Advanced Diagnostics for Spray Behavior, Fuel Impingement, and Soot Processes in Direct Injection Spark Ignition Engines

by

Luis G. Gutierrez Arsuaga

A dissertation submitted in partial fulfillment
of the requirements for the degree of
Doctor of Philosophy
(Mechanical Engineering)
in the University of Michigan
2019

Doctoral Committee:

Professor Margaret S. Wooldridge, Chair
Professor Andre Boehman
Professor Matthew Johnson-Roberson
Professor Branko Kerkez

Luis G. Gutierrez

lgga@umich.edu

ORCID iD: 0000-0002-5295-3036

Dedication

A mis abuelos y mis padres,

no soy más que el fruto de sus sacrificios

Acknowledgments

I would like to start by expressing my profound gratitude to Professor Margaret Wooldridge. The opportunity she gave me by inviting me to be part of her research group has formed and inspired who I am today at a professional, intellectual, and personal level. The work presented here would not have been possible without her constant guidance, insightful feedback, and the freedom she gave me to explore new ideas and fields even when the path was not clear nor the success certain. I will be forever grateful to her for everything I learned and got to experience thorough my doctoral journey.

I would also like to thank Professor Andre Boehman, Professor Branko Kerkez, and Professor Matthew Johnson-Roberson for serving in my dissertation committee and for their invaluable input, comments, and feedback. The insights and advice they provided facilitated and shaped the work presented in this dissertation.

I am extremely thankful for the generous financial funding and technical support from Ford Motor Company. I would like to especially thank Dr. Benjamin Petersen and Dr. Steven Wooldridge for their guidance and collaboration during the multiple phases of my degree.

I would like to thank the University of Michigan, the Department of Mechanical Engineering, and their staff and faculty. I have been extremely fortunate to be part of this amazing institution that challenged me every day to become a better version of myself. Special thanks to the ME-IT staff: Jon Klozik, Matthew New, and Nick Cantu for all their help fixing, recovering, and setting-up the multiple computer systems used in this work.

To my friends in Ann Arbor and back in Mexico, thank you for your encouragement and friendship through the years. To my present and past lab mates: Andrew, Cesar, Dimitris, Mario, Max, Miles, Mohammad, Rachel, Ripudaman, and Scott, for the daily doses of joy, insightful conversations, and intellectual challenges.

And last but not least, I want to thank all my family. My parents for supporting me and inspiring me at every stage of my life, and for being the embodiment of sacrifice and love. To my grandparents, who are greatly missed, for their wisdom and pure love. To my siblings, Magda, Rodolfo, and Mariela, for continuously motivating me and for always being close when I need them the most. To Fernando, Gi, and Sandra, for receiving me into their family as a son and a brother, and for all their caring. And finally, to my wife, Patricia, for her unmeasurable love, kindness, and faith in me. Thank you for filling my world with light and bliss and for being my companion through this journey and my partner in every part of my life. You are my PhD.

Table of Contents

List of Tables

List of Figures

List of Appendices

Abstract

Direct injection spark-ignition (DISI) engines have significant potential to improve vehicle fuel economy and CO_2 emissions in the transportation sector. Recent years have seen rapid growth in the market penetration of DISI engines in light-duty vehicles as a result of the intrinsic benefits the technology offers. Nonetheless, DISI engines face important challenges regarding regulated emissions, especially in terms of particulate matter (PM). Soot particles represent significant health and environmental hazards; thus, current emission standards strictly limit PM emissions and future regulations will be even more stringent. The objective of this work was to provide novel insights, analysis, and diagnostic tools to study and mitigate some of the drawbacks of direct injection systems, without compromising the superior thermal efficiency of DISI engines. The studies focused on the behavior of fuel sprays, soot formation at cold start conditions, and spray impingement. The experimental approach leveraged high-speed imaging of fuel injection, combustion, and spray impingement in optically-accessible engines to better understand various in-cylinder phenomena. First, non-reactive spray imaging experiments were conducted at three engine speeds (300, 1000, and 2000 RPM) and two intake pressures (50 kPa and 98 kPa) to assess the effects of piston motion and fuel flash boiling on the behavior and time evolution of fuel sprays. The results showed the significant influence of the in-cylinder flow and plume collapse on spray development, liquid fuel distribution, and cycle-to-cycle variability. Second, different charge strategies at cold start conditions (20° C) were evaluated by imaging the injection and combustion processes, while measuring engine-out gaseous and soot emissions. The different fueling strategies considered up to two injection events spanning a range of injection timing form 300° to

25° before top death center (bTDC). Differences in combustion, soot sources, and PM characteristics particular to the cold-start environment were identified, specifically fuel-rich pockets and wetted surfaces. Results show that emissions and engine performance are dominated by the effects of the later injection. Finally, a novel diagnostic tool for fuel impingement was designed and demonstrated. A piston was instrumented with a prototype sensor and a telemetry technique was developed for non-contact data transmission. The system was tested in a static optical engine while high-speed imaging of the spray was simultaneously recorded. The sensor was used to measure films formed by different blends of ethanol and gasoline (E10 to E80) at varying injection pressures and injection durations. The response of the prototype sensor was fast enough to capture the sub-microsecond dynamics in the spray impingement event (<0.5 ms). The results demonstrated the sensor has excellent resolution and sensitivity to detect spatial and temporal characteristics of the impingement and the films generated by a realistic fuel injection system. Overall, the outcomes of the present work provide better understanding of the relationships between fuel spray characteristics and engine performance, which directly inform and improve fueling strategies for this important class of internal combustion engines.

Chapter 1

Introduction

1.1 Background

Meeting growing energy demands while mitigating the environmental impact of human activity remains one of the biggest challenges of our time. High-efficiency energy systems have become urgently needed as major concerns over the associated climate effects of energy production and high population growth rates increase. Researchers have addressed these concerns by redesigning energy systems to readily supply complex energy needs in a sustainable manner. While the results of these efforts are significant, additional work is remaining since energy demand is expected to increase drastically in the near future. The global primary energy consumption was approximately 600 quadrillion BTU (where 1 quad = 10^{15} BTU) in 2018. It is expected that by 2040 the total energy demand will increase to 739 quad BTU –almost a 25% increase [1].

Even though the energy carriers in the global portfolio have expanded in recent years, combustion is still an essential component of energy production as it represents more than 82% of the global energy supply; power generation forecasts project this proportion to continue in the next decades [1], [2]. Moreover, combustion of liquid fuels, like gasoline and diesel, dominates the transportation sector since this application requires a high-energy density and high-power energy carrier. In 2018, combustion of petroleum-derived fuels and biomass represented 96% of the total energy consumed to transport goods and people in the U.S. [3]. This high figure contrasts with the overall low efficiency that characterizes the transportation sector, where only 21% of the energy is translated into useful work [4]. Increasing the efficiency of the transportation sector is paramount since combustion systems with low thermal efficiency equate to higher emissions of the greenhouse gases responsible for climate change. This latter fact has been identified as both a motivation and an area of opportunity for novel technology developments [5].

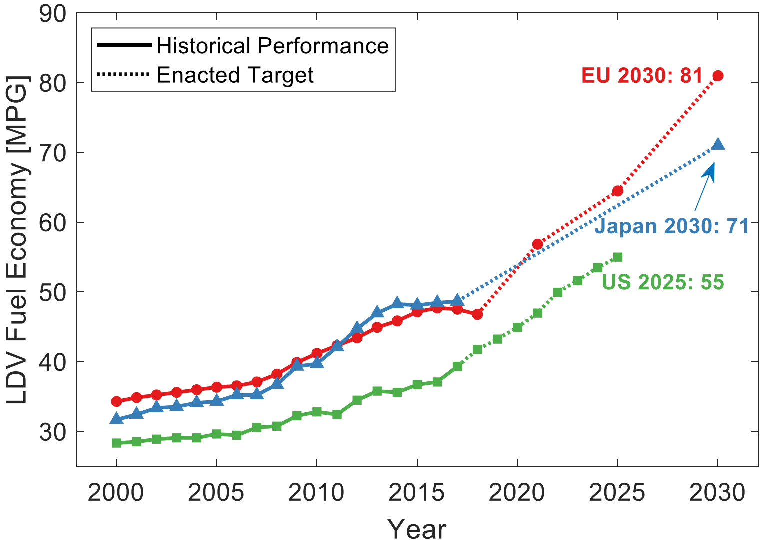

Figure 1.1. Historical trends and enacted targets for LD vehicle fuel economy of three geographical regions. Adapted from [6].

In particular, improving the efficiency of light-duty (LD) vehicles has become a primary objective of industry, researchers, government programs and policy [7]–[9]. Passenger transportation accounts for the largest share of energy consumption in transportation sector, and in turn, LD vehicles consume close to 70% of the energy used for passenger transportation [2]. LD vehicles are predominantly fueled using hydrocarbon fuels; 99.1% the energy used by LD vehicles in 2018 came from gasoline in the U.S [10]. Therefore, addressing the need to increase the fuel economy of passenger vehicles is key in achieving more efficient and sustainable global energy systems. At least nine countries (or geopolitical regions) have enacted policies to improve the efficiency of vehicles. Figure 1.1 presents the historical trends for LD vehicle fuel economy for three regions –the European Union, Japan, and the U.S.– and the enacted targets in these nations. Although substantial progress has been achieved in the past few decades, the figure shows that significant work is needed to reach the established goals.

1.2 Direct Injection Spark Ignited Engines

The direct injection spark ignition (DISI) engine is one of the technologies with significant potential to improve vehicle fuel economy and lower carbon emissions of LD vehicles [11]. This engine technology is also commercially known as gasoline direct injection (GDI) and spark-ignited direct injection (SIDI) engines. Recent years have seen rapid growth in market penetration of direct injection (DI) engines due to demonstrated fuel economy improvements. By 2016, DISI engines had captured 49% of the LD market in the 9 years since their commercial introduction, as shown in Figure 1.2 [5].

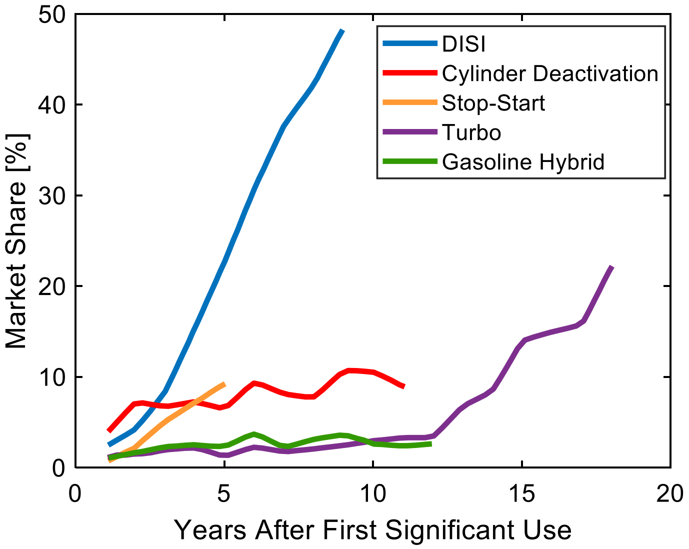

Figure 1.2. Market share of engine technologies aimed at improving vehicle and engine fuel consumption. Figure adapted from [5].

The other technologies shown in the figure also aim at improving the fuel efficiency of LD spark-ignition vehicles and, importantly, all benefit from operating with a direct fuel injection system. Hence, DISI is considered a crucial piece in developing passenger vehicles with better efficiency and less environmental impact [5], [12], [13].

Generally, two characteristics of directly injecting fuel into the cylinder are exploited to produce engines with higher specific power, higher efficiency, and, consequently, less CO_2 emissions: 1) an evaporative cooling effect on the mixture, and 2) more precise control of the fuel and air charge preparation. Firstly, as fuel is injected into the cylinder, it rapidly evaporates, decreasing the temperature of the charge, and increasing the density [14], [15]. This phenomenon can be used to increase the volumetric efficiency while additionally decreasing the probability of knocking –a violent and uncontrolled auto-ignition of the charge, which can damage the engine [14]. The propensity of the mixture to auto-ignite increases exponentially with an increase in the mixture temperature. As a result, knock mitigation strategies in spark-ignition engines typically limit the engine compression ratio and hence the end of compression temperatures, which limits the thermal efficiency of spark-ignition engines. However, the cooling effect that direct injection has on the mixture, allows higher compression ratios and more aggressive boosting (e.g., turbo- and supercharging), which translates to a lighter and more efficient engine, without sacrificing power output. This strategy –that is, engines with smaller displacement volumes coupled with forced induction– is known as engine downsizing, and the approach has recently become the focus of significant commercial and research efforts [7], [11], [12], [14], [16].

The second benefit from having the injector located inside the combustion chamber is that it enables the exact metering of fuel mass and injection timing during the cycle; leading to more precise control of the mixture composition and fuel distribution. Advanced combustion strategies that offer efficiency improvements can be implemented using the improved control of charge mixing and composition [13], [15], [17], [18]. Additionally, the superior control of fuel metering and timing improves the response of the engine during transient operation [19]. Technologies that intrinsically increase the transient aspects of engine operation (e.g., stop-start, cylinder deactivation, and hybrid powertrains) especially require or benefit from better control of the mixture characteristics. The synergy of coupling advanced strategies with direct injection improves engine performance and enables higher-efficiency systems.

1.3 Particulate Matter in Direct Injection Engines

Direct injection engines face important challenges regarding emissions, predominantly particulate matter (PM) or soot. DISI engines produce higher PM emissions, compared with LD engines that use port fuel injection (PFI) [20]–[22]. Soot particles represent a significant health and environmental hazard [23], [24]. As a result, current emission standards strictly limit end-tailpipe particulate emissions, and future regulations will be more stringent [9]. At the federal level, vehicle PM emission standards are set by the Environmental Protection Agency (EPA) in the U.S. The EPA Tier 3 emissions regulation for particulate mass from light-duty vehicles are 3 mg/mi, and started phasing in for the model year 2017; the standard will be applied to all LD vehicles by 2022 [9]. The State of California recently adopted regulations that are even more stringent than the national standards. The Low Emission Vehicle (LEV) III sets the limit at 1 mg/mi, and starts phasing-in by 2025, with full implementation by 2028 [25]. In Europe, the emission standard regulates particulate number (PN) instead of particulate mass. The Euro 6c limits the PN at 6×10^{11}/km for vehicles with direct injection, and will be in complete compliance by 2020 [22].

At the fundamental level, soot formation is governed by numerous thermophysical and chemical factors that interact in a complex manner [26]. In the context of DISI engines, spray behavior, fuel impingement, and engine temperature play major roles in the formation and emission of soot particles [27]–[30]. The fuel spray, coupled with the effects of in-cylinder charge motion, is responsible for the charge preparation and mixing characteristics, and therefore, spray behavior has a direct and significant impact on engine emissions [31]. A second phenomenon relevant to the injection is fuel impingement on the combustion chamber surfaces. If the fuel spray impinges on the cylinder and piston surfaces, it forms a fuel film that leads to pool fires and incomplete combustion, thus, augmenting soot emissions [11], [15].

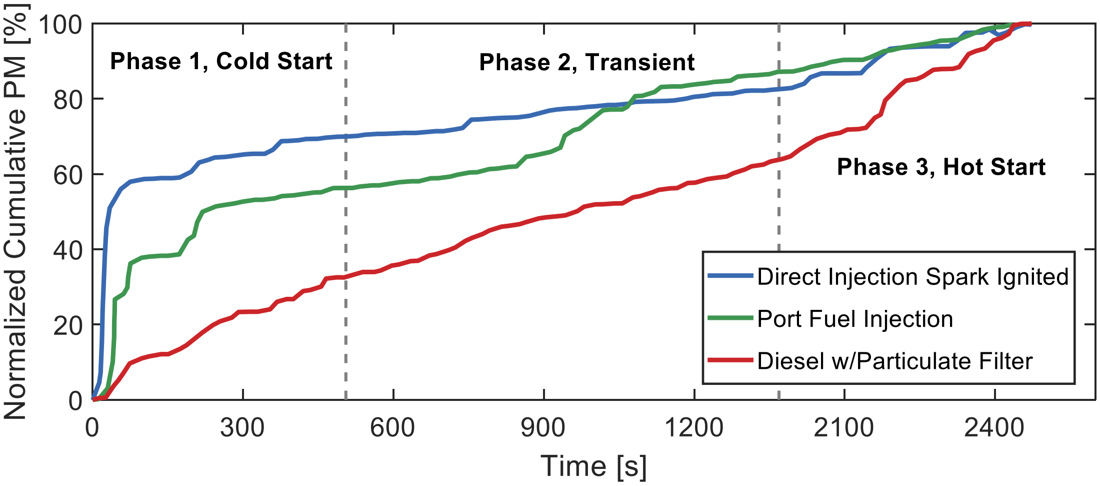

Figure 1.3. Particulate emissions from different engine technology during the Federal Test Procedure (FTP) 75. Adapted from [32]

Finally, low operating temperatures associated with cold-start conditions introduce numerous problems to the performance of the system. For example, the efficiency of the engine decreases due to higher friction losses caused by the higher oil viscosity [33]. Additionally, the intake air temperature is lower than at fully warm-up conditions, so the fuel does not vaporize properly and spray penetration increases during fuel injection, increasing the likelihood of fuel impingement [15]. Engine-out emissions are typically higher during the initial cold-start phase for all internal combustion engines; however, DISI PM emissions are especially sensitive to this condition, as shown in Figure 1.3 [11], [32], [34], [35]. The coupled effects of direct injection and cold-start conditions combine to exacerbate the propensity of DISI to form soot and other harmful emissions. It is therefore critical to devise methods to mitigate in-cylinder soot formation to ensure that the DISI engine technology can comply with emission control policies, without compromising the efficiency benefits from this technology.

1.4 Research Objectives and Chapter Content

The overall objective of this dissertation is to provide new insights, methods, and diagnostic tools to enable soot emissions reduction in direct injection spark ignition engines without sacrificing thermal efficiency or engine performance. The studies focus on the behavior of fuel sprays, cold-start operation, and fuel impingement using a combination of imaging, sensor development, and DISI engine experiments using gasoline, gasoline-ethanol blends, and the gasoline surrogate iso-octane. First, the effects of charge motion and fuel flash boiling on non-reactive sprays were investigated in an optically accessible DISI engine. The spray cycle-to-cycle variability was also explored. Second, the sources of soot at cold-start conditions were identified and the effects of charge preparation strategy –i.e., stratified or homogeneous charge– on PM formation during this phase were investigated. The final component of the work focused on developing a new in-situ diagnostic to study spray impingement. While the approach focuses on iso-octane, gasoline, and ethanol-gasoline fuel blends, the methods are generally applicable to diesel direct injection compression ignition engines as well.

The technical approach was based on multiple techniques to interrogate the fuel spray and the related combustion and emission behaviors in DISI engines. Reactive and non-reactive experiments were conducted using two optically accessible engines. Several aspects of spray development and impingement, combustion, and emissions were explored using different high-speed imaging methods, conventional in-cylinder sensors, and exhaust analyzers. Spray variability was evaluated using two variations of proper orthogonal decomposition (POD). Finally, a novel film sensor was tested in an optical engine and coupled with Mie scattering imaging of the fuel injection and spray-wall interactions.

Chapter 2 presents the results of the investigation of the time-evolution of non-reactive sprays in an optically accessible engine. A canonical gasoline fuel injector that has been extensively studied in constant-volume chambers (CVC) at conditions typical of reciprocating engines [36], [37] was used in this part of the dissertation study. Previous work on non-reactive sprays in CVC and optical engines are discussed in the chapter. The work in this dissertation expanded on the previous efforts to characterize the injector and fuel sprays by imaging for the first time the spray development inside a motoring engine. The liquid-phase structure of the spray plumes was imaged using Mie-scattering with a high-speed camera. Two ambient pressures and three engine speeds were used to evaluate the effects of flash boiling and charge motion on the spray structure and time evolution.

Understanding the sources of cycle-to-cycle variability (CCV) in an engine is critical, as reducing variability can improve operation and emissions of vehicles. A brief review of methods to quantify and study CCV in engines is presented in Chapter 3. The work Chapter 3 focuses in using the imaging data from Chapter 2 to assess the effects of engine speed and flash boiling on the cycle-to-cycle variability of the spray structure. Two variants of proper orthogonal decomposition (POD) –the snapshot method and the space-time POD– were applied to the time-resolved imaging data and results are presented in Chapter 3. A brief review of the fundamentals of the POD method and its application to engine data is included in this chapter. The study is the first application of the space-time POD to cycle-resolved spray imaging data.

As mentioned before, the emissions of DISI engines are higher during the cold-start phase compared with warmed-up operation. One very effective way to mitigate engine-out emissions is by controlling the mixing characteristics of the charge. The effects of different charge strategies at cold-start conditions on engine performance and particulate matter (PM) emissions in an optically-accessible engine are presented in Chapter 4. This chapter includes a brief review of the literature on soot formation in combustion systems and previous research exploring how operating parameters impact PM emissions in internal combustion engines. A discussion of the challenges faced by direct injection systems during the cold-start phase is also presented. The study leverages high-speed imaging of fuel sprays, combustion, and natural incandesce, coupled with a gas analyzer and soot measurement tools, to better understand sources of PM formation. The results offer new insights on fuel and soot phenomena that are particular to the cold-start phase that have an important impact on the emissions formed.

Fuel impingement poses a challenge to direct injection engines, as is still a poorly understood phenomenon that increases engine-out emissions. Robust and versatile diagnostics of fuel impingement characteristics are still lacking. Previous experimental techniques to study films generated by spray impingement and conceptual models of spray-wall interaction are presented in Chapter 5. The present work focused on the design, development, and demonstration of a novel sensor to detect fuel films produced by spray impingement. The goal of this part of the dissertation was to generate a fast, sensitive, and in-situ tool to improve experimental understanding of fuel impingement in engines. The diagnostic device is based on a capacitive sensing technique using an interdigitated electrode structure. A piston was instrumented with the sensor and a telemetry technique was developed for non-contact data transmission. The instrument was tested on a static engine while simultaneously imaging the spray. Results show the sensor capabilities and demonstrate the potential to study fuel films with this new tool. The sensor developed in this work represents the first use of capacitive sensing to study fuel impingement in engines. The final chapter of the thesis presents the conclusions of the studies and thoughts on future work.

1.5 Abbreviations

CCV	Cycle-to-cycle variability
CVC	Constant volume chamber
CO	Carbon monoxide
DI	Direct injection
DISI	Direct injection spark ignition

EPA	Environmental Protection Agency
FTP	Federal test procedure
GDI	Gasoline direct injection
HC	Hydrocarbon
IDE	Interdigitated Electrodes
LD	Light-duty
LEV	Low-Emissions Vehicle
NOx	Nitrogen oxides
PM	Particulate matter
PN	Particle number
POD	Proper Orthogonal Decomposition
RPM	Revolutions per minute
SIDI	Spark-ignited direct injection
SMPS	Scanning mobility particle sizer
SOI	Start of injection
TWC	Three-way catalyst
UHC	Unburned hydrocarbons

References

[1] L. Capuano, "International Energy Outlook 2018," Washington, DC, 2018.

[2] U.S. Energy Information Administration, "International Energy Outlook 2016," 2016.

[3] L. L. N. Laboratory, "Estimated U.S. Energy Consumption in 2018," 2019. [Online]. Available: https://flowcharts.llnl.gov/commodities/energy.

[4] U.S. Energy Information Administration, "Monthly Energy Review, June 2019," 2019.

[5] S. C. Davis, S. E. Williams, R. G. Boundy, and S. A. Moore, "2016 Vehicle Technologies Market Report," Oak Ridge, TN (United States), Mar. 2014.

[6] International Council on CleanTransportation, "Chart library: Passenger Vehicle Fuel economy," 2019. [Online]. Available: https://theicct.org/chart-library-passenger-vehicle-fuel-economy.

[7] G. A. Lavoie, E. Ortiz-Soto, A. Babajimopoulos, J. B. Martz, and D. N. Assanis, "Thermodynamic sweet spot for high-efficiency, dilute, boosted gasoline engines," *Int. J. Engine Res.*, vol. 14, no. 3, pp. 260–278, Jun. 2013.

[8] V. T. Office, "Advanced Combustion Systems and Fuels," 2017.

[9] Z. Yang and A. Bandivadekar, "2017 Global update: Light-duty vehicle greenhouse gas and fuel economy standards," 2017.

[10] U.S. Energy Information Administration, "Annual Energy Outlook 2019 - Light-Duty Vehicle Energy Consumption by Technology Type and Fuel Type," 2019.

[11] J. Koczak, A. Boehman, and M. Brusstar, "Particulate Emissions in GDI Vehicle Transients: An Examination of FTP, HWFET, and US06 Measurements," *SAE Tech. Pap.*, vol. 500, 2016.

[12] V. Triantopoulos, "Experimental and Computational Investigation of Spark Assisted Compression Ignition Combustion under Boosted, Ultra-EGR Dilute Conditions," University of Michigan, Ann Arbor, 2018.

[13] A. C. Alkidas, "Combustion advancements in gasoline engines," *Energy Convers. Manag.*, vol. 48, no. 11, pp. 2751–2761, 2007.

[14] Z. Xu, J. Yi, S. Wooldridge, D. Reiche, E. W. Curtis, and G. Papaioannou, "Modeling the Cold Start of the Ford 3.5L V6 EcoBoost Engine," *SAE Int. J. Engines*, vol. 2, no. 1, pp. 2009-01–1493, 2009.

[15] M. Fatouraie, M. Wooldridge, and S. Wooldridge, "In-Cylinder Particulate Matter and Spray Imaging of Ethanol/Gasoline Blends in a Direct Injection Spark Ignition Engine," *SAE Int. J. Fuels Lubr.*, vol. 6, no. 1, pp. 2013-01–0259, Apr. 2013.

[16] R. Singh, "Enabling Ethanol Use as a Renewable Transportation Fuel : A Micro- and Macro-scale Perspective," University of Michigan, Ann Arbor, 2019.

[17] P. S. Shingne, M. S. Gerow, V. Triantopoulos, S. V Bohac, and J. B. Martz, "A Comparison of Valving Strategies Appropriate For Multimode Combustion Within a Downsized Boosted Automotive Engine—Part I: High Load Operation Within the Spark Ignition Combustion Regime," *J. Eng. Gas Turbines Power*, vol. 136, no. 10, p. 101507, May 2014.

[18] M. S. Gerow, P. S. Shingne, V. Triantopoulos, S. V. Bohac, and J. B. Martz, "A Comparison of Valving Strategies Appropriate for Multimode Combustion Within a Downsized Boosted Automotive Engine—Part II: Mid Load Operation Within the SACI Combustion Regime," *J. Eng. Gas Turbines Power*, vol. 136, no. 10, p. 101508, May 2014.

[19] M. Fatouraie, "The Effects of Ethanol / Gasoline Blends on Advanced Combustion Strategies in Internal Combustion Engines," pp. 1–147, 2014.

[20] J. Su, W. Lin, J. Sterniak, M. Xu, and S. V. Bohac, "Particulate Matter Emission Comparison of Spark Ignition Direct Injection (SIDI) and Port Fuel Injection (PFI) Operation of a Boosted Gasoline Engine," *J. Eng. Gas Turbines Power*, vol. 136, no. 9, p. 091513, May 2014.

[21] P. Price, R. Stone, T. Collier, and M. Davies, "Particulate Matter and Hydrocarbon Emissions Measurements: Comparing First and Second Generation DISI with PFI in Single Cylinder Optical Engines," in *SAE Technical Paper Series*, 2006, vol. 1, no. 724.

[22] M. Braisher, R. Stone, and P. Price, "Particle Number Emissions from a Range of European Vehicles," 2010.

[23] R. D. Brook *et al.*, "Air Pollution and Cardiovascular Disease," *Circulation*, vol. 109, no. 21, pp. 2655–2671, Jun. 2004.

[24] J. Stolcpartova *et al.*, “Internal Combustion Engines as the Main Source of Ultrafine Particles in Residential Neighborhoods: Field Measurements in the Czech Republic,” *Atmosphere (Basel).*, vol. 6, no. 11, pp. 1714–1735, Nov. 2015.

[25] K. G. Duleep, “The Impact of Gasoline Direct Injection System Design on PM Emissions,” 2019, pp. 1–16.

[26] A. Violi, A. F. Sarofim, and T. N. Truong, “Mechanistic Pathways to Explain H/C Ratio of Soot Precursors,” *Combust. Sci. Technol.*, vol. 174, no. 11–12, pp. 205–222, Nov. 2002.

[27] M. Fatouraie, “The Effects of Ethanol/Gasoline Blends on Advanced Combustion Strategies in Internal Combustion Engines,” pp. 1–147, 2014.

[28] H. Chen, D. L. Reuss, and V. Sick, “Analysis of misfires in a direct injection engine using proper orthogonal decomposition,” *Exp. Fluids*, vol. 51, no. 4, pp. 1139–1151, Oct. 2011.

[29] F. Schulz, J. Schmidt, A. Kufferath, and W. Samenfink, “Gasoline Wall Films and Spray/Wall Interaction Analyzed by Infrared Thermography,” *SAE Int. J. Engines*, vol. 7, no. 3, pp. 2014-01–1446, Apr. 2014.

[30] P. Price, R. Stone, T. Collier, and M. Davies, “Particulate Matter and Hydrocarbon Emissions Measurements: Comparing First and Second Generation DISI with PFI in Single Cylinder Optical Engines,” in *SAE Technical Paper Series*, 2006, vol. 1, no. 724.

[31] S. N. Soid and Z. a. Zainal, “Spray and combustion characterization for internal combustion engines using optical measuring techniques – A review,” *Energy*, vol. 36, no. 2, pp. 724–741, Feb. 2011.

[32] D. C. Quiros *et al.*, “Measuring Particulate Emissions of Light Duty Passenger Vehicles Using Integrated Particle Size Distribution (IPSD),” *Environ. Sci. Technol.*, vol. 49, no. 9, pp. 5618–5627, May 2015.

[33] A. Roberts, R. Brooks, and P. Shipway, “Internal combustion engine cold-start efficiency: A review of the problem, causes and potential solutions,” *Energy Convers. Manag.*, vol. 82, pp. 327–350, 2014.

[34] G. K. Hargrave, P. Efthymiou, J. E. T. Rimmer, M. H. Davy, D. Richardson, and C. P. Garner, “Insights into Cold-Start DISI Combustion in an Optical Engine Operating at −7°C,” *SAE Int. J. Engines*, vol. 6, no. 2, pp. 1059–1074, 2013.

[35] P. Efthymiou, C. P. Garner, G. K. Hargrave, and D. Richardson, “An Optical Analysis of a DISI Engine Cold Start-Up Strategy,” in *SAE Technical Paper Series*, 2015, vol. 1.

[36] J. Lacey *et al.*, “Generalizing the behavior of flash-boiling, plume interaction and spray collapse for multi-hole, direct injection,” *Fuel*, vol. 200, pp. 345–356, 2017.

[37] L. Allocca, A. Montanaro, and G. Meccariello, “Effects of the Ambient Conditions on the Spray Structure and Evaporation of the ECN Spray G,” 2019, pp. 1–11.

Chapter 2

Effects of Engine Speed and Flash Boiling on Non-reactive Sprays in an Optical Engine

This chapter was published as part of the SAE World Congress: Gutierrez, L., Mansfield, A., Fatouraie, M., Assanis, D. et al., "Effects of Engine Speed on Spray Behaviors of the Engine Combustion Network "Spray G" Gasoline Injector," SAE Technical Paper 2018-01-0305, 2018, https://doi.org/10.4271/2018-01-0305.

2.1 Introduction

Fuel spray processes are inherently important to direct injection and other advanced technology internal combustion engine operation in terms of performance and emissions. It is therefore critical both to the improvement of existing designs and the development of future advanced combustion strategies that real fuel spray processes in engine-like conditions, be well investigated, understood and modeled. To this end, an international collaboration called the Engine Combustion Network (ECN) was formed between numerous academic, federal laboratory and industrial partners, aimed at improving engine-relevant spray experiments and models. As part of this collaboration a prototype injector manufactured by Delphi, the "Spray G" injector, is presently under investigation by many groups simultaneously [1].

While the Spray G injector behaviors have been characterized in various experimental facilities to date, specifically in constant volume quiescent spray chambers [2]–[6], there has been no published evaluation in an actual reciprocating engine. Indeed, injector characterizations in quiescent spray chambers are useful for basic spray model validation; however, it is vitally important to evaluate and model injector behaviors during more realistic engine operation when, at a minimum, intake air charge motion and turbulence are expected to have significant impact. Furthermore, it is key to understand the connections and differences between spray behavior in constant volume spray chambers, commonly used in many research and development settings, and spray behavior in real engines.

Previous investigations by Aleiferis et al. [7], Allocca et al. [8], and Bao et al. [9] considered some comparisons of spray behaviors of gasoline and biofuel between a spray chamber apparatus and a motoring single-cylinder engine. The studies illustrated significant differences in spray behaviors between the two types of facilities, however, the engine data in each study were limited to a single speed. Considering the direct relationship between engine speed and flow-field properties (e.g., turbulence, charge motion, etc.), variations in engine speed expected in real operation would affect fuel spray behaviors, and how the changes relate to behaviors in a typical quiescent spray chamber are of considerable interest.

To address these needs, the primary objective of the present brief work was to characterize, compare, and document the behaviors of the Spray G gasoline fuel injector in both a constant volume spray chamber and a single-cylinder engine over a range of engine speeds for two standard thermodynamic conditions set by the ECN. The data are crucial to improve understanding of spray development and modeling at realistic engine conditions as part of the Engine Combustion Network.

2.2 Experimental Set-up

The present work includes experimental investigations of the Spray G injector in two optically accessible facilities, a single-cylinder engine at the University of Michigan (UofM) and a constant volume spray chamber at the University of Melbourne (UMelbourne). In both facilities, iso-octane fuel spray from the Spray G injector was observed optically using high-speed, diffusebacklit, Mie-scatter imaging, from which the spray behaviors were quantitatively analyzed. The Mie scattering technique used in this study assumes that the scattered light and detected by the camera correlates with the presence of liquid fuel at that location [10].

Table 2.1. Spray G2 and G3 conditions as defined by the ECN

Variable	Spray G2	Spray G3
Ambient Pressure	50 kPa	100 kPa
Fuel	Iso-octane	
Fuel Pressure	20 MPa	
Fuel Temperature	90° C	
Ambient Temperature	60°	
Fuel Mass	10 mg	
Electronic Pulse	0.680 ms	

Two initial thermodynamic conditions, pre-defined by the ECN, were used in both facilities: a) G2 at 50 kPa ambient pressure, and b) G3 at 100 kPa ambient pressure. Here, ambient means the air into which the fuel was sprayed. Spray G2 represents an early injection at throttled conditions, while G3 is representative of a fully open throttle early injection. Fuel rail temperature and pressure were fixed at 60°C and 20 MPa, respectively. The ambient temperature was 60°C. Iso-octane fuel (2,2,4-trimethyl pentane, Sigma Aldrich, anhydrous, 99.8% purity) was used. It should be noted, that Spray G2 conditions induce flash-boiling in iso-octane, while at G3 conditions, flash boiling is not observed. The injected fuel mass was constant at 10 mg, with an electronic pulse width of 0.68 milliseconds. For the single-cylinder engine experiments, the intake manifold air temperature and pressure were controlled to the desired ambient conditions. A summary of these standard experimental conditions are shown in Table 2.1.

The Spray G Injector was manufactured by Delphi as a gasoline fuel injector with 8-holes evenly spaced in a circular pattern, orifice drilling angle of 37° relative to the nozzle axis, 0° bend angle, orifice length/diameter ratio of 1.4, nominal orifice diameter of 0.165 mm, and a flowrate of 15 cm^3/s at 10 MPa fuel line pressure. A summary of the specifications for the Spray G injector are presented in Table 2.2.

Table 2.2. ECN Spray G injector specifications

Variable	Values
Injector Type	Solenoid-activated
Number of Holes	8
Orifice Diameter	165 micrometers
Orifice Drill Angle	37° relative to nozzle axis
Full Outer Angle	80°
Flow Rate	15 cm^3/s at 10 MPa

2.2.1 University of Michigan Single-cylinder Engine

The University of Michigan single-cylinder engine used in the study was an optically accessible engine, reconfigurable with optical and metal bore liners and optical piston insert. A Bowditch-style crank was used with a modified dual-camshaft four-valve Ford Zetec Sigma-SE 1.25 L cylinder head. The engine had a 71.9 mm bore, 76.5 mm stroke, compression ratio of 10.0:1, and a total displacement 0.31 L. The production head, originally designed for port-fuel injection, was modified to accept a central fuel injector located 6.5 ± 0.5 degrees out of parallel with the bore. In-cylinder pressure was measured using a Kistler 6125A transducer mounted between the intake and exhaust valves at the periphery of the combustion chamber. A detailed description of the engine, before the modification to direct injection, is given by Zigler et al. [11]. A substantial intake manifold plenum volume (~20 L) was used to reduce intake manifold pressure dynamics and to ensure the heated intake air temperature was well mixed. The intake air temperature was controlled using resistive heaters. Engine coolant temperature was controlled via a PID controller and an external water pump. An in-line external resistive heater and an external cold-water heat-exchanger was used to ensure the coolant temperature was maintained at the desired set-point temperature. A diagram for the single-cylinder and the experimental equipment used is presented in Figure 2.1.

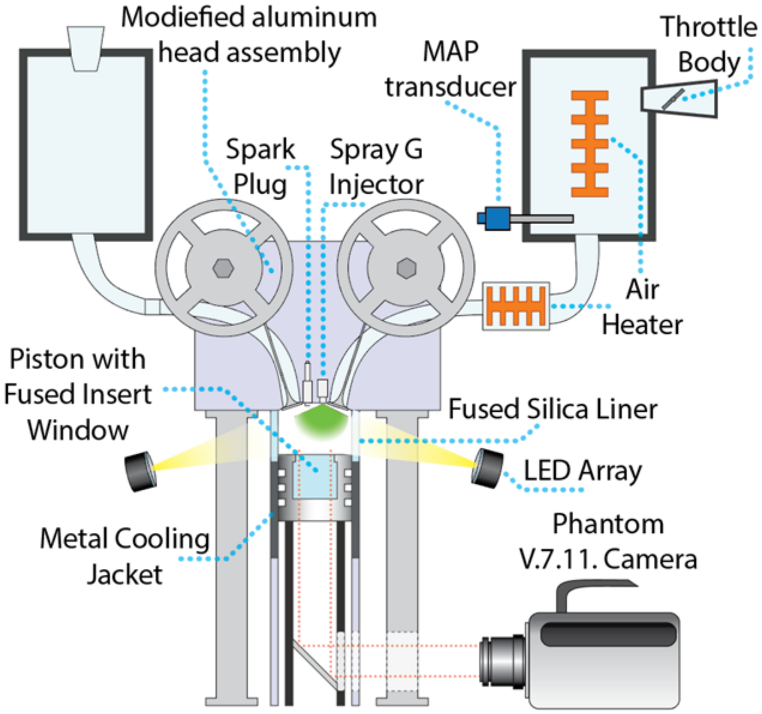

Figure 2.1. Schematic for single-cylinder optical engine and equipment used at UofM.

In the present work, optical observations of the in-cylinder spray process were made through a transparent piston crown (48.5 mm diameter window) and 45° elliptical mirror located inside the piston extension tube, below the piston. High-speed color imaging was recorded using a digital video camera (V711-8G-MAG-C, Vision Research, Phantom) with an AF Nikkor 80-200mm lens (f/5.6). Video sequences were recorded at 24,000 frames/s with a CMOS array resolution of 512×512 pixels, resulting in an exposure time of 41.3 µs and a spatial resolution of 101 µm/pixel. During all imaging experiments, the camera was focused on the injector tip. A partial optical bore liner, with 25 mm in height, was used, through which two light emitting diode arrays (Visual Instrumentation Corporation Model 900420) provided diffuse backlighting of the spray. A view of the combustion chamber through the optical imaging system is shown in Figure 2.2.

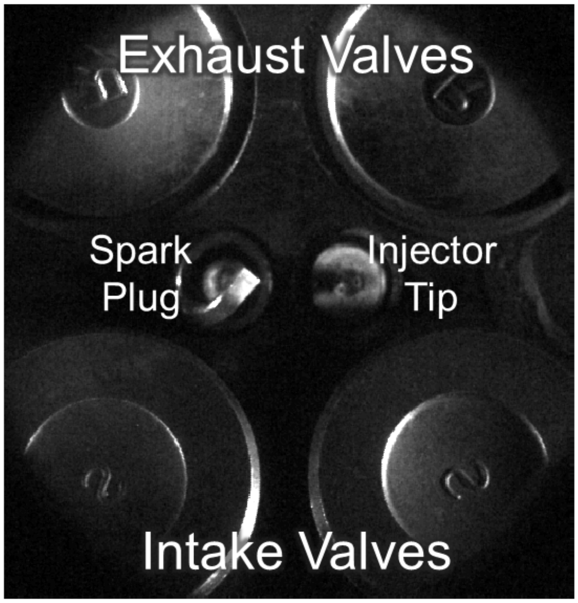

Figure 2.2. UofM single-cylinder engine combustion chamber view through the optical insert in the piston crown.

Spray observations were made during engine motoring at 300, 1,000, and 2,000 RPM and fuel was injected once every 10 cycles in order to maintain uniform in-cylinder conditions. Fuel was injected in a single pulse with start of injection (SOI) at 270 crank angle degrees before top-dead-center (CAD bTDC), which coincided with the maximum intake valve opening lift. Spray end-of-injection (EOI) occurred after approximately 1 ms and therefore all results here are reported for a duration of 800 μs or less. The high-speed camera was simultaneously triggered by the fuel injection signal, automatically generating a recording from just before the fuel injection event to well after the spray plume had exceeded the viewable area. The videos were then post-processed individually to analyze spray behaviors, as described in detail in Section 2.3.1. For each combination of conditions (G2 or G3) and engine speed, approximately 30 videos were recorded.

2.2.2 University of Melbourne Constant Volume Chamber

The Spray G injector has been characterized in quiescent environments both in computational and experimental studies [3], [5], [6], [12]. For this particular study, the constant volume chamber (CVC) experiments were performed at the University of Melbourne. The facility consists of a quiescent chamber with three cylindrical windows, each 90 mm in diameter. Nitrogen was used to pressurize the interior of the CVC; the fuel temperature was regulated using a heating element surrounding the fuel line. Two tungsten spotlights (Dedolight Dedocool Standard 2-Light Kit) were used to illuminate the spray from the sides, as seen in Figure 2.3.

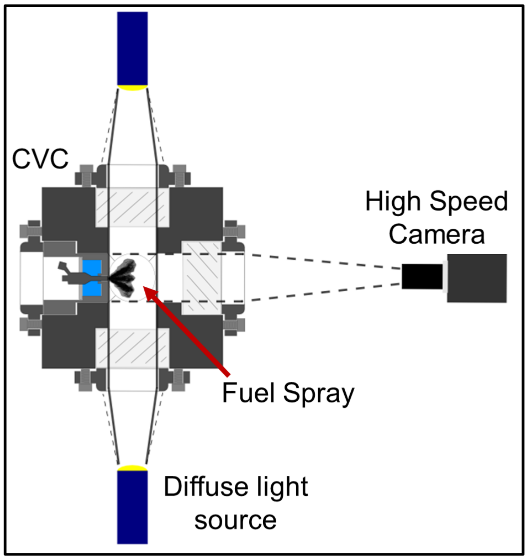

Figure 2.3. Schematic of the UMelbourne facility constant volume chamber.

The spray was imaged orthogonal to the direction of the spray using a high-speed CMOS camera (Phantom Miro 310, Vision Research) with a Nikon 135 mm Nikon Zoom Lens (f/8). Videos were recorded at 20,000 frames/s, with a resolution of 384×344 pixels, exposure time of 10 μs, and spatial resolution of 232 μm/pixel.

2.3 Experimental Approach

2.3.1 Spray Imaging and Analysis

Using the high-speed imaging videos from both facilities and a custom post-processing algorithm it was possible to quantify certain features of the spray for comparison and benchmarking purposes. Unlike single nozzle studies where a single fuel plume is developed, the fuel jets merge rapidly from multi-hole gasoline injectors, and conventional spray penetration distance and spray cone angle have little relevance to the sprays developed with multi-hole gasoline direct injectors. Consequently, alternative metrics were used in this work to characterize the spray development. Specifically, the total wetted-footprint area of the spray and the location of the centroid of the wetted area were determined as a function of time. The wetted or liquid area of the spray is considered here, as the Mie scattering technique used is associated with the location of the liquid phase. An area measurement was applied because significant asymmetry in the spray structures was evident; therefore, typical penetration distance measurements quickly lose meaning for most conditions. This is consistent with the work by Aleiferis et al. when highly asymmetric sprays were observed in their direct-injection, spark-ignition engine study [13].

For each frame in each high-speed video, the wetted-footprint area and centroid were calculated by first finding the edges of the wetted-footprint and then applying numerical integration to the defined contour. In order to find the edge of the spray in a given frame, a background detection and subtraction algorithm was applied which generated a binary image (spray versus no spray) from which the edge could be located. The process is generally illustrated for one frame in Figure 2.4. The subtraction algorithm quantitatively compares a given pixel intensity to a baseline value generated with no spray present in order to determine if a significant change is apparent. Effects of changing the sensitivity value used in the comparison, by amplification by a factor of 0.5 and 2.0, was found not to significantly affect the results of the present work.

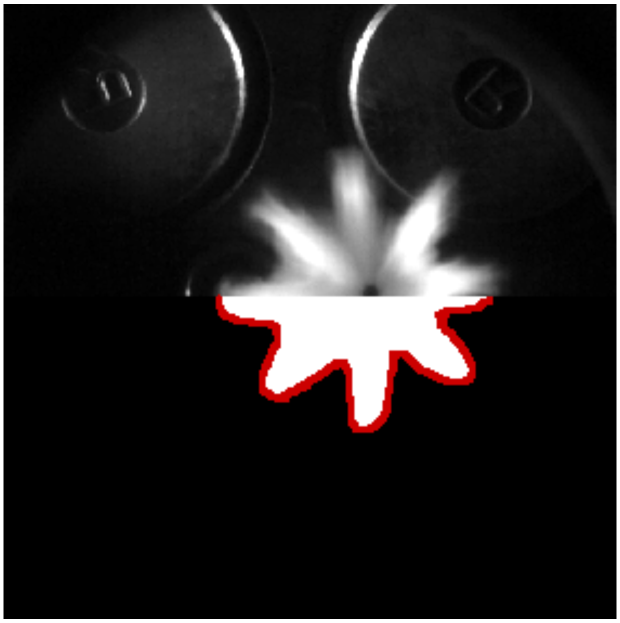

Figure 2.4. Example of spray image analysis for one frame of the single-cylinder engine data at an engine speed of 300 RPM and an intake pressure of 100 kPA. The upper half of the image is the raw data. The bottom half is the processed binary image with the spray edge identified in red.

2.4 Experimental Results and Discussion

2.4.1 Spray Morphology

Figure 2.5 and Figure 2.6 contain sets of images which illustrate the general wetted-footprint morphology for the G2-Flash boiling and G3-Non-flash boiling conditions as a function of time for a range of engine speeds. The results for 0 RPM are from the UMelbourne spray chamber.

For the G2-Flash boiling condition, individual spray plumes were evident for the 0 RPM case throughout the times considered, as shown in Figure 2.5; additional still frames are presented in Appendix 1. However, as engine speed increased to 300 RPM, for a similar time after the start of injection (SOI), distinct structure of the plumes was only weakly apparent and individual plumes were completely lost by 250 μs after SOI. As the engine speed increased to 2,000 RPM, distinct plume structures could not be identified at any time. Additionally, as engine speed increased the centroid of the footprint moved farther away from the injector tip for a given time after SOI, as shown by the green circle in Figure 2.5.

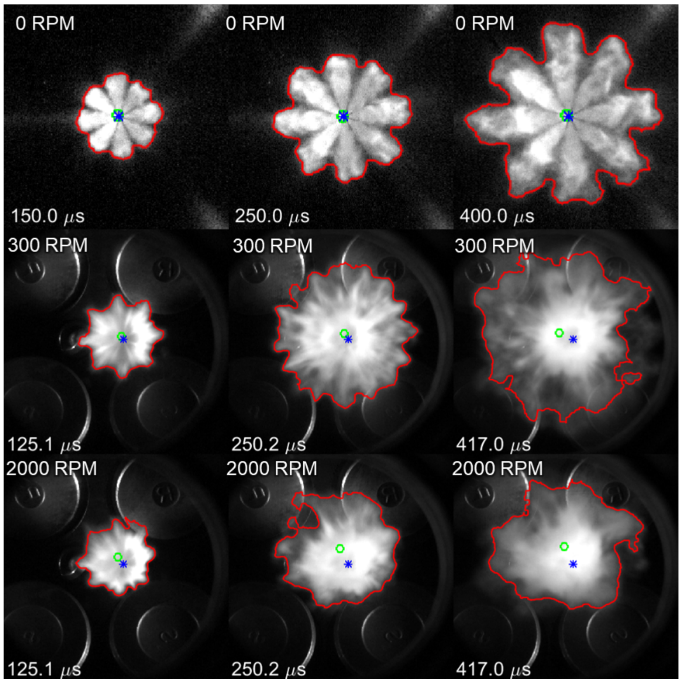

Figure 2.5. Spray wetted-footprint morphology for the G2-Flash boiling condition as a function of engine speed and time after SOI. Spray edges are marked with red, the injector tip in blue, and area centroid in green. Rows correspond to engine speeds of 0, 300, and 2000 RPM respectively at 50 kPa ambient pressure.

The centroid movement was exclusively towards the exhaust valves and spark plug, likely the result of intake charge motion. For the G3-Non-flash boiling condition (Figure 2.6), individual spray plumes were evident for all times for both the 0 and 300 RPM cases and early for the 2,000 RPM case, in contrast with the images from the flash boiling conditions presented in Figure 2.5. With respect to the centroid of the wetted-area, a similar direction and general magnitude of the shift from the injector tip was observed for the G3 condition as a function of engine speed.

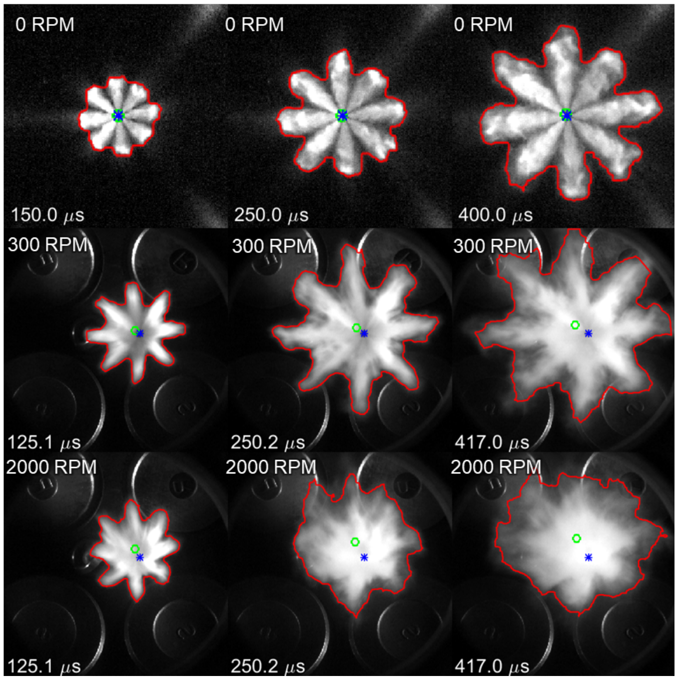

Figure 2.6. Spray wetted-footprint morphology for the G3-Non-flash boiling condition as a function of engine speed and time after SOI. Spray edges are marked with red, the injector tip in blue, and area centroid in green. Rows correspond to engine speeds of 0, 300, and 2000 RPM respectively at 100 kPa ambient pressure

Overall the evidence of enhanced spray collapse and general loss of distinct structure is in excellent agreement with findings by Aleiferis et al. [13] and Allocca et al. [8] for non-zero engine speeds, and the effects are most likely the result of increased turbulence and charge motion associated with higher piston speeds. The loss of spray structure was only evident for the non-zero speed cases for both the G2 and G3 conditions. Importantly this behavior change illustrates significant effects of a real engine which may not be observed in a quiescent spray chamber. It follows that the applicability of spray chamber behaviors to real engine performance are limited without the means to integrate the flow-field effects.

Regarding engine speed effects, the results indicate for flash boiling conditions (i.e. low- and mid-load) increasing engine speed has negligible importance on general spray structure (nearly all the sprays are collapsed continuous shapes of convolved plumes). Whereas, for non-flash boiling conditions (i.e. mid- and high-load) increasing engine speed from near idle (300 RPM) to cruising (2,000 RPM) causes the spray structure to transition from organized plumes to collapsed blobs. The results highlight the importance of considering engine speed effects on spray structures for higher load conditions of the engine operating space. Engine speed also has a distinct effect on the wetted-footprint area over time, which is illustrated below.

2.4.2 Centroid Translation

The location of the centroid of the wetted spray area provides information on the movement and general symmetry of the fuel spray. The maximum distance between the centroid of the wetted-footprint and the injector tip for all cases, from the time of SOI until the spray reached the edge of the viewable window (500-800 μs), was less than approximately 6 mm (or <12% of the diameter of the optical piston window). Because of the relatively low level of impact, specific results are not shown here. However, the result is interesting since it suggests that while some bulk movement of the wetted-footprint should be expected in the engine due to charge motion, as illustrated in Figures 2.5 and 2.6, changes in the bulk motion may be minimal. It follows that spray chamber results for penetration rates and distances may not need significant adjustment to account for bulk charge motion when applied to an engine. Considering that the Ford Zetec head used here likely generates levels of tumble and swirl realistic to production engines generally, this finding has practical significance.

2.4.3 Spray Footprint Area

Figure 2.7 and Figure 2.8 show the evolution of the values of the wetted-footprint area for the G2-Flash boiling and G3-Non-flash boiling conditions for a range of engine speeds. The results for 0 RPM are from the UMelbourne spray chamber. In both figures, the symbols indicate the average results from all image sequences and fuel injection cycles and translucent shading demarks the absolute maximum and minimum values of the wetted area for all cycles.

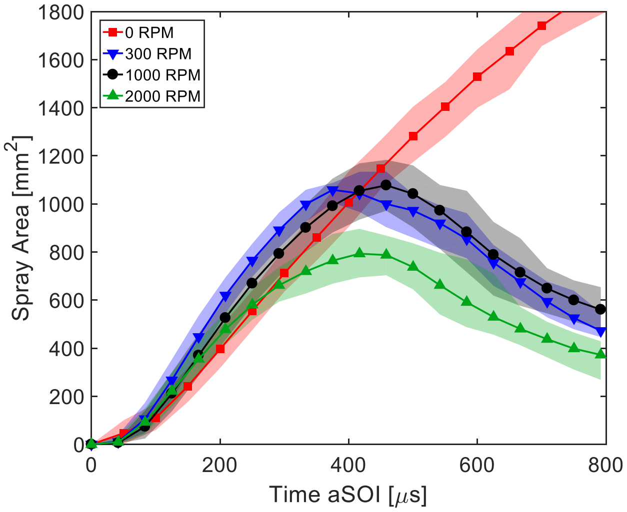

Figure 2.7. Wetted-footprint area time history for the G2-Flash boiling condition; where the symbols represent the average values and the shaded region corresponding to each line indicates the minimum and maximum observed values.

For the G2-Flash boiling condition presented in Figure 2.7, the wetted areas are not significantly different for any of the engine speeds studied until after approximately 300 μs. After this time, the 0 RPM results continue at a similar growth rate (approximately 2.5 mm^2/ μs) for times up to 800 μs; whereas, the area growth rates for the non-zero RPM conditions decrease and eventually become negative. The trend of initial agreement between the different data sets with subsequent divergence with the non-zero speed results is in excellent agreement with the penetration distance results from Allocca et al. [8]. For non-zero speed, peak spray areas for all speeds occur around 400 μs, with no significant difference in maximum values (approximately 1000 m^2) for 300 and 1,000 RPM, but a lower maximum area was observed for 2,000 RPM of 800 mm^2. For the G3-Non-flash boiling condition (Figure 2.8), the general behaviors are similar to those seen for the G2 case in Figure 2.7. Note the data stop for the non-zero speed conditions when the spray moves outside of the visible/viewable region of the piston window. Interestingly, while peak area values for non-zero speed results are indeed quite similar to the G2 conditions results, the wetted-footprint extends beyond the viewable area for 300 and 1,000 RPM at around 450 μs. Furthermore, for 2,000 RPM, the rate of area decrease after the maximum is less than for the G2 condition (approx. 0.66 mm^2/ μs compared with 1 mm^2/ μs).

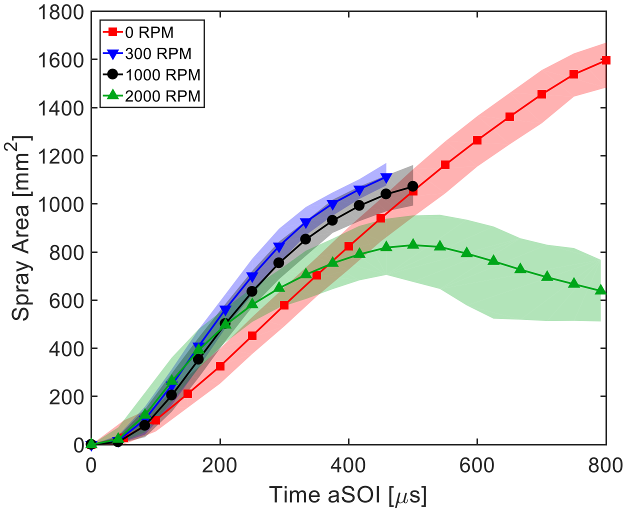

Figure 2.8. Wetted-footprint area time history for the G3-Non-flash boiling condition, where lines and symbols represent the average values and the shaded region corresponding to each line indicates the minimum and maximum observed values. Data for 300 and 1000 RPM are plotted until part of the spray escapes the field of view.

Regarding engine speed effects, it is evident the transition from zero to non-zero engine speed correlates with a marked change in behavior, from continual expansion to parabolic behavior with a maximum value on the same time scales. This certainly affects the use of spray chamber correlations for direct use in engine models. As engine speed is increased, a reduction in maximum wetted-footprint area is evident for both G2 and G3 cases, likely the result of improved vaporization and spray break-up for higher turbulence and charge motion as suggested by Aleiferis et al. [13]and Allocca et al. [8].

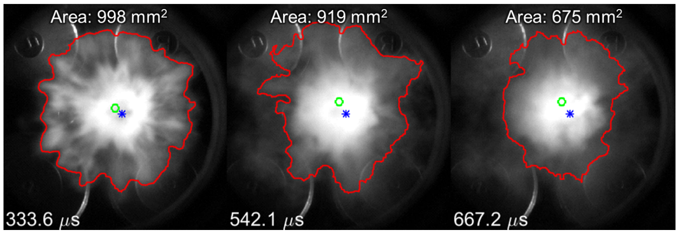

Figure 2.9. Spray wetted-footprint morphology as a function of time for one G2-Flash boiling condition. The images illustrate outer-droplet cloud-shedding and corresponding reduction of the wetted-footprint area. Spray edges are marked with a red line.

The apparent reduction in wetted-footprint area before the end of injection (EOI) seen in the present non-zero speed results is quite interesting and is likely the result of spray collapse. In fact, similar behavior in end-view imaging was seen previously in an engine with gasoline injection at 0.5 bar intake manifold air pressure and 90°C coolant temperature by Aleiferis et al. [7]. While not discussed explicitly in Aleiferis et al. [7]., inspection of the high-speed images in the present work suggests the reduction in area corresponds to the vaporization of an outer cloud of diffuse fuel droplets, i.e. spray collapse. This process is illustrated for a set of images at the G2-Flash boiling condition in Figure 2.9. Similar spray collapse behavior has indeed been observed by Xu et al. [14] in a spray chamber for gasoline fuels at flash boiling conditions, where an empirical formulation was developed relating spray structure to the ratio of ambient to fuel saturation pressure ratio. The present data offer additional insight into the flow-field effects, i.e. turbulence, on spray structure, which were not considered in the formulation by Xu et al. [14], but are clearly important based on the present results.

To assess the bias of the liquid fuel distribution introduced by the charge motion, a ratio of the wetted area found on the upper part (exhaust side) of the image, to the area on the lower part (intake side) was computed. The line separating these two areas was defined by the location of the injector tip. Based on this definition, a ratio of 1 means the spray is equally distributed, and any deviation from unity indicates the liquid is distributed asymmetrically with respect to the injector tip. Figure 2.10 and Figure 2.11 display the spray wetted-area for spray G2 and G3. As expected, the area ratio stays close to unity throughout the test for the 0 RPM case; however, as the engine speed increases, a bias on the spray distribution is introduced. For Spray G2, at non-zero velocities, the spray tends to be distributed on the upper side of the combustion chamber (i.e., the exhaust side). The lower and moderate engine speeds have a similar ratio, while the deviation tends to be higher, on average, for the highest engine speed.

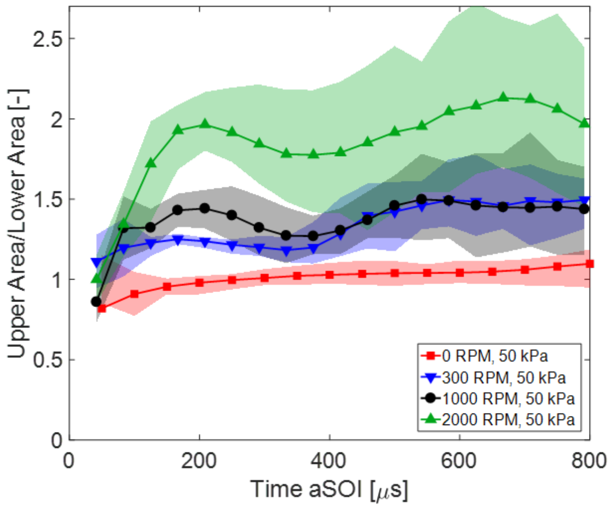

Figure 2.10. Upper to lower wetted-area ratio for Spray G2 time history for different engine speeds.

On the other hand, at non-flash boiling conditions the ratio of the upper to lower area shows a distinct behavior as a function of engine speed without much overlap between speeds. Clearly, as the engine speed increases, the spray rapidly distributes asymmetrically towards the exhaust side. This a clear indication that the charge motion generated by the intake air pushes the spray towards the opposite side, inducing a biased spray distribution. Since the intake air velocity scales with piston speed –or engine speed–, the asymmetry is stronger for the highest engine speed. Comparing the two plots for the area ratios, it is apparent that flash-boiling decreases the differences seen as a function of speed. The reason for the lower sensitivity is that the flash-boiling leads to rapid spray collapse, decreasing the bias generated by the charge motion.

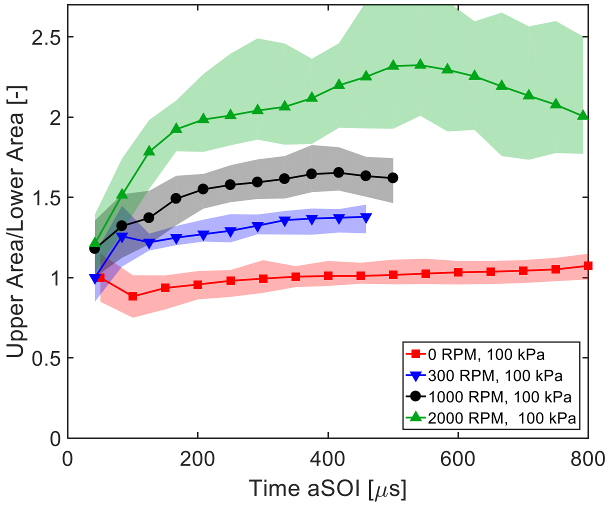

Figure 2.11. Upper to lower wetted-area ratio for Spray G3 time history for the different engine speeds.

2.5 Conclusions

The present work addresses a need to characterize, compare, and document the behaviors of fuel sprays in fundamental and repeatable experimental conditions. The results advance the mission of the Engine Combustion Network for the Spray G injector using a constant volume spray chamber and a single-cylinder engine over a range of engine speeds for two thermodynamic conditions set by the ECN and relevant to practical gasoline direct injection engines. Not unexpectedly, the present results indicated the general spray behaviors and specific characteristics differed significantly between the spray chamber and engine. The differences must be well considered when applying spray chamber results to spray model development for engine applications. Overall, increases in engine speed correlated well with enhanced vaporization, loss of distinct plume structure, and enhanced spray collapse which led to reductions in wetted-footprint area. Furthermore, while the loss of distinct plume structures appeared to be strongly dependent on ambient thermodynamic conditions, the relative impact of the spray collapse on wetted-footprint area was small. Of practical importance, while the spray chamber results indicated a consistent increase in wetted-footprint area through the end of injection, sprays in the engine underwent significant spray collapse and resulted in a parabolic area time history, with maximum values far less than the spray chamber values.

2.6 Abbreviations

bTDC	Before top dead center
CAD	Crank angle degree
CVC	Constant volume chamber
DISI	Direct injection spark ignition
ECN	Engine Combustion Network
RPM	Revolutions per minute
SOI	Start of injection
TDC	Top dead center
UofM	University of Michigan
UMelbourne	University of Melbourne

References

[1] Engine Combustion Network, "ECN5 Procedings." [Online]. Available: https://ecn.sandia.gov/ecn-workshop/ecn5-workshop.

[2] Engine Combustion Network, "Spray G Operating Conditions." [Online]. Available: https://ecn.sandia.gov/gasoline-spray-combustion/target-condition/spray-g-operating-condition/.

[3] J. Manin, Y. Jung, S. A. Skeen, L. M. Pickett, S. E. Parrish, and L. Markle, "Experimental Characterization of DI Gasoline Injection Processes," 2015.

[4] J. Lacey *et al.*, "Generalizing the behavior of flash-boiling, plume interaction and spray collapse for multi-hole, direct injection," *Fuel*, vol. 200, pp. 345–356, 2017.

[5] L. Allocca, A. Montanaro, and G. Meccariello, "Effects of the Ambient Conditions on the Spray Structure and Evaporation of the ECN Spray G," 2019, pp. 1–11.

[6] D. Paredi *et al.*, "Combined Experimental and Numerical Investigation of the ECN Spray G under Different Engine-Like Conditions," in *SAE Technical Paper Series*, 2018, vol. 1, pp. 1–15.

[7] P. G. Aleiferis, J. Serras-Pereira, Z. van Romunde, J. Caine, and M. Wirth, "Mechanisms of spray formation and combustion from a multi-hole injector with E85 and gasoline," *Combust. Flame*, vol. 157, no. 4, pp. 735–756, Apr. 2010.

[8] L. Allocca, F. Catapano, A. Montanaro, P. Sementa, and B. M. Vaglieco, "Study of E10 and E85 Effect on Air Fuel Mixing and Combustion Process in Optical Multicylinder GDI

Engine and in a Spray Imaging Chamber," in *SAE Technical Paper Series*, 2013, vol. 1.

[9] Y. Bao, Q. N. Chan, S. Kook, and E. Hawkes, "Spray Penetrations of Ethanol, Gasoline and Iso-Octane in an Optically Accessible Spark-Ignition Direct-Injection Engine," *SAE Int. J. Fuels Lubr.*, vol. 7, no. 3, pp. 2014-01–9079, Nov. 2014.

[10] M. Fatouraie, M. S. Wooldridge, B. R. Petersen, and S. T. Wooldridge, "Spray Development and Wall Impingement of Ethanol and Gasoline in an Optical Direct Injection Spark Ignition Engine," in *Volume 1: Large Bore Engines; Fuels; Advanced Combustion*, 2015, p. V001T02A004.

[11] B. T. Zigler, S. M. Walton, D. Assanis, E. Perez, M. S. Wooldridge, and S. T. Wooldridge, "An Imaging Study of Compression Ignition Phenomena of Iso-Octane, Indolene, and Gasoline Fuels in a Single-Cylinder Research Engine," *J. Eng. Gas Turbines Power*, vol. 130, no. 5, p. 052803, 2008.

[12] K. Saha, S. Quan, M. Battistoni, S. Som, P. K. Senecal, and E. Pomraning, "Coupled Eulerian Internal Nozzle Flow and Lagrangian Spray Simulations for GDI Systems," in *SAE Technical Paper Series*, 2017, vol. 1.

[13] P. G. Aleiferis *et al.*, "Optical studies of spray development in a quiescent chamber and in a direct-injection spark-ignition engine," *Int. Conf. Intern. Combust. Engines Performance, Fuel Econ. Emiss. IMechE, London, 11-12 December*, pp. 3–13, 2007.

[14] M. Xu, Y. Zhang, W. Zeng, G. Zhang, and M. Zhang, "Flash Boiling: Easy and Better Way to Generate Ideal Sprays than the High Injection Pressure," *SAE Int. J. Fuels Lubr.*, vol. 6, no. 1, pp. 2013-01–1614, Apr. 2013.

Chapter 3

Cycle-to-cycle Analysis of Non-reactive Spray Stucture Using Proper Orthogonal Decomposition

3.1 Introduction

Stochastic behavior is a defining characteristic of internal combustion (IC) engines. Processes like gas exchange, fuel injection, charge motion and mixing, ignition, and combustion are dominated by intrinsically unsteady and/or chaotic phenomena like turbulence, atomization, and chemical reactions [1], [2]. When the effects of random events become significant, they can lead to noticeable differences from one cycle to another, introducing inconsistencies in performance and potentially increasing engine emissions At the extreme, intense cycle variability leads to poor combustion stability, partial burns, and misfires , which leads to higher engine emissions [3], [4]. Ozdor et al. [2] estimated that a 10% increase in efficiency would be achieved if the cycle-to-cycle variability (CCV) could be minimized. Additionally, the cycle variability translates to poor drivability and louder engine noise, since fluctuations in energy release induces power output variations as well as pressure oscillations [2], [5]–[7].

In direct injection spark ignited (DISI) engines, the shorter times available for injection, vaporization, and mixing, combined with higher fuel injection velocities, intensify the magnitude and tendency of CCV [6]. Fluctuations of the local equivalence ratio and charge flow are a result of the liquid jet injection processes [1], [2], [5], [8]. Therefore, understanding how the spray behavior and structure varies as a function of operating parameters and conditions is crucial to mitigate the adverse of effects of CCV.

Engine stability –or variability, in this case– can be measured by computing the coefficient of variation (COV) of the indicated mean effective pressure (IMEP) derived from in-cylinder pressure measurements. This metric is commonly reported as a way to characterize the CCV of a particular engine at a given condition [4], [6], [9]. However, optically-accessible engines and constant volume chambers (CVC) allow more in-depth understanding of in-cylinder processes and can be used to provide new insight into physical characteristics of cycle variability.

Spray behavior during fueling has been identified as one of the sources of CCV [5], [6]. Fuel sprays have been extensively studied through direct imaging in optical engines and quiescent chambers as discussed in Chapter 2. However, predictive understanding of sprays at conditions present in production engines and the effect of operating conditions are still lacking. Serras-Pereira et al. [10] and Marchi et al. [11] used the mean and root mean square of spray images of multiple cycles to identify physical regions of high variation in the combustion chamber. A different approach, based on the probability of liquid location distribution, has been used by other authors to study the consistency of spray structure [12]. More recently, the proper orthogonal decomposition (POD) has been proposed to study CCV of sprays and other stochastic phenomena that can be imaged in optical engines or generated through computational simulations [3], [7], [8], [13], [14].

The POD is part of a broader set of techniques for dimensional reduction of data sets with a large number of components [15], [16]. The method excels at reducing the complexity of high-dimensional data and has, therefore, been applied to large experimental and computational data sets to understand engine phenomena [6], [14], [17]. Compared with the other techniques mentioned, the advantage of the POD method resides in its capacity to eliminate statistical noise from experimental and computation data [18]. The POD separates coherent structures from fluctuations that do not contribute significantly to the behavior of the ensemble data set [15], [19].

The POD procedure has been recently applied to study multiple engine phenomena. Wu et al. [6] studied the effects of fuel temperature and injection pressure on the CCV of a spray in a CVC using the POD method. Chen et al. [20], [21] used orthogonal decomposition to explore the connection between cycle variability of in-cylinder flow, misfires, and the resulting combustion characteristics. Using orthogonal decomposition of combustion imaging, Bizon et al. [22] were able to discriminate between normal and incoherent fluctuations in the luminosity field of the images, and then connect the fluctuations to the CCV in the heat release. Moreover, Fogleman et al. [23] exploited the versatility of the POD method to bridge between experiments and simulations of in-cylinder flows with the objective of increasing the accuracy and reliability of computational tools. The objective of the present study was to explore the effects of engine speed and fuel flash boiling on the variability of liquid fuel distribution using the POD method on in-cylinder spray imaging data.

3.2 Experimental Method and Data Processing

3.2.1 Experimental Approach

The high-speed imaging spray data used for this study are the same as the visualization results used and presented in Chapter 3 on the Spray G injector from the Engine Combustion Network (ECN). As a reminder, three engine speeds (300, 1000, and 2000 RPM) and two manifold pressures (50 kPa and 98 kPa) were considered; the lower pressure induces flash boiling on the spray. Imaging data for the spray injection of 20 cycles was used for the CCV analysis. A summary of the experimental conditions and experimental setup is presented in Table 3.1.

Table 3.1. Experimental conditions for high-speed imaging of Spray G2 and G3

Variable	Spray G2	Spray G3
Manifold Pressure	50 kPa	98 kPa
Ambient Temperature	60°	
Engine speeds	300, 1000, and 2000 RPM	
Fuel	Iso-octane	
Fuel Pressure	20 MPa	
Fuel Temperature	90° C	
Start of injection	270° bTDC	
Image Resolution	512×512	
Frame rate / Period	22,500 fps / 40 μs per frame	

3.2.2 Fundamentals of the Proper Orthogonal Decomposition Method

From the historical perspective, the POD method was developed and introduced simultaneously by multiple people in different fields and, therefore, is known by different names depending on the context [24]. These names include the Karhunen-Loève transform, principal component analysis, Hotelling transform, and empirical orthogonal function [15], [19], [24], [25]. The POD also has a direct relation to the singular value decomposition (SVD), which is commonly used in applications for reducing information redundancy and noise in data sets [24], [26]. The use of this procedure in the context of fluid dynamics was originally proposed by Lumley [19] as tool to identify coherent structures in turbulent flows.

In essence, the POD procedure decomposes the input data set into a linear combination of an orthonormal basis. The obtained basis functions are also called modes, and they are the optimal representation of the data in the L2-norm sense (i.e. they minimized the Euclidean error) [15], [27]. The POD modes capture the dominant features or trends in the data and, in the context of fluid dynamics, they represent the coherent structures of a –scalar or vector– field, such as velocity fields, flame luminosity patterns, or the distribution of liquid jets [13], [17], [19], [28].

Although the orthogonal decomposition can be applied to general continuous functions, the discrete treatment will be now discussed and used in this study. Moreover, the discussion of the method will be framed in the context of application to imaging data. Specifically, the approach referred as the method of snapshot [29] is presented here. For a more complete and fundamental description of the mathematical derivation and properties of the POD, the reader is encouraged to consult Holmes et al. [19] and Towne et al. [16].

The snapshot method is commonly used to analyze data sets in which a quantity of interest is repeatedly measured at multiple locations and at different instances. In an imaging experiment repeated K times, the gray scale images obtained represent discrete scalar fields. Each snapshot can be expressed as $z_k(x)$, where the k index represents the index of the realization, ranging from 1 to K, and x spans the $M{\times}N$ pixels in a digital image.

To apply the POD analysis, the vectorial representation of each snapshot is stalked as columns of an ensemble matrix $\boldsymbol{Z}$ that contains the complete experimental data set:

$$\mathbf{Z} = [\mathrm{z}_1, \mathrm{z}_2\,, \dots\,, \mathrm{z}_\mathrm{K}] \tag{4.1}$$

In geometric terms, each of the columns z_k –i.e., each of the images– is a vector in a $\mathbb{R}^{M\times N}$ Hilbert space, where each pixel is treated as a dimension. That means that for an image with a resolution of 512×512, every frame represents a location in a $512^2 = 262144$ dimensional space. In such a space, some of the dimensions may be redundant or have little variability between images. Hence, it is of interest to find a more appropriate basis capable of capturing the dominant components contained in the set. For example, the kth image can be expressed as a linear combination of an arbitrary basis ϕ_i and the associated linear weights a_{ik}

$$z_k(x) = \sum_{i=1}^{K} a_{ik}\phi_i(x)$$

(4.2)

Expression 4.2 does not have a unique solution. However, if the basis vectors $\phi(x)_i$ are derived through the POD, the optimal basis set can be obtained. The basis vectors are optimal in the sense that the vectors correspond to the direction of maximum variance in the data set. These orthonormal basis vectors are commonly called POD modes or eigenmodes, and the coefficients a_{ik} are referred to as the modal coefficients. In practical terms, the POD modes $\phi(x)_i$ describe the coherent structures present in the ensemble set $\boldsymbol{Z}$, while the modal coefficients a_{ik} indicate how strong or dominant the ith mode is in the kth snapshot [18]. The modes can also be thought of as directions in the Hilbert space, and the coefficients as "distances" one has to travel in those directions to get to the kth image. Hence, the modes capture the spatial patterns, and the coefficients indicate the amplitude of those spatial patterns.

As mentioned before, the modes obtained through POD are the optimal basis in the least square sense (or the L-2 norm) [15], [18], [24]. In fact, for any $r < K$, the subset $\{\phi(x)_1, \dots, \phi(x)_r\}$ forms the best subspace or truncated approximation of dimension r since

$$\sum_{k=1}^{K} \left\| z_k(x) - \sum_{i=1}^{r} a_{ik}\phi_i(x) \right\|^2 \rightarrow min$$

(4.3)

There are two common approaches to find both the POD modes and their respective coefficients. The first involves computing the covariance matrix of $\boldsymbol{Z}$, solving its eigenvalue problem, and finally projecting the original snapshots onto the obtained eigenvectors. A complete description of this process can be found in the study by Hao et al. [30]. However, a more direct and faster method [15] is computing the singular value decomposition (SVD) of the ensemble data matrix $\boldsymbol{Z}$, through which we get the matrices $\boldsymbol{U}$, $\boldsymbol{\Sigma}$, and $\boldsymbol{V}$, such that:

$$\boldsymbol{Z} = \boldsymbol{U\Sigma V}^T \tag{4.4}$$

Conveniently, the columns of the matrix $\boldsymbol{U}$ are the POD modes $\phi(x)_i$, and the modal coefficients can be obtained by the matrix multiplication of $\boldsymbol{\Sigma}$ and $\boldsymbol{V}$. A second useful feature of equation 4.4 is that the matrix $\boldsymbol{\Sigma}$ contains the singular values σ_i of the $\boldsymbol{Z}$ matrix, which are associated with each of the ϕ_i modes. Both the singular values and the modes appear arranged in decreasing order (i.e., $\sigma_1 \geq \sigma_2 \geq \ldots \geq \sigma_K$), such that the first mode, ϕ_1, has the highest singular value, σ_1. This is useful because the singular value (and the associated eigenvalue, $\lambda_i = \sigma_i^2$) indicates how much of the energy is captured by the ith mode. Therefore, the first mode describes the strongest features, followed by the second mode, and so on. The highest modes tend to capture only the statistical noise. It should be mentioned that the concept of energy in this context does not refer to the thermodynamic property, but rather to the "information" or total norm of the data set [15], [24], [26].

A common metric to understand how the energy is distributed between the modes is computing the energy fraction E_i of each mode [16]

$$E_i = \frac{\lambda_i}{\sum \lambda_j} \tag{4.5}$$

In a repeatable imaging experiment (i.e., one with consistent snapshots), the image vectors cluster and point in the same direction, so the POD would have most of the energy concentrated in the first few modes. On the contrary, significant variation in the data set translates to a larger span of the space, and therefore, more modes are needed to resolve the differences between the images; meaning that the energy fraction of higher modes would increases accordingly. Therefore, the energy fraction distribution can be used to measure CCV in engines in a quantitative way that is not only easy to present, but also captures the complex spatial features present in the imaging data.

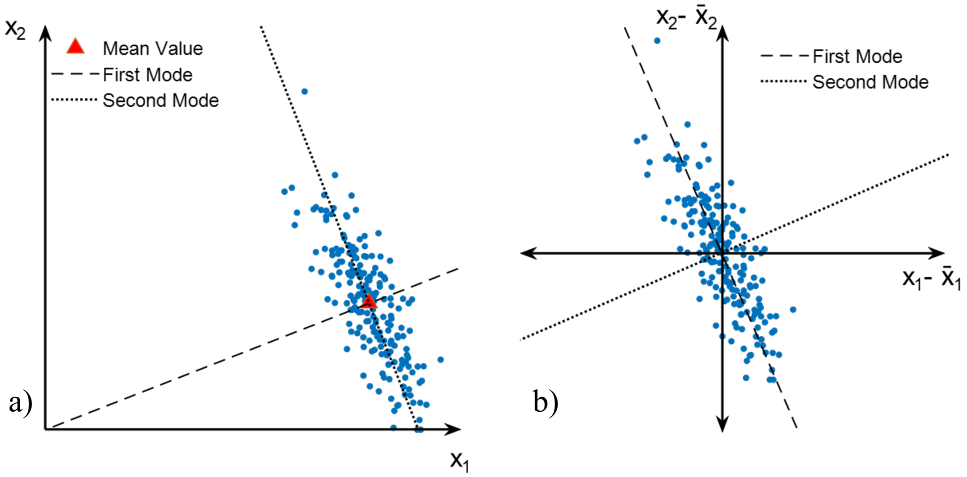

Figure 3.1. Effect of subtracting the ensemble average: a) random data set and POD modes with no mean-subtraction, b) random data with POD modes after subtracted mean values

One final and important consideration is the effect that subtracting the ensemble mean has on the interpretation of the computed POD modes. In most cases, the average value tends to be large compared with the variations present in the data set, so if it is not subtracted, the first mode tends to represent the mean behavior [31]. In this case, the second mode represents the direction of higher variability. However, if the ensemble mean is subtracted from the data matrix $\boldsymbol{Z}$, then, the first mode is interpreted as the structure of higher variance. Figure 3.1 shows an example of the effect of performing this translation on a random 2-D data set. The second mode in Figure 3.1a (the data without mean-subtraction) is the same as the first mode in Figure 3.1b, which has been translated by subtracting the average value. Both approaches have useful features, so in the present study, the two methods are used for different purposes, as discussed in the following sections.

3.3 Experimental Results and Discussion

3.3.1 Time-dependent cycle-to-cycle variability of fuel sprays

To understand how the CCV evolves throughout the injection event at each condition, the POD method was applied to the ECN spray-imaging data as a function of time. The process consisted of building an ensemble matrix of the first frame after start of injection (SOI) of all cycles, applying the orthogonal decomposition algorithm to the matrix, computing the energy fraction for each of the POD modes, and finally advancing in time by moving to the next frame after SOI and repeating the previous steps.

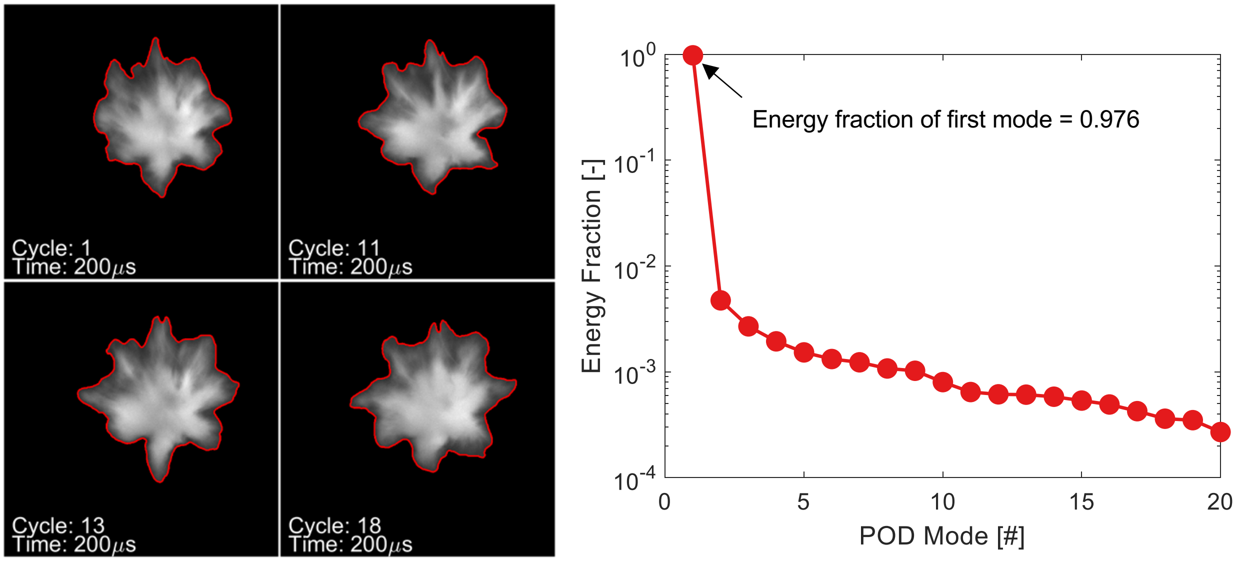

Figure 3.2. *Left*: Spray structure at 200 μs after SOI for four of the 20 cycles. *Right*: Energy fraction for 20 POD modes at time 200 μs after SOI.

As an example, Figure 3.2 shows the snapshots at 200 μs after SOI for four of the 20 cycles at the condition of 2000 RPM and 98 kPa. On the right, Figure 3.2 plots the energy fraction of the 20 POD modes obtained at that instant in time; how the energy is distributed changes depending on how consistent –or inconsistent– the spray distribution is at a particular time. For this part of the study, the ensemble mean was not subtracted from the data set; therefore, the first mode describes the average spray structure. In this case, a first mode with a high-energy fraction indicates that the pattern of the spray is consistent from one cycle to another. This fact indicates there is little variability between the cycles, so the first mode is able to capture most of the ensemble behavior. Conversely, a lower first-mode energy fraction indicates the differences in the spray morphology are more complex, and higher modes are needed to capture the variance in the data set [5], [6], [23].

Figure 3.3 shows the time evolution of the energy fraction of the first POD mode for the sprays at a manifold pressure of 98 kPa and the three engine speeds tested. The results display similar trends. The first mode energy is lower at the early part of the injection, and then this fraction increases as the sprays penetrates and develops. The behavior indicates there is significant CCV of the initial spray structure (the first three data points of each curve), and the differences tend to decrease as the spray evolves. The reason for this behavior is explored in Section 3.3.2 in more detail, and is due to differences in spray penetration between the cycles caused by small discrepancies between the physical SOI and the first imaging frame. In other words, the CCV is due to the fidelity of the imaging.

A second observation is that the energy of the first mode is higher for the lowest engine speed, indicating the spray morphology is more consistent–i.e., lower spray CCV at lower engine speeds. As the engine speed increases to 2000 RPM, the energy of the first mode decreases compared with the 300 RPM case, indicating the differences in spray distribution from cycle-to-cycle become more complex and significant, and thus require higher modes to resolve the CCV. The midrange speed, 1000 RPM, falls between the two extremes for most injection events. The results indicate that the variability in spray structure becomes more significant as the in-cylinder flow increases with engine speed. While increased turbulence might be expected to dissipate structures and therefore reduce CCV, the data indicates increasing turbulence increases stochastic spray distribution at the scales of the imaging used here.

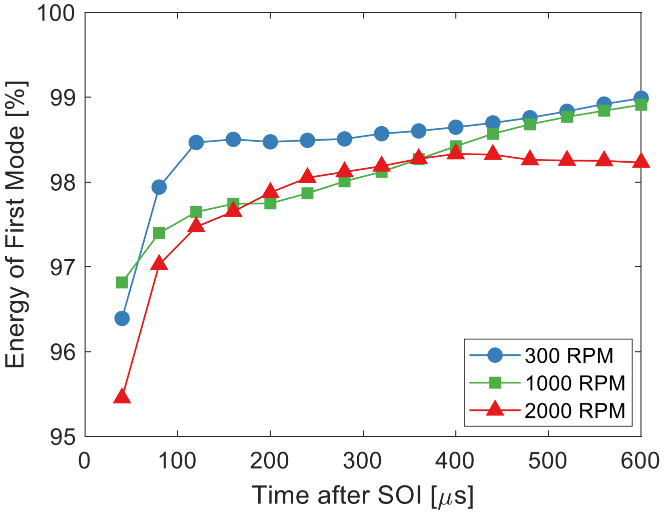

Figure 3.3. Energy of the first POD as a function of time for three engine speeds at manifold pressure of 98 kPa (Spray G3 - non-flash boiling condition)

Figure 3.4 shows the time evolution for the first mode energy at the lower manifold pressure, which induces flash boiling. The energy of the first mode shows consistent dynamics for the three engine speeds, with a local maximum early in the injection event (around 120 µs), followed by a slight decrease, which is followed by a second maximum at the later phase of the injection. The results are quite different compared with the non-flash boiling case shown in Figure 3.2. Consequently, the behavior is attributed to the effects of flash boiling on the spray morphology and the evolution of the spray. In Chapter 2, the imaging data showed that flash boiling induces spray collapse and the detachment of an outer layer of the plume. However, the process is not instantaneous, as during the early stages of the injection the plumes do not interact with each other. Once the effects of plume interaction become significant, the spray collapses [32]. This phenomenon introduces additional sources of CCV, since the sprays can collapse at different rates and form diverse spatial patterns when comparing cycles. In fact, visual inspection of the imaging data showed that the sudden drop in first mode energy coincides with the onset of the spray collapse, indicating the increase in inter-cycle variability is associated with the spray collapse process.

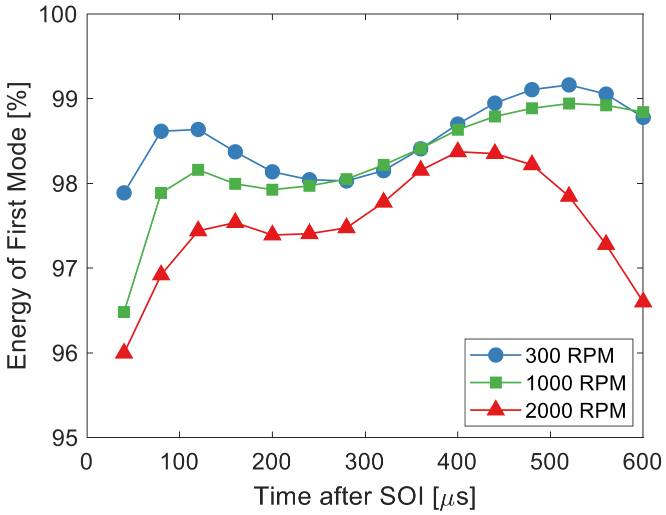

Figure 3.4. Energy of the first POD as a function of time for three engine speeds at manifold pressure of 50 kPa (Spray G2 - flash boiling condition)

Comparing data from the three engine speeds at flash boiling conditions, the energy of the first mode decreases with increasing speed in the same way as discussed previously for the non-flash boiling case. Again, the higher first mode energy percentage at the lower speed condition implies the spray structure is more consistent from cycle-to-cycle, whereas for the higher engine speed, the first mode has lower energy fraction. The intermediate speed data are between the other two data sets, although closer to the lower speed data for most of the later part of the injection. Wu et al. [6] reported that flash boiling can decrease the differences in spray distribution after spray collapse. The results for the low and intermediate speed after the spray collapse (after ~300 µs) support this proposition, as the sprays become more consistent.

3.3.2 Time-coherent cycle-to-cycle variability of fuel sprays

The snapshot method used in the previous sections serves well to understand how the spatial CCV develops, but since the POD is applied independently at each instant in time, the analysis has no "memory" of what happens from frame to frame. In that sense, the eigenmodes obtained can only capture the spatially coherent trends, but they are temporally disconnected from each other, –i.e., the temporal connections exist only implicitly within the evolution of the raw data. In that sense, the snapshot method represents a spatial-only version of the POD. Using the more general definition, the POD technique can be used to explicitly include the time-coherent structures contained in a data set [19].

Interest in developing and applying a more generalized version of the POD to obtain spatio-temporal understanding of turbulent flows and other transient data has recently grown in popularity. This include the development of the temporal POD (TPOD) and the space-time POD methods [33]–[35]. Since the fuel sprays commonly display strong transient behavior, the space-time POD is an appropriate tool for this study. Using the space-time POD variant enables the capture and observation of statistical structures of the spray with spatial and temporal coherence.

The implementation of the space-time POD is similar to that of the snapshot method. The difference is that, in this case, the matrix $\mathbf{Z}$ *is made by vectorising the frames for the* ith *realization and sequentially stacking the vectors as a column, starting with the frame at time zero* $z_i^{t_0}$ *to* $z_i^{t_f}$*. By doing so, the space-time matrix* $\mathbf{Z}$ *is obtained:*

$$\mathbf{Z} = \begin{bmatrix} z_1^{t_0} & z_2^{t_0} & \cdots & z_K^{t_0} \\ z_1^{t_0+\Delta t} & z_2^{t_0+\Delta t} & & z_K^{t_0+\Delta t} \\ \vdots & \vdots & \ddots & \vdots \\ z_1^{t_f} & z_2^{t_f} & \cdots & z_K^{t_f} \end{bmatrix} \tag{4.6}$$

The rest of the process is identical to the one previously described. The SVD is applied to the **Z** matrix and the eigenmodes are obtained, singular values, and modal coefficients. Nonetheless, by including the complete data evolution in the decomposition, the eigenmodes $\phi_i(x,t)$ obtained are explicitly dependent on time, not only on space, and therefore are called space-time POD modes [35].

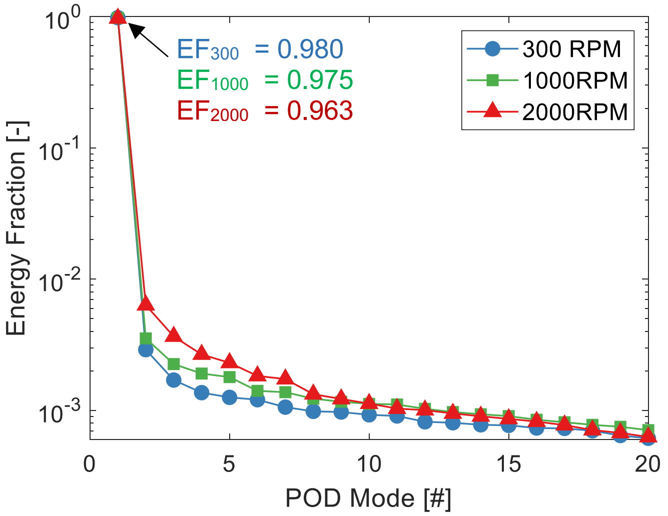

Figure 3.5. Energy fraction for the 20 space-time POD modes for the three engine speeds and a manifold pressure of 98 kPa (Spray G3 - non-flash boiling condition).

Just as before, the analysis was applied to the spray imaging data for the different engine speeds and manifold pressures. The eigenvalues were used to compute the energy fraction for the space-time modes. It is worth mentioning that, when applying the space-time POD, the energy that each mode captures represents how strong the structures are throughout the complete injection event and rather than at a particular instance in time. Figure 3.5 plots the energy fraction for the space-time modes of the three engine speeds at a manifold pressure of 98 kPa. For the first part of the analysis, the ensemble mean was not subtracted, so the first mode captures the average spray structure. The energy distribution follows the same trend as shown in Figure 3.3; that is, as engine speed increases, more modes are needed to resolve the differences between cycles. The behavior shows the increase in charge motion generated by higher engine speeds induces a stronger inter-cycle variability to the spray distribution.

Figure 3.6 presents the energy distribution for the 50 kPa pressure tests. Again, the overall CCV show similarities to the time-histories shown in Figure 3.4. The lower and medium speeds (300 and 1000 RPM, respectively) show similar behavior, indicating that flash boiling diminishes differences induced by turbulence at low and moderate engine speeds.

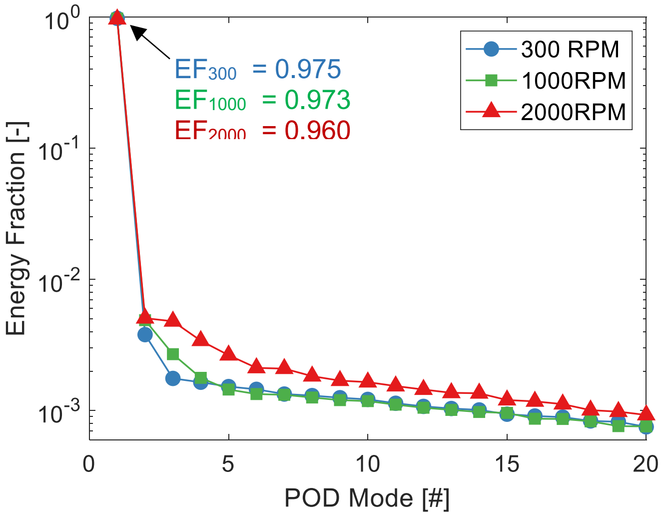

Figure 3.6. Energy fraction for the 20 space-time POD modes for the three engine speeds and a manifold pressure of 50 kPa (Spray G2 - flash boiling condition)

An important feature of the space-time POD is that the modes can be used to visualize and understand how spatial inter-cycle differences evolve with time. For this part of the analysis, the ensemble mean was subtracted from the data set. Therefore, the first mode represents the most statistically significant spatial differences between the cycles, and not the average structure, as previously shown and discussed in Figure 3.1.

A couple comments should be made about the mode plots before describing the results. First, the modes obtained through the POD analysis are normalized unit vectors; they are only direction vectors, and the modal coefficients capture the distance or amplitude of the directions.

Consequently, one has to be careful at assigning a physical meaning to the plots. Second, when visualizing the eigenmodes, the projections of the modes onto the original pixel grid are obtained. As seen in Figure 3.1b, if the data are spread widely through mode, positive and negative values are possible when projecting back to the original grid. Alternating patterns (positive to negative and vice versa) indicate opposing behaviors present between the different cycles with respect to the average.

With these remarks in mind, the first modes for the 98 kPa experiments are shown in Figure 3.7; results for higher modes can be found in Appendix 2. Each row represents a different engine speed starting with the lowest speed, and each column represents an instant in time after SOI. The regions in white show the spatial locations with low CCV, while the red and blue indicate the patterns of high fluctuation on the spray distribution from cycle-to-cycle. The results show that at the low engine speed (300 RPM), the CCV is concentrated at the edges of the spray, indicating that the variability is mainly in the spray penetration distance. Additionally, the fluctuations are equally distributed throughout the eight plumes. For the moderate speed (1000 RPM), the initial behavior is similar, since the fluctuations are concentrated at the edges; but at 120 μs, blue regions appear at the bottom three plumes (as noted in the previous chapter, those plumes are closer to the intake valves). The difference in color indicates that the variations with respect to the average pattern alternate between cycles. In physical terms, it means that for some cycles, those plumes move to the left (red region), while in other cycles they move to the right (blue region), with respect to the average. Hence, as the engine speed increases, the fluctuation in spray penetration is coupled with variability in plume orientation, and the variations grow as the spray develops. Finally, for the highest speed, the variability in plume orientation emerges as soon 80 μs. The alternating fluctuations are concentrated especially on the intake side again. The rest of the CCV is distributed throughout the spray, and not concentrated only at the edges. The results show that the intake air inflow has a direct impact on the spray CCV and on how the variability is spatially distributed.

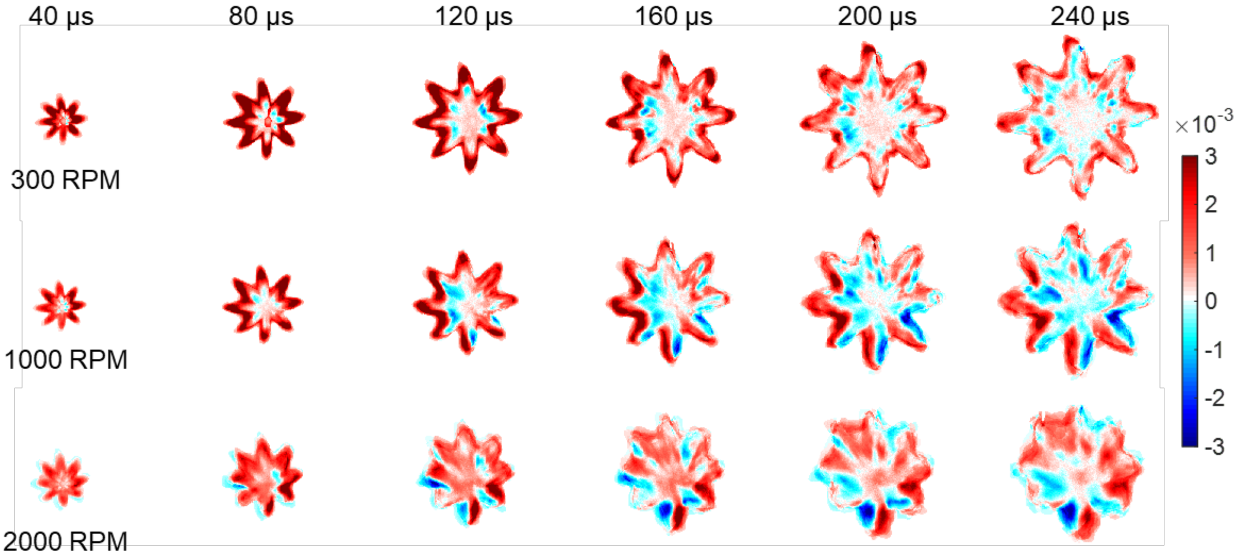

Figure 3.7. Time-evolution of the first space-time POD mode at 98 kPa (non-flash boiling). Each row corresponds to a different engine speed. The mean ensemble has been subtracted before performing the decomposition.

Similarly, Figure 3.8 shows the first mode for the 50 kPa experiments, which experienced fuel flash boiling. For the three speeds, at this condition, fluctuations appear radially distributed through the plume. At around 120 µs, a region appears at the core and grows towards the edge of the spray as the spray penetrates into the chamber. This event coincides with the increase in CCV discussed in Figure 3.4. Furthermore, the evolution of the first mode for the low and moderate speeds is similar for both cases, in agreement with the results shown in Figure 3.4 and Figure 3.6. The behavior indicates that at lower speeds, the flash boiling effectively decreases the impact of charge motion on CCV, since the region closer to the intake valves does not show perturbations compared with other areas of the spray. For the highest engine speed, the CCV is distributed throughout the plume, and there is no clear region of concentrated variability.

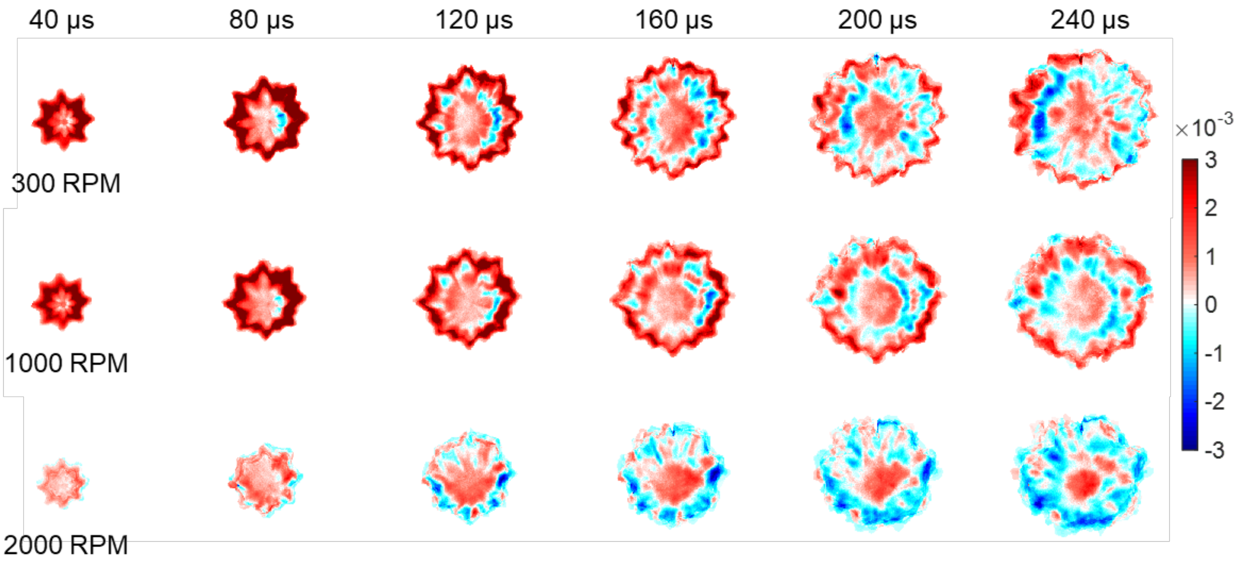

Figure 3.8. Time-evolution of the first space-time POD mode at 50 kPa (flash boiling). Each row corresponds to a different engine speed. The mean ensemble has been subtracted before performing the decomposition

3.4 Conclusions

Cycle-to-cycle variability (CCV) has a significant impact on engine performance and emissions. Higher CCV is associated with poor vehicle drivability, lower efficiency, and increased noise and emissions. Spray behavior plays a key role in controlling cycle variability, especially in direct injection engines. This study used two POD methods to analyze and describe the variance of fuel spray structure at different engine speeds and manifold pressures. Results of the on the analysis support the following conclusions:

- For the higher manifold pressure, the snapshot POD showed that as the engine speed increased, the CCV in spray structure became more significant. A similar trend was observed for the lower manifold pressure; however, the difference between the low and moderate speed decreased at this condition due to fuel flash boiling.

- At flash boiling conditions, the time-history of the CCV showed a sudden increase in variability that coincided with the time of plume collapse. The higher the inter-cycle variability was attributed to the rate of spray collapse and the resulting complex structures.
- The space-time POD technique was used to detect spatiotemporal coherent features. In general, the modal energies followed similar trend as the ones obtained using the snapshot method.
- The time-evolution of the first space-time mode showed that at the lowest engine speed, the differences between cycles were concentrated at the edges of the plumes (i.e., variance in spray penetrations). However, as the engine speed increased, differences in plume orientation appeared early in the injection event, and grew as the spray developed.
- At fuel flash-boiling conditions, the variability in spray structure was radially distributed through plume. The results indicate differences in the structure generated during the spray collapse were responsible for the sudden increase in CCV observed.

3.5 Abbreviations

bTDC	Before top dead center
CCV	Cycle-to-cycle variability
COV	Coefficient of variation
CVC	Constant volume chamber
DISI	Direct injection spark ignition
ECN	Engine Combustion Network
IMEP	Indicated mean effective pressure
POD	Proper orthogonal decomposition
RPM	Revolutions per minute
SOI	Start of injection
SVD	Singular value decomposition
TPOD	Temporal proper orthogonal decomposition

References

[1] M. Theile, E. Hassel, D. Thévenin, B. Buchholz, K. Michels, and M. Hofer, "Analysis of Cycle-to-Cycle Variations of the Mixing Process in a Direct Injection Spark Ignition Engine

Using Scale-Resolving Simulations," *SAE Int. J. Engines*, vol. 9, no. 4, pp. 2320–2336, 2016.

[2] N. Ozdor, M. Dulger, and E. Sher, "Cyclic Variability in Spark Ignition Engines A Literature Survey," *SAE Tech. Pap. Ser.*, vol. 1, no. 412, 2010.

[3] H. Chen, D. L. Reuss, and V. Sick, "Analysis of misfires in a direct injection engine using proper orthogonal decomposition," *Exp. Fluids*, vol. 51, no. 4, pp. 1139–1151, Oct. 2011.

[4] B. Peterson, D. L. Reuss, and V. Sick, "High-speed imaging analysis of misfires in a spray-guided direct injection engine," *Proc. Combust. Inst.*, vol. 33, no. 2, pp. 3089–3096, Jan. 2011.

[5] H. Chen, D. L. S. Hung, M. Xu, and J. Zhong, "Analyzing the Cycle-To-Cycle Variations of Pulsing Spray Characteristics By Means of the Proper Orthogonal Decomposition," *At. Sprays*, vol. 23, no. 7, pp. 623–641, 2013.

[6] S. Wu, M. Xu, D. L. S. Hung, T. Li, and H. Pan, "Analyzing the Cycle-to-Cycle Variations of Vapor and Liquid Phases of Evaporating SIDI Sprays via Proper Orthogonal Decomposition Technique," *SAE Int. J. Engines*, vol. 9, no. 1, pp. 2015-01–1901, Sep. 2015.

[7] W. Qin, M. Xie, M. Jia, T. Wang, and D. Liu, "Large eddy simulation and proper orthogonal decomposition analysis of turbulent flows in a direct injection spark ignition engine: Cyclic variation and effect of valve lift," *Sci. China Technol. Sci.*, vol. 57, no. 3, pp. 489–504, Mar. 2014.

[8] H. Chen, M. Xu, D. L. S. Hung, and H. Zhuang, "Cycle-to-cycle variation analysis of early flame propagation in engine cylinder using proper orthogonal decomposition," *Exp. Therm. Fluid Sci.*, vol. 58, pp. 48–55, Oct. 2014.

[9] P. G. Aleiferis, J. Serras-Pereira, and D. Richardson, "Characterisation of Flame Development with Ethanol, Butanol, Iso-octane, Gasoline and Methane in a Direct-Injection Spark-Ignition Engine," *Fuel*, vol. 109, pp. 256–278, Jul. 2013.

[10] J. Serras-Pereira, P. G. Aleiferis, and D. Richardson, "An experimental database on the effects of single- and split injection strategies on spray formation and spark discharge in an optical direct-injection spark-ignition engine fuelled with gasoline, iso -octane and alcohols," *Int. J. Engine Res.*, vol. 16, no. 7, pp. 851–896, Oct. 2015.

[11] A. Marchi, J. Nouri, Y. Yan, and C. Arcoumanis, "Spray stability of outwards opening pintle injectors for stratified direct injection spark ignition engine operation," *Int. J. Engine Res.*, vol. 11, no. 6, pp. 413–437, Dec. 2010.

[12] D. L. S. Hung, D. M. Chmiel, and L. E. Markle, "Application of an Imaging-based Diagnostic Technique to Quantify the Fuel Spray Variations in a Direct-Injection Spark-Ignition Engine," in *SAE Technical Paper Series*, 2003, vol. 1, no. 724.

[13] K. Bizon, G. Continillo, E. Mancaruso, S. S. Merola, and B. M. Vaglieco, "POD-based analysis of combustion images in optically accessible engines," *Combust. Flame*, vol. 157, no. 4, pp. 632–640, Apr. 2010.

[14] K. Liu and D. C. Haworth, "Development and Assessment of POD for Analysis of Turbulent Flow in Piston Engines," 2011.

[15] C. W. Rowley and S. T. M. Dawson, "Model Reduction for Flow Analysis and Control," *Annu. Rev. Fluid Mech.*, vol. 49, no. 1, pp. 387–417, Jan. 2017.

[16] A. Towne, O. T. Schmidt, and T. Colonius, "Spectral proper orthogonal decomposition and its relationship to dynamic mode decomposition and resolvent analysis," *J. Fluid Mech.*, vol. 847, pp. 821–867, 2018.

[17] A. Towne, O. T. Schmidt, and T. Colonius, "Spectral proper orthogonal decomposition and its relationship to dynamic mode decomposition and resolvent analysis," *J. Fluid Mech.*, vol. 847, pp. 821–867, Jul. 2018.

[18] H. Chen, D. L. Reuss, D. L. S. Hung, and V. Sick, "A practical guide for using proper orthogonal decomposition in engine research," *Int. J. Engine Res.*, vol. 14, no. 4, pp. 307–319, 2013.

[19] P. Holmes, J. Lumley, G. Berkooz, and C. Rowley, *Turbulence, Coherent Structures, Dynamical Systems and Symmetry*, Second Edi. Cambridge, UK: Cambridge University Press, 2012.

[20] H. Chen, D. L. Reuss, and V. Sick, "Analysis of misfires in a direct injection engine using proper orthogonal decomposition," *Exp. Fluids*, vol. 51, no. 4, pp. 1139–1151, 2011.

[21] H. Chen, M. Xu, D. L. S. Hung, and H. Zhuang, "Cycle-to-cycle variation analysis of early flame propagation in engine cylinder using proper orthogonal decomposition," *Exp. Therm. Fluid Sci.*, vol. 58, pp. 48–55, 2014.

[22] K. Bizon, G. Continillo, E. Mancaruso, S. S. Merola, and B. M. Vaglieco, "POD-based analysis of combustion images in optically accessible engines," *Combust. Flame*, vol. 157, no. 4, pp. 632–640, 2010.

[23] M. Fogleman, J. Lumley, D. Rempfer, and D. Haworth, "Application of the proper orthogonal decomposition to datasets of internal combustion engine flows," *J. Turbul.*, vol. 5, Jun. 2004.

[24] A. Chatterjee, "An Introduction to the Proper Orthogonal Decomposition Method.Pdf," *Curr. Sci.*, vol. 78, no. 7, 2000.

[25] L. Sirovich and R. Everson, "Management and Analysis of Large Scientific Datasets," *Int. J. Supercomput. Appl.*, vol. 6, no. 1, pp. 50–68, Apr. 1992.

[26] G. Kerschen and J. C. Golinval, "Physical interpretation of the proper orthogonal modes using the singular value decomposition," *J. Sound Vib.*, vol. 249, no. 5, pp. 849–865, 2003.

[27] P. J. Olver and C. Shakiban, *Applied Linear Algebra*, 2nd Editio., vol. 72, no. 462. Cham: Springer International Publishing, 2018.

[28] H. Chen, D. L. Reuss, and V. Sick, "On the use and interpretation of proper orthogonal decomposition of in-cylinder engine flows," *Meas. Sci. Technol.*, vol. 23, no. 8, p. 085302, Aug. 2012.

[29] L. Sirovich, "Turbulence and the dynamics of coherent structures. III. Dynamics and scaling," *Q. Appl. Math.*, vol. 45, no. 3, pp. 583–590, Oct. 1987.

[30] H. Chen, D. L. Reuss, and V. Sick, "On the use and interpretation of proper orthogonal decomposition of in-cylinder engine flows," *Meas. Sci. Technol.*, vol. 23, no. 8, 2012.

[31] H. Chen, D. L. S. Hung, M. Xu, H. Zhuang, and J. Yang, "Proper orthogonal decomposition analysis of fuel spray structure variation in a spark-ignition direct-injection optical engine," *Exp. Fluids*, vol. 55, no. 4, 2014.

[32] P. Sphicas *et al.*, “A Comparison of Experimental and Modeled Velocity in Gasoline Direct-Injection Sprays with Plume Interaction and Collapse,” *SAE Int. J. Fuels Lubr.*, vol. 10, no. 1, pp. 2017-01–0837, 2017.

[33] S. V. Gordeyev and F. O. Thomas, “A temporal proper decomposition (TPOD) for closed-loop flow control Topics in Flow Control. Guest editors J.P. Bonnet and L. Cattafesta,” *Exp. Fluids*, vol. 54, no. 3, pp. 1–16, 2013.

[34] B. O. T. Schmidt, P. J. Schmid, A. Towne, and S. K. Lele, “Statistical description of intermittency and rare events via conditional space-time POD : Example of acoustic bursts in turbulent jets,” *Cent. Turbul. Res. Annu. Br.*, pp. 151–159, 2018.

[35] O. T. Schmidt and P. J. Schmid, “Statistics of Stochastics: A conditional space-time POD formalism for intermittent and rare events with application to jet noise,” no. Pope, 2018.

Chapter 4

Study of Cold-Start Soot and Gas Emissions in a DISI Engine Using a Skip Firing Protocol

4.1 Introduction

As discussed in the introductory chapter, direct injection spark ignited (DISI) engines offer great advantages that can be exploited to increase the fuel efficiency of light-duty vehicles. Nonetheless, particulate matter (PM) emissions associated with this type of engine are higher when compared to other common gasoline engines, namely port-fuel injection (PFI) engines [1]–[3]. This higher tendency to form soot gets worse at the operating phase known as cold start, the first few minutes in which the engine and exhaust treatment equipment operate at a colder temperature with respect to their optimum set points. It is crucial to further understand the phenomena that drive in-cylinder soot formation in direct injection (DI) engines, especially during the cold start period, in order to mitigate emissions, meet ever more stringent regulations, and minimize their environmental and health impact.

From the perspective of public health, PM has been shown to have significant negative impacts on respiratory and cardiovascular health [4]–[6]. Airborne particulates are usually classified based on their size, as characterized by equivalent or aerodynamic diameter, and how far they can penetrate in the human body. The thoracic PM fraction, or PM_{10}, is defined as particles with a diameter smaller than 10 μm and can penetrate into the tracheobronchial tree. Fine particulates, also called $PM_{2.5}$, can reach small airways and the alveoli and have diameters smaller than 2.5 μm. Ultra-fine particulates (UFP) and nanoparticles have diameters smaller than 100 nm and 50 nm, respectively, and can go past the respiratory system into the bloodstream and reach other organs, including the brain. These particulates have a high area-to-mass ratio, which can increase their toxicity and can lead to multiple diseases [4], [5]. Internal combustion (IC) engines have been identified as one of the major sources of $PM_{2.5}$, UFP, and nanoparticles [1], [4]–[6].

PM emitted by IC engines consists of a heterogeneous mixture of particles with different composition, shape, and size in both liquid and solid phases [1], [7]. Commonly emitted engine-generated particulates include oil, fuel and water droplets, metal wear particles, and carbonaceous particulates known as soot; the latter commonly being the most prominent type of PM from engines [6]. Is for this reason, in the context of IC engines, soot and PM are generally used interchangeably. Historically speaking, soot has been a major concern primarily for diesel engines. But as gasoline direct injection becomes a mainstream technology and, simultaneously, emission standards become stricter, knowledge on soot formation and mitigation is crucial for spark ignited engines as well [8], [9].

Much research has focused on understanding the structure of soot and how it forms in combustion systems. Soot particles consist of primarily carbon atoms, with H/C ratio of around 0.2, which is comparable to coal [9]. At its core, a soot particle is based on carbon atoms arranged in hexagonal arrays, similar to graphite, which form crystallites that grow and agglomerate to form bigger particulates [10]. Soot forms in the environment of fuel-rich flames, and is controlled by local temperature, pressure, and equivalence ratio [11], [12]. These main parameters drive various simultaneously-occurring phenomena that lead to soot particulates and include fuel pyrolysis, nucleation, surface growth, coagulation, agglomeration, and oxidation. These processes are depicted in Figure 4.1 [1], [6], [9], [10], [13]. Soot particles form at high temperatures, at least around 1500 K [6]. At that point, the parent fuel has been thermally decomposed into stable and radical components by pyrolysis/thermal decomposition. One of the major products of hydrocarbon pyrolysis is acetylene, which has been identified as a key soot precursor, in addition to small polycyclic aromatic hydrocarbons (PAH), like benzene, that serve as building blocks for soot [9]–[11], [13]. Specifically, pre-condensed PAH, six-membered ring molecules, are stable at the high temperatures present in the flame. These embryonic aromatic species nucleate and undergo surface growth by means of dehydrogenation [6], [9]. The initial particles are a few nanometers in size, but experience rapid growth in an entropy driven reaction that has been explained as an hydrogen abstraction-acetylene (C_2H_2) addition mechanism, commonly referred to as HACA [9]–[11], [13]. The HACA mechanism involves a 2-step repetitive reaction, in which, first, a radical abstracts a hydrogen atom from a PAH molecule, leaving an active site open to which an acetylene molecule attaches [12], [13]. As mentioned before, acetylene is abundant in pyrolized hydrocarbons, so small aromatics can react with the gas, polymerize, and rapidly grow into large PAHs. At the same time, as the concentration of the incipient particulates increases, the particles collide and aggregate through coagulation and agglomeration. Coagulation occurs when two particles collide and their original structure is lost; this route leads to the formation of spherical units called spherulites [11], [12]. On the contrary, when particles aggregate, they maintain their structure after collision and form chain-like molecules with complex shapes and fractal characteristics. It is understood that agglomeration requires “mature” molecules and sufficient residence time [12]. The last important process relevant to soot particles is oxidation, through which particles can shrink or completely oxidized into gas products. The primary soot oxidizer is the OH radical and the reaction is highly sensitive to temperature and radical concentration [1], [12]. It is important to note that, although each process has a different rate, characteristic time, and sensitivity to local variables, they are generally happening in parallel and do not necessarily follow sequential development [11].

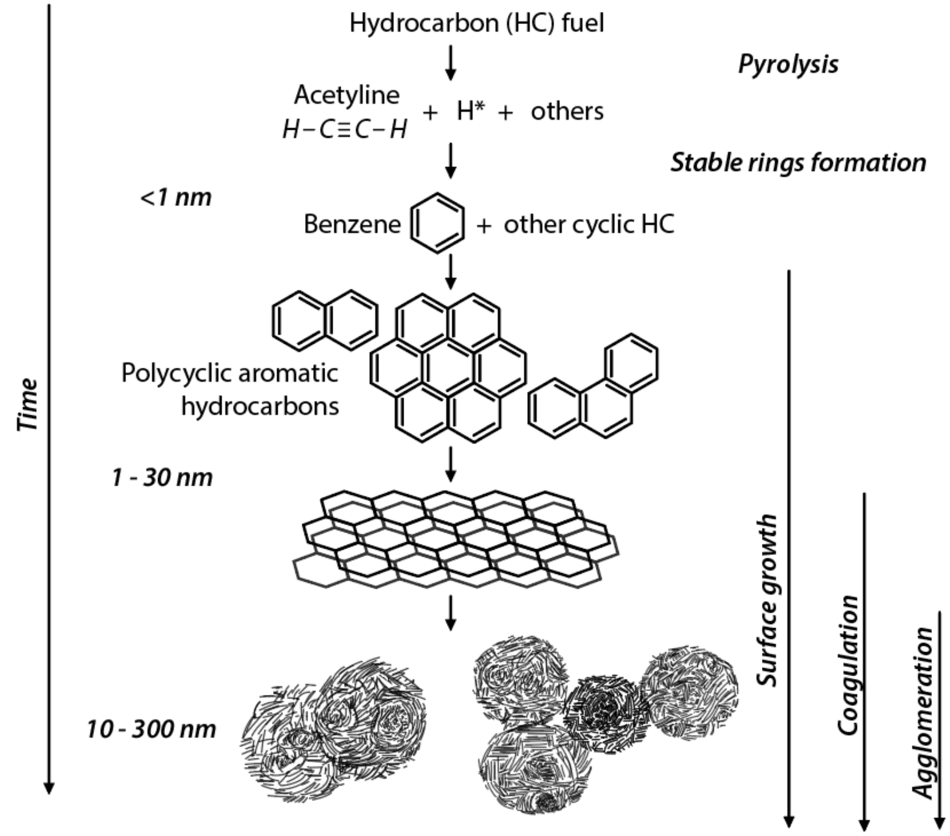

Figure 4.1. Phases and soot formation processes in combustion systems (based on [6]).

The characteristics of engine-out soot depend on the engine specifications, fuel properties, and operating conditions, and therefore, vary from system to system. Three common quantitative characteristics used to study PM in engines are particulate number (PN) –the number of particles generated by volume, the particle size distribution and the particulate mass [7], [14], [15]. The parameters can be presented relative to engine performance like engine power or on mass, volume or size bases. In-cylinder particulates generally present a lognormal size distribution. When two modes are present in the size distribution they are commonly referred to as the nucleation and accumulation modes [3], [6], [8], [15]–[17]. Although the thresholds are not well defined, particles in the range of 1 nm to a ~50 nm in diameter are referred as the nucleation mode, while the accumulation mode is identified as particles in the size range from ~50 nm to 1000 nm [6], [8].

The names denote a connection between the particle size distribution and the formation mechanisms previously described, that is, nucleation, agglomeration, and coagulation. The naming convention is based on the thought process that larger particles can only form through accumulation, which includes aggregation and coagulation. Although small particles usually form by nucleation, it is possible for a particle to grow by accumulation, followed by considerable oxidation and result in a particle which is in the nucleation size range. Therefore, the names of the distribution modes can be misleading. It should also be noted that a third range, called the coarse mode, represents particles in the 2.5 to 40 μm in size, but these larger particles are generally attributed to carbonaceous deposits which detach from the walls of the exhaust system and are not generally formed during the combustion process [6].

In the context of DISI engines, the literature indicates the phenomena that happen during and just after fuel injection –namely, fuel atomization, vaporization, spray impingement, and mixing– dominate the formation of soot [2], [15], [17]–[19]. The main engine parameters that control these engine processes are fuel injection pressure and timing, fueling strategy, and operating temperatures. Increasing the injection pressure promotes better fuel atomization and mixing, creating a more homogeneous charge that mitigates the formation of particulates [15], [17]. By optimizing the injection timing, turbulence can promote mixing while spray piston impingement and the formation of fuel films on surfaces can be avoided, driving down the occurrence of fuel rich zones and pool fires that create soot [2], [14], [15], [19]. The injection strategy can also help decrease PM emissions; for example, using multiple injections per cycle improves air entrainment and minimizes impingement, factors that mitigate particulate formation [20]–[23]. Finally, the operating temperatures –intake air, fuel, and engine temperatures– have significant effects on soot formation, as cold temperatures impede proper vaporization, lead to more fuel impingement and the formation of pool fires [15], [22], [24].

In connection to this last point emissions during the cold-start phase represent one of the major challenges DISI engines. As defined by the Federal Test Procedure #75 (FTP-75), cold start represents the initial 505 seconds after engine start of operation at a temperature of 20°C. During this early phase, DISI engines can produce up to 75% of the total PM and 80% of the total hydrocarbons emitted during the test [19], [25].

The problem with emissions during cold start is aggravated by the fact that the exhaust treatment equipment operates poorly at cold temperatures. Three-way catalyst (TWC) converters are the standard method of controlling emissions of the criteria air pollutants –hydrocarbons (HC), the oxides of nitrogen (NOx), and carbon monoxide– in spark-ignited engines, but their conversion efficiency is low when they operate at temperatures below the light-off set point. To achieve fast catalyst light-off, a big part of the start-up procedure involves generating a high enthalpy flux out of the engine. This is generally achieved by retarding the spark timing to have ignition occur after top dead center (TDC) of the compression stroke, so the exhaust gases flow out the cylinder and into the TWC at high temperatures [19], [26], [27]. However, delaying the spark introduces another problem, namely engine instability. At these retarded ignition timings, the combustion takes place in an environment where the temperature, pressure, and turbulence intensity are rapidly decreasing. Since these factors play a major role in flame formation, development and combustion stability, partial burns and misfires become a challenge that has to be addressed. Using a split injection can counteract the effects of delaying the spark discharge, by using the first injection to generate a homogeneous charge and the second injection to create a fuel rich mixture close to the spark plug so a strong flame kernel can be formed [18], [19], [27]. In summary, specific considerations during the cold-start phase must be balanced to achieve the desired engine stability, low engine-out emissions, and a short catalyst light-off time.

Previous experimental studies using optical engines have covered some of the issues related to soot formation in DISI engines and their operation at cold temperatures using reactive and non-reactive conditions. The presence of PM can be detected in the combustion chamber as a bright yellow/orange region due to the thermal radiation of the particles [2], [14], [18], [23], [27], [28]. Previous studies have shown that the in-cylinder incandescence of soot particles can be directly correlated with engine-out PM measurements; this validates the study of soot formation and behavior by means of direct high-speed imaging of in-cylinder combustion phenomena to understand soot emissions [2], [14], [23], [29]. Other relevant findings regarding optical studies are discussed further in Section 4.4.

4.2 Experimental Setup

The experiments presented in this chapter were performed in a reconfigurable optically-accessible DISI engine with a side-mounted 6-hole fuel injector, centrally-mounted spark plug, and dual-camshaft four-valve design located at the University of Michigan. The engine had a 0.51 L displacement volume, with an 89.0 mm bore, 81.4 mm in stroke, and a nominal compression ratio of 9.4:1. The valve timing used for this set of experiments were intake valve opening (IVO) at 5° bTDC, with duration of 253°, and exhaust valve closings at 30° bTDC, with a duration of 238°. The valve timing used for the study is also presented in Figure 4.2.

Before and during the experiments, an external pump ran coolant fluid through the engine head, metal liner, and engine block. A closed control system consisting of a proportional–integral–derivative (PID) controller, an electric heater, and a heat exchanger with flowing chilled water was used to maintain the coolant temperature at the desired set-point. Since the oil temperature was only passively controlled, special care was taken to monitor the oil gallery temperature and limit drift by more than 5°C with respect to the coolant temperature. The intake pressure was set in an open loop by adjusting a stepper motor position that controlled a throttle mounted on the intake manifold.

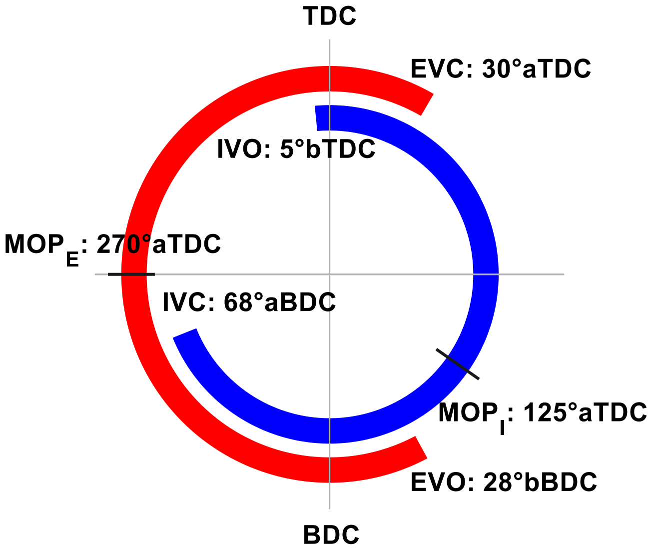

Figure 4.2. Intake and exhaust valve timings for skip-firing experiments.

Four different piston/liner configurations were used to interrogate the fuel injection, combustion, and emission characteristics throughout the study. 1) The metal configuration (i.e., metal piston with metal liner) was initially used to explore the injection pulse-width duration, injection timing space and their effects on equivalence ratio, engine performance, and emissions. 2) The optical piston and with partial optical liner (25 mm) configuration was used for imaging non-reactive sprays by Mie scattering. 3) Combustion imaging was acquired using an optical piston with metal liner. 4) Finally, combined spray and combustion imaging was performed using a partial optical liner and metal piston to explore the connections between the spray behavior, its interactions with the combustion chamber surfaces, soot behavior, and the effects of the production bowl design of the piston crown. Figure 4.3 presents a diagram of the single cylinder engine in the optical configuration used to image non-reactive sprays.

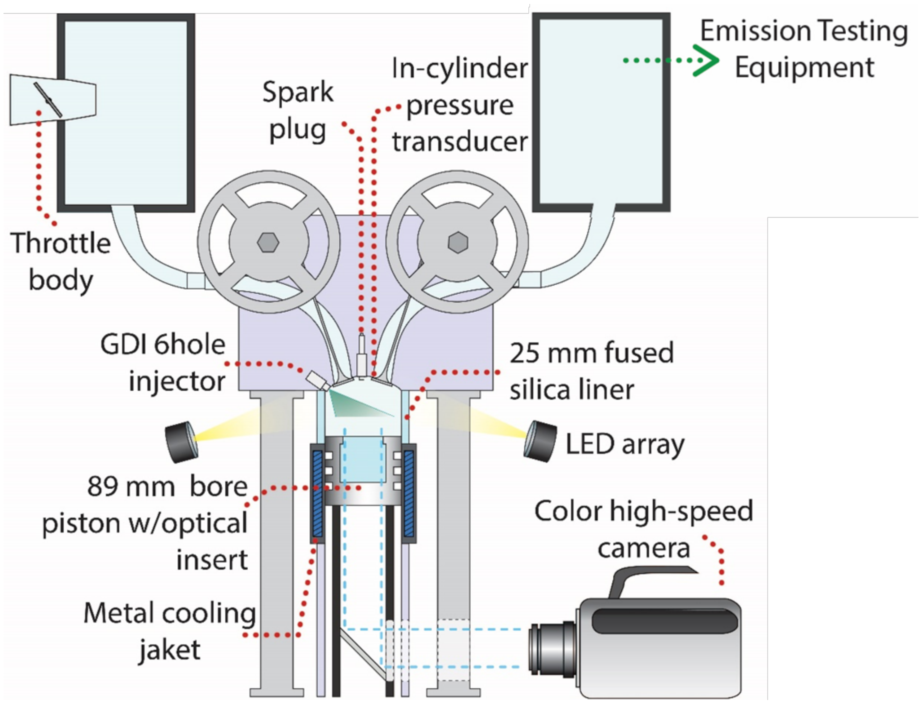

Figure 4.3. Single-cylinder engine in the fully optical configuration: optical piston with partial optical liner.

The engine was instrumented with multiple transducers in order to probe and measure various variables of interest. In-cylinder pressure measurements were acquired using a piezoelectric transducer and amplifier from Kistler (6052A and 5010B). Additionally, a Druck transducer (PMP-2060) was used to measure the manifold absolute pressure (MAP), and the dynamic pressure at the intake runner was recorded using a Kistler transducer and amplifier (4045A2 and 4618). Air-to-fuel (A/F) ratio was measured using a broadband lambda sensor from Bosch (LSU 4.9) located at the exhaust runner and a lambda module from ETAS (LA4). Thermocouples located at the intake and exhaust manifolds and runners, the oil gallery, and coolant inlet and outlet were used to obtain temperature data.

The engine speed, throttle, injection and spark timing were controlled using an engine module from Electro Mechanical Associates (EMA). A Bosch P06 engine control unit connected to the EMA module activated the injector at command. During this study, the engine was operated using a skip firing protocol; Section 4.3 discusses this in further detail. In order to control and synchronize the engine's fueling pulses, the data acquisition system, the LED arrays, and the camera, a microprocessor (Arduino Due) was programmed as an external input/output real-time digital controller. The microprocessor was used to perform the skip-firing procedure by enabling the injector during firing cycles and disabling it during skipping cycles. Additionally, the microcontroller sent a trigger signal to the camera and powered the LED arrays only during the injection events.

Engine-out emissions were measured using three emission testing systems. An exhaust gas emission analyzer (Horiba MEXA-584L) was used to measure emissions for CO, CO_2, unburned hydrocarbons, and nitrogen oxides (NOx). To characterize the soot emissions, an opacity meter from AVL (415 Smoke Meter) was used to obtain a filter smoke number (FSN) based on the filter paper method and a blackening index. Finally, a scanning mobility particle sizer (SMPS) from TSI, consisting of a classifier (DMA 3080) and a particle counter (CPC 3010), was used to obtain particulate distributions and particulate numbers for the experiments. An impact filter with D50 of 50.8 μm was used to condition the exhaust samples, in addition to a rotating thermo-diluter disk (379020A) with a dilution factor of 50:1 and a conditioning temperature of 120°C. The scanning time for the SMPS was 30 seconds and the scanning range was 8.35 to 264 nm. Two SMPS scans, with a dwell time of 10 seconds, were performed at each condition and later averaged.

Analog and digital signals were recorded using a data acquisition system from National Instruments programmed with a LabVIEW routine that enabled instantaneous data visualization and monitoring. Digital signals included the fuel pulse signal, spark coil signal, TDC marker, and the trigger signal sent to the high-speed camera. The emission readings from the Horiba analyzer, the equivalence ratio reading, the intake air flow rate, and the signals for the previously described pressures were acquired using an analog input cards (NI-9201 and NI-9206); the spark, injection, and TDC signals were recorded with a digital carl (NI-9401). Temperature readings were recorded using a thermocouple input card (NI-9213). The data acquisition cards were mounted on two NI cDAQ-9174 chassis connected to a computer through a USB port. Data were acquired at a sampling rate of 60 kHz and logged into a text file for further processing and analysis in MATLAB.

In regard to the imaging equipment, a color high-speed CMOS camera from Vision Research (Phantom V711-8G-MAG-C) with a RGGB Bayer array was used for all the imaging studies. As mentioned before, both spray and combustion events were visualized through the partial optical liner and through the optical piston using a mirror tilted at 45°, as shown in Figure 4.3. The camera was operated at a frame rate of 22,500 frames per second (fps), which translated into three frames per crank angle degree (CAD), with an exposure time of 44.4 μs. The video sequences have a resolution of 512×512 pixels, and a bit depth of 16 bits. A Canon TV Zoom J6x11-11 lens with an f-stop at 5.6 was used and focused at the tip of the spark plug. To obtain Mie scattering data of the fuel sprays, two white light-emitting diode (LED) arrays from Visual Instrumentation (#900420) were used to illuminate the chamber during injection.

4.3 Experimental Approach

The study was based on cycle-resolved in-cylinder high-speed imaging of fuel spray, combustion and soot incandescence phenomena using a skip-firing protocol to represent cold-start operating conditions. Experiments using the metal configuration were also performed to understand the effects of injection strategy on emission and engine performance variables. The engine was operated at a single speed of 1250 revolutions per minute (RPM) and a MAP of 75kPa, with coolant and air temperatures of 20°C. A dwell time of ~45 minutes between tests, during which the engine block was actively cooled, was followed. All experiments used reference grade gasoline; Appendix 3 lists the fuel properties obtained from the vendor. To replicate industry-relevant ignition timing for cold-start conditions, a delayed spark timing of 17° aTDC was used throughout the tests. This represents a delay of about 60 CAD from the spark-timing conventionally used at warm conditions.

At the conditions studied, the engine presented complete instability when using stoichiometric fueling. Therefore, the engine was operated using fuel rich conditions to improve combustion stability. An injection strategy using one injection event was tested, but the strategy led to misfires in more than 98% of cycles, so a double injection strategy was then used throughout the experiments. The second injection stabilized the engine by generating a fuel rich environment close to the spark plug, which supported the propagation of the flame even at the delayed spark timing.

Table 4.1. Summary of experimental conditions used for the skip firing study.

Variable	Values
Engine Speed	1250 RPM
Coolant and Air Temperature	20 ± 2°C
Oil Temperature	20 ± 5°C
Spark Timing	17° aTDC
Start of Injection 1 (SOI1)	180°, 240°, 300° bTDC
Start of Injection 2 (SOI2)	25°, 45°, 65°, 85, 125 bTDC
Split Ratio	70/30
Injection Pressure	100 bar
Equivalence Ratio	1.25
Manifold Absolute Pressure	75 kPa
Skip/Firing Ratio	10/1

To investigate the effects of charge strategy as a function of start of injection (SOI), three SOI for the first event and five SOI for the second injection where varied, giving a total of 15

SOI1/SOI2 combinations. The different combination of SOIs have a direct impact on charge homogeneity and stratification; the implications are discussed in the results section. Table 4.1 presents a summary of the experimental conditions and the parametric space investigated during the study.

Cold-start experiments in an optical engine pose several challenges. Liquid fuel films generated due to poor vaporization and spray impingement and soot deposits on surfaces lead to a rapid decrease in optical visibility. Secondly, using industry-relevant ignition timings (e.g., 10° aTDC and later) for cold-start protocol produce extremely high exhaust temperatures that can damage the instrumentation and emission testing equipment. Temperatures on the exhaust manifold can surpass 700 °C in a few seconds. Finally, the cold-start process is intrinsically transient and temperatures drift considerably after testing. These phenomena limit the repetition rate to short experimental runs and long cooling times between tests, making statistically significant data sets time consuming.

To address these problems, the engine control and data acquiring systems were adapted to operate under a skip-firing mode, in which one firing cycle was followed by 10 non-firing cycles. The skip-firing protocol improves visibility since non-firing cycles help to evacuate the combustion chamber. Additionally, exhaust temperatures are quenched during the non-firing cycles and the transient temperature rise is slowed. Ideally, each cycle becomes independent from the others, so the firing cycles can be directly compared, and their variability analyzed on a firing cycle-to-firing cycle basis. However using a skip firing protocol reduces the effects of certain phenomena present in a continuously firing engine, namely, the effect of residuals and the interdependence between cycles.

During the optical experiments of the combustion events, natural luminosity from the flame and soot incandescence were obtained. The emission spectra of combustion radicals (e.g., OH, CN, and CH) peak mainly on the 250-400 nm range [14], [27]. On the other hand, thermal radiation from soot is broadband in nature and is apparent from 200 nm to a few microns [14]. With this in mind, the red, green, and blue (RGB) channels from the camera were analyzed separately. The blue channel is spectrally tuned for light in the 390 to 525 nm range, while the red channel is sensitive in the 575 to 655 nm region. By separating the red and blue channels, the chemiluminescence, which is concentrated in the blue channel data and be differentiated from the thermal radiation from soot which is present in the signal from both channels. Based on this, a quantitative metric developed by Fatouraie et al. [29], the spatially integrated natural luminosity (SINL), was used to characterize the sooting behavior and compare the injection timings. The SINL was computed by spatially integrating the pixel values, $\iint I_{pixel} dxdy$, throughout each frame in the video sequences. Heat release analysis, based on the method proposed by Brunt et al. [30], was used to compare the combustion phasing of all experiments.

4.4 Experimental Results and Discussion

4.4.1 Metal Configuration Experiments

The SOI for a split injection strategy was systematically varied to understand the effect of charge homogeneity and stratification on engine performance and emissions. Since earlier injections translate to longer time for vaporization and mixing, the first event sets a baseline for the bulk charge stoichiometry, while the second injection can generate local heterogeneities of fuel distribution and mixing. In the SOI1 space, the 300° bTDC injection timing represented the most homogenous case, while the 180° bTDC corresponded to a more stratified charge. Similarly, 125° and 25° bTDC represented the homogeneous and stratified extremes in the SOI2 space.

At each condition, 60 firing cycles were recorded from which averages and standard deviations were computed. Figure 4.4 presents the computed averages for the net indicated mean effective pressure (IMEP) and its coefficient of variation (COV) as a function of SOI2; error bars represent the standard deviation for the recorded cycles. The results show engine performance is dominated by the timing of the second injection event, as the data overlapped within the experimental variability for most of the SOI2 timings studied. The IMEP peaked around 45° to 65° bTDC, and decreased if SOI2 was too early (too homogeneous) or too late (too stratified), indicating there is an optimal level of charge stratification. The same effect was observed for COV. The engine became unstable as SOI2 was advanced or retarded from 65° in the direction of more homogeneous (advanced) or more stratified (retarded) charge. The extremes were not equally unstable, since on the more homogeneous side (85° and earlier), the engine became very unstable, which underlined the importance of having a fuel rich zone close to the spark plug. It should be noted that for light-duty vehicles, a COV of IMEP lower than 10% is desired for cold start conditions. The significantly higher instability results observed in this study were a result of the retarded spark timing.

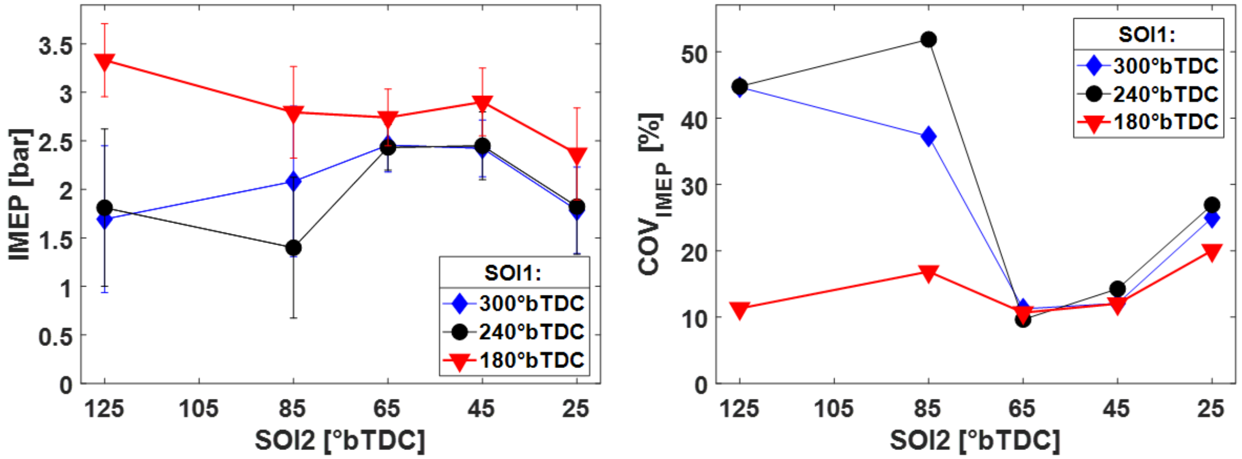

Figure 4.4. Net IMEP and COV of IMEP as a function of SOI2 for three SOI1.

The trends presented in Figure 3.4 were observed for all conditions, except the SOI1:180°, SOI2:125° combination. This point showed good performance and low variability between cycles. The fuel injection timings correspond to the most stratified first injection and the most homogeneous second injection. The combination of these extremes yielded in an appropriate environment in which the flame propagated consistently every cycle, translating to better combustion phasing and shorter burn durations.

Figure 4.5 shows the burning profiles (i.e. mass fraction of fuel burned as a function of time as derived from in-cylinder pressure data) for two conditions with the same SOI2 of 125° bTDC, and different SOI1. The panel on the left corresponds to the case of SOI1 at 180° bTDC. The dark solid line represents the average for all cycles, the red area represents the standard deviation, and the pink area represents the fastest and slowest cycles. The plot shows that for the case in question, the spread in burning profiles was smaller, closer to TDC, and faster for the more retarded SOI1 timing. The figure panels include the computed CA50 and CA10-90 values for each set of operating conditions. Here, CA50 is defined as the crank angle degree with 50% of the total heat release, as derived from the pressure data [30]. Similarly, the CA10-90 refers to period from where the 10% to 90% the heat release happens, in crank angle degrees. Note that for the 180°/125° combination, the CA50 was closer to TDC and the combustion duration, as shown by the CA10-90, was shorter.

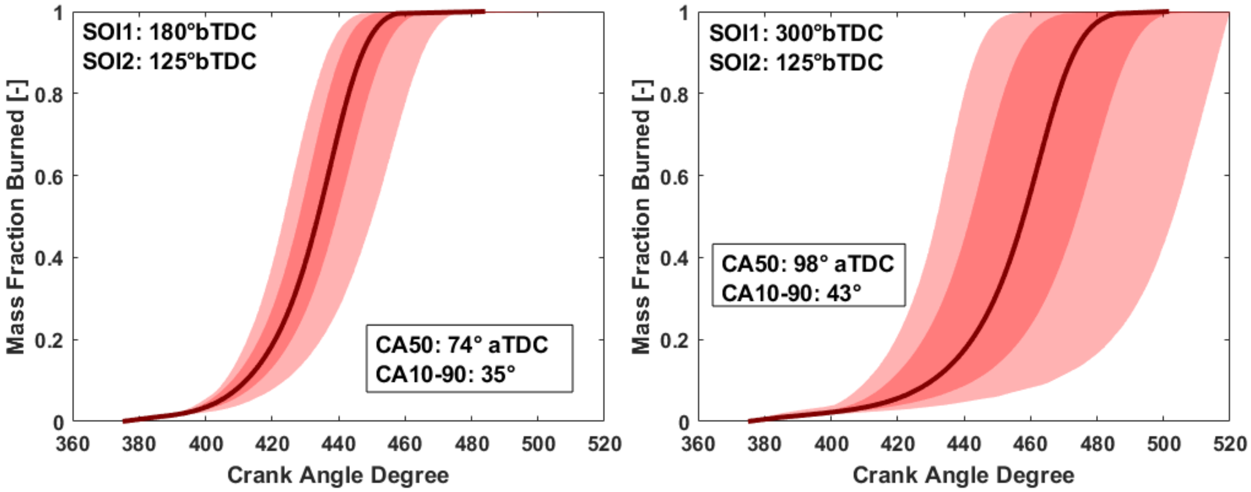

Figure 4.5. Mass fraction burned profiles for two SOI1 timings with the same SOI2 timing.

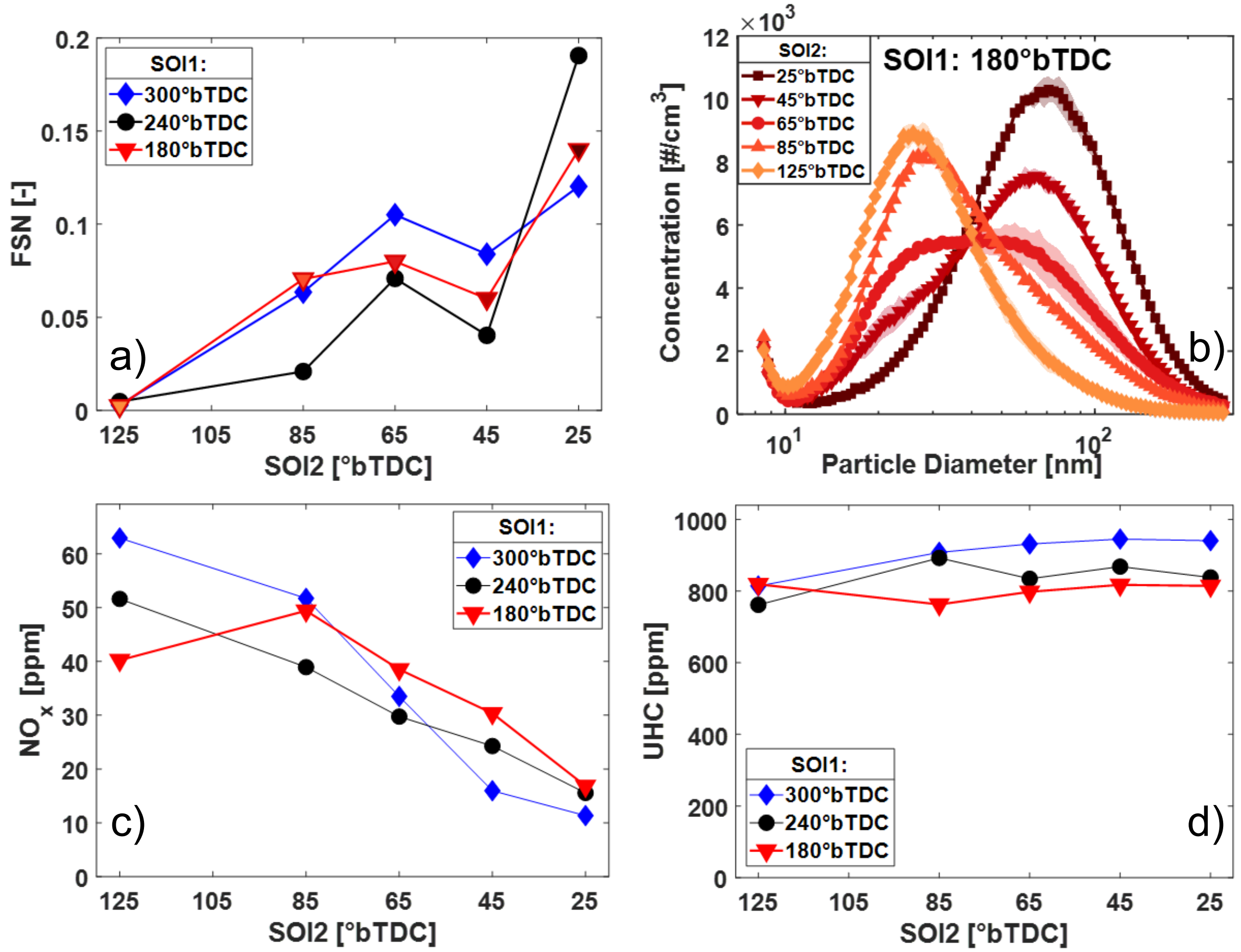

Figure 4.6. Engine-out emissions as a function of SOI2 for different SOI1 for the metal engine configuration experiments.

The engine-out emissions were similarly more sensitive to the second injection event. Figure 4.6 presents a summary of some of the emissions tested. The data show there was a strong dependence of FSN on SOI2, which tended to rapidly increase as SOI2 was retarded. The sudden decease at 45° bTDC can be explained by the interaction of the fuel jet with the bowl design of the piston crown. This behavior has been observed in other wall guided engines [31]. One could speculate that dependence on SOI2 is explained by the fact that a delayed injection would increase the spray impingement on the cylinder, driving soot formation and increasing the FSN. Nonetheless, the fact that 300° and 180° bTDC had such similar trends, even though there was significantly higher impingement for the earlier injection case, indicates that for the conditions tested, the primary source of soot was not fuel films. Imaging data presented in Section 4.4.3 show the increase in sooting for later injection timings (e.g, 45° and 25° bTDC) is dominated by particulates formed from fuel-rich pockets in the bulk of the charge, and not from fuel films.

Panel b) in Figure 4.6 shows the particle size distribution obtained from the SMPS measurements for the different SOI2 timing. A single SOI1 of 180° is shown here, but the other injection timings had similar behavior. The plot shows the FSN and particle number distribution are correlated, as one would expect since FSN measurements are mass-biased. Additionally, there is a clear distribution shift as a function of SOI2. For the case with higher charge stratification, SOI2 = 25° bTDC, the particle number distribution peaks at around 80 nm. As the injection timing is advanced, the distribution shifts to smaller mean diameter, peaking at close to 20 nm for the more homogeneous condition. The change in average particle size seems to indicate that stratified conditions at late injection, lead to particle agglomeration, while more homogeneous charge conditions tend to produce distributions that peak around the nucleation mode.

A shift in particle distribution as a function of injection timing has been previously reported in the literature. Barone et al. reported that for early injection timing, average particle diameter was around 25 nm, while at later injection timings the distribution was dominated by particles in the 10 to 15 nm size range [32]. However, the study by Barone et al. [16] was performed in a fully warmed engine at high-load conditions, which could explain the differences in particle size distribution and trend in size shift. Ketterer and Cheng [26] characterized PM emissions in a DISI engine at similar temperatures to the present study, and they found a strong connection between SOI and particle distribution similar to the one observed in the present study. For a single injection, they found the particle size distribution peaked close to 180 nm for early injection timings, specifically SOI of 360° and 340° bTDC. They also found a shift towards smaller geometric means (~10 nm) as the injection was retarded to 220°, but the distribution returned to peaks closer to 200 nm as the injection was delayed further to 20° bTDC. The authors attributed the change in distribution to the effects of fuel films generated during spray impingement. However, imaging in the present study will elucidate more regarding the nature of the particle formation, showing that the change is distribution is not only a function of spray impingement, but also strongly dependent on fuel stratification of the bulk charge.

Continuing with panel c), Figure 4.6 shows that the NOx emissions tended to increase for the most homogeneous cases, as the injection timing was advanced. A tradeoff between NOx and FSN was clear and consistent with behavior previously reported for DISI engines [29]. NOx in DISI engines is primarily generated though the thermal pathway [14] and is dominated by the local temperature and local air-to-fuel (A/F) ratio; so as the charge becomes more stratified, two regions –one locally lean, and a second one locally rich– would be formed. NOx increases for high-temperature stoichiometric conditions. Finally, the unburned hydrocarbons (UHC) emissions are presented in panel d) of Figure 3.6. The first observation is that UHC were higher as SOI1 was advance indicating this was a result of fuel impingement. A similar, but not as strong, trend was observed for SOI2. The behavior shows the film generated during the second injection is not as important as of the one formed during the first injection event with respect to the UHC emissions. Combining the performance and emissions results, the optimized injection timings for the engine used in the study would be an SOI1 between 180° and 240° bTDC with a second injection event around 45° bTDC. Such timing would maximize IMEP, yield acceptable engine stability, and emit low levels of soot, NOx, and UHC.

4.4.2 Non-reactive Spray Imaging Experiments

Non-reactive spray imaging experiments for all SOI conditions were performed to understand the behavior of the spray as a function of injection timing before moving into reactive flow studies. Figure 4.7 shows still frames for two different views for the injection timing at 300°bTDC a few CAD after SOI. The liner view in panel b) clearly shows valve wetting from the center spray plumes as the arrows in the figure indicate. Valve interference was detected for the three SOI1, and the 240° bTDC timing was the case with the largest source of interference since that timing coincided with the maximum opening position of the intake valves. The valve wetting was exacerbated by the cold fuel and air temperatures used during the testing. It is known that lower temperatures increase the penetration distance and prevents spray collapse [29], [33], which increases the chances of valve impingement as observed here. Additionally, fuel impingement on the piston was also detected for injection timings with end of injection (EOI) within 60° of TDC, namely SOI2 of 65°, 45° and 25° bTDC.

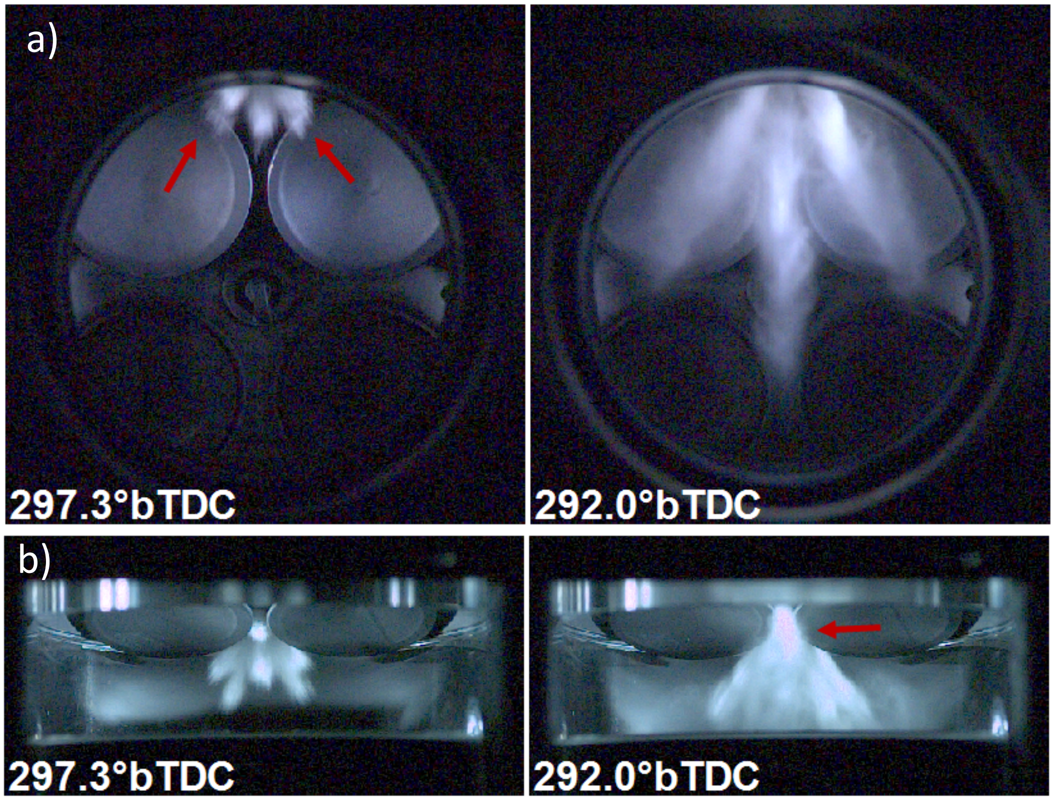

Figure 4.7. Non-reactive spray imaging for SOI1 at 300° bTDC. Panel a) shows a piston view of the spray, and panel b) shows a liner view. Valve wetting from the central plume is observed in both panels and is indicated by the arrows in the figures.

The non-reactive spray imaging studies also showed a second interesting observation relevant to cold-start operation. During the expansion stroke, fuel re-condensed in a cloud with a pattern similar to the spray footprint driven by the quick decrease in temperature and turbulence. Since retarding the ignition timing to the expansion stroke is a common strategy during the warm-up phase, fuel re-condensation becomes important. The fuel contrails can be seen in Figure 4.8, and although temperatures would rapidly increase after ignition in a firing cycle, the still frame shows the environment in which the flame would propagate, which includes fuel rich zones formed due to this condensation.

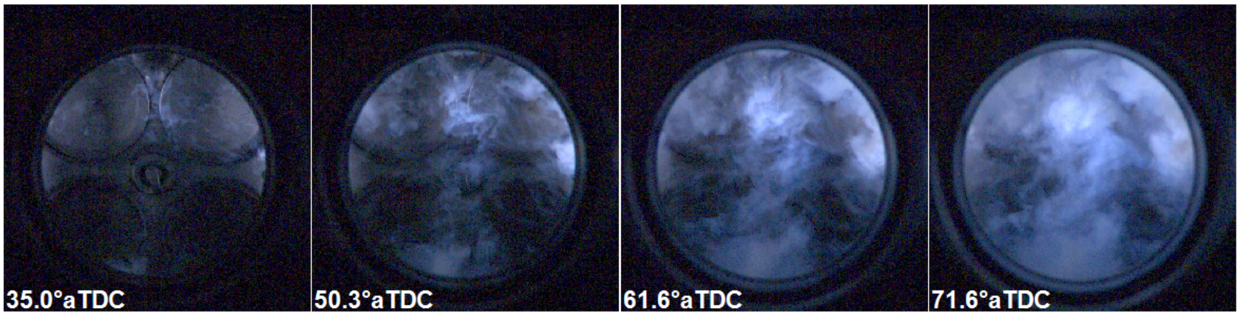

Figure 4.8. Fuel re-condensation during the expansion stroke in a similar pattern as the initial spray path.

4.4.3 Spray and Combustion Imaging Experiments

The effects of SOI timing on combustion characteristics and sooting behavior were studied using two engine configurations. During the first set of experiments, a full metal liner was used, and the combustion process was imaged trough an optical insert in the piston crown. A second set of data was obtained using a metal piston with a crown design similar to a production engine. The imaging of the spray and combustion processes was obtained through the 2.5 cm liner as previously shown in Figure 4.3. Using this configuration, the experiments were repeated two times at each condition, one with the LED arrays on during the combustion phase, and a second set with the LED illumination off. In the latter set, the camera only captured the natural luminosity from combustion, which was used to compute a spatially integrated natural luminosity (SINL) as a metric to evaluate the sooting characteristics based on the imaging data.

The imaging data showed a similar trend as the FSN and the particle distribution results, in the sense that the combustion characteristics were clearly controlled by the second injection and no sensitivity to the first injection event was observed. Still frames for the two extremes, the most stratified charge (25° bTDC) and the most homogeneous charge (125° bTDC), for a single SOI1 of 180° bTDC are presented in Figure 4.9. Results from the other two SOI1 showed similar behaviors as those described here.

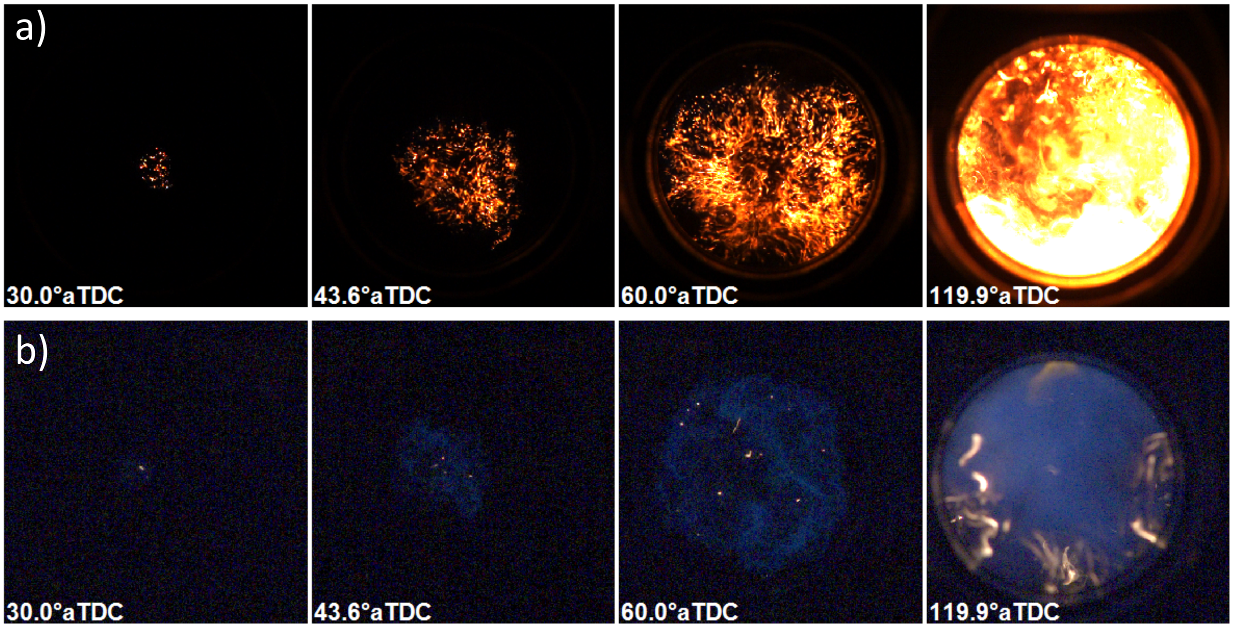

Figure 4.9. Imaging data for SOI1 at 180° bTDC and two SOI2 timings of a) 25° and b) 125°, which correspond to the most stratified and most homogeneous conditions, respectively. The gain for the images at the SOI2 of 125°bTDC was increased for presentation purposes

For the case of the late SOI2, i.e. the most stratified charge, strong soot formation was detected early in the flame propagation process and throughout the cycle. The soot formed at this condition was mainly localized in filament-like structures that formed as the flame propagated through the combustion chamber and reached fuel rich pockets in the charge. Similar flame structures have been reported when poor vaporization leads to the presence of fuel droplets that ignite as the growing flame reaches them, forming soot as fuel rich diffusion flames [23], [27].

Efthymiou et al. [27] reported filament structures similar to the ones observed in the present study in a DISI engine operating at similar temperatures, ambient intake pressure, but using a single injection strategy and an earlier ignition timing than what was used here . The authors stated the presence of droplets leads to rich local zones where particulates nucleate and rapidly grow, leaving observable incandescence trails as the droplets travel [18], [27]. The same mechanism appears to be the source of soot in the present study: fuel droplets present in the combustion chamber burn in localized diffusion flames as the premixed flame expands through the cylinder. The presence of the filament-like soot structures appears to be a specific sooting characteristic at cold-start conditions and is due to the fact that cold temperatures can produce a significant number of non-vaporized fuel droplets.

On the contrary, for the case of early SOI2, combustion starts with a non-sooting premixed flame kernel which is defined by blue spectral emission, and the flame grows in what appears to be a “soot-less” manner until it reaches the surfaces of the combustion chamber, where some soot pockets form. Mostly, blue emission, from the chemiluminescent reactions involving radicals like CH, is present during the combustion event. In this case, the particulates were produced from fuel films formed by spray impingement, primarily at the liner and spark plug. Having more time to mix and evaporate at these fuel injection conditions, the presence of liquid fuel drops does not appear to be prevalent, yielding cleaner combustion and lower PM emissions.

The trends were similar when using the metal piston and imaging through the optical liner. Figure 4.10 shows the imaging data for SOI1 at 180°bTDC and the same SOI2 timings previously discussed. The right panel shows the most stratified condition, although only the first injection could be imaged. Significant liner impingement on the opposite side of the injector was observed. Additionally, liquid droplets were present close to the spark plug at 30° aTDC. A condensation cloud, like the one observed during the non-reactive spray studies, starts forming during the expansion stroke, and it grows from the boundary surfaces towards the center of the combustion chamber. Filament-like structures form as the flame propagates, and once the flame reaches the re-condensation zones, soot incandescence intensifies. Late in the cycle, incandescence is stronger on the side opposite from the injector, i.e. the region where obvious spray impingement occured. For the homogeneous case, Figure 4.10 panel b), both SOI1 and SOI2 injection events could be imaged, and showed significant liner impingement. However, the combustion process was very different from the more stratified condition. Flame propagation was characterized by the "cleaner" blue spectral emission and soot was localized at the chamber surfaces, mainly the spark plug and liner. Furthermore, fuel re-condensation appeared to be less significant; therefor soot formation was not intensified by this effect.

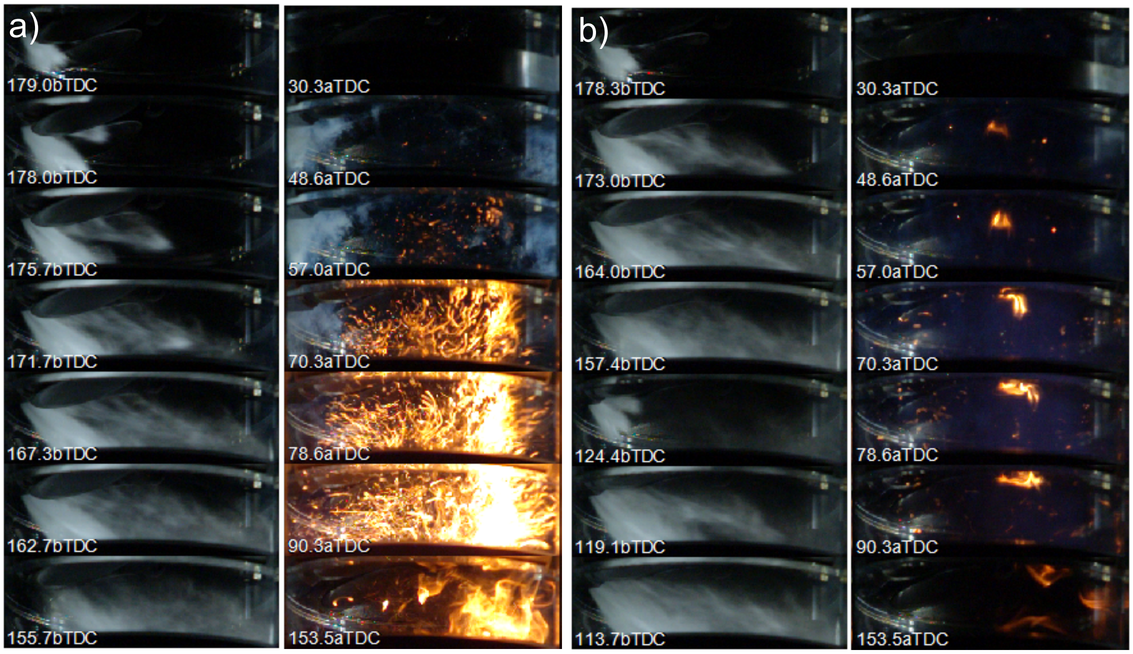

Figure 4.10. Injection and combustion events for SOI1 = 180° bTDC and a) SOI2 = 25° bTDC and b) SOI2 = 125° bTDC.

The combustion events without the LED lights for four SOI2 and a single SOI1 timing of 180° bTDC are presented in Figure 4.11. Results from other SOI1 timing yielded similar trends. The imaging data showed a clear transition as SOI2 was advanced from combustion development dominated by intense soot filaments, to a blue flame propagation where soot was formed at the boundaries of the combustion chamber.

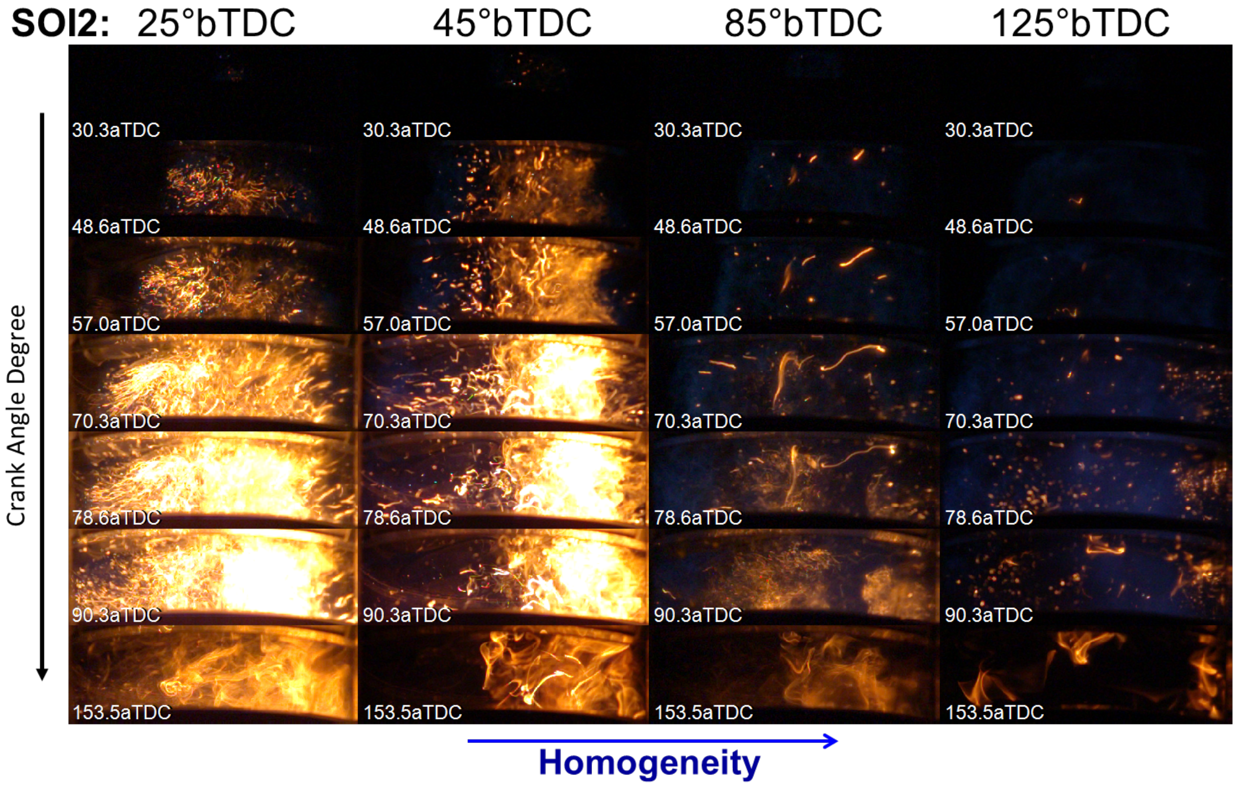

Figure 4.11. Comparison of combustion events for SOI1 = 180° bTDC and four different SOI2 timings. Similar trends were observed for SOI1 at 240° and 300° bTDC.

The combustion imaging results help clarify the trends observed on the particle size distribution previously discussed. Conditions which yielded larger average particle size in the aggregation mode, (e.g. conditions with stratified charge), correlate with soot formed in filament structures (which are associated with combustion of fuel droplets). Conversely, the homogeneous case, where the particle size distribution peaked in the nucleation mode, had most of the soot formed at the surfaces of the combustion chamber. The optical study, in connection with the SMPS measurements, indicates that the physical location and source of the soot has a strong effect on the size distribution of the particles formed. Moreover, at the conditions tested for late injection timing, the primary source of soot formation is fuel stratification and rich pockets, and not fuel impingement. This explains why FSN and particle distribution were insensitive SOI1, even when early injection would lead to higher impingement; SOI2 has a higher impact on charge stratification, and therefore, dominates the sooting behavior.

As mentioned before, the red channel in the camera captures the thermal radiation from the soot, while filtering out most of the chemiluminescence, so this signal was used to quantitatively characterize the soot behavior. For each frame, the data were spatially integrated to compute the SINL as a function of CAD and the results are shown in Figure 4.12. The solid lines represent the ensemble average for 30 cycles, and the shaded area is the standard deviation.

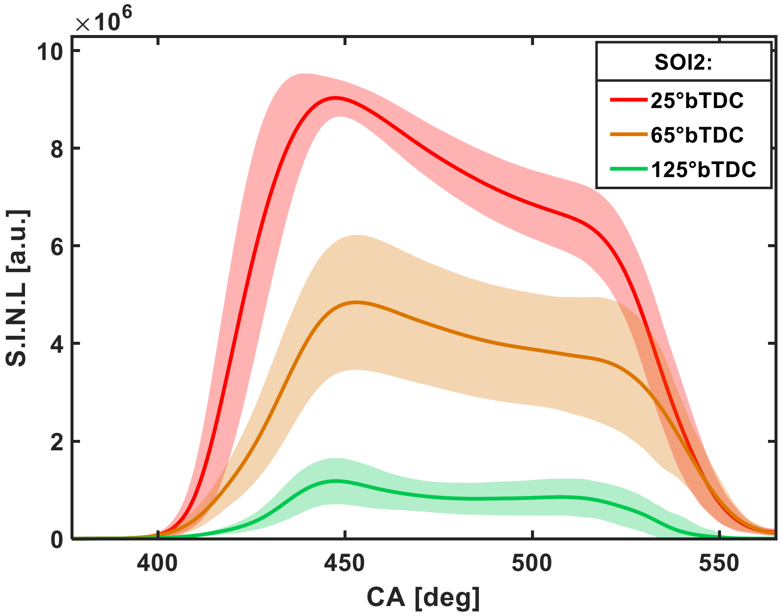

Figure 4.12. Spatially integrated luminosity for SOI1 at 180° and three different SOI2. The missing SOI2, 45° and 85°, lay between the curves shown here.

As the second injection is advanced, SINL decreased significantly indicating that soot formation is mitigated by optimizing the stratification. Although the three luminosity profiles peaked at approximately the same time, the rate of soot formation was higher for the stratified charge (25° bTDC) and the particulates started forming earlier in the cycle, which translated to longer residence time and higher PM concentration. These two facts would increase the chances of particles colliding, coagulating, and agglomerating, which explains why the agglomeration mode dominates at the particle distribution for that case. The longer residence time would also allow more time for oxidation; however, the results indicate soot growth mechanisms dominate over soot oxidation. As with the FSN and the SMPS measurements, the SINL was insensitive to SOI1, as seen in Figure 4.13, and a strong correlation with SOI2 is clear.

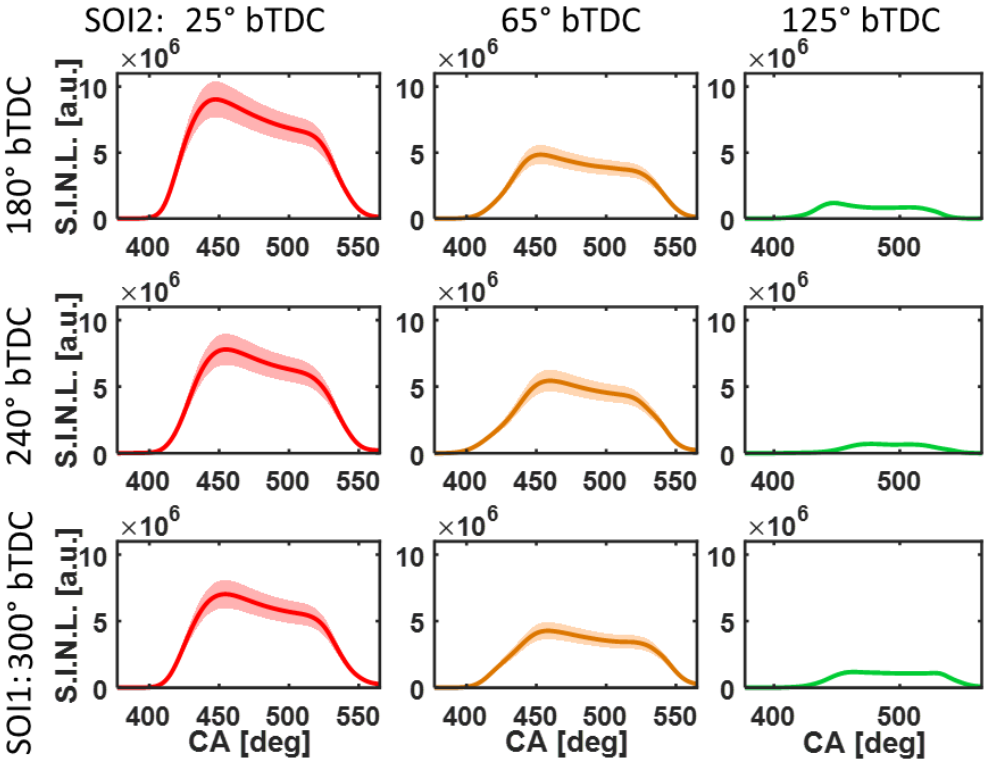

Figure 4.13. Spatially integrated natural luminosity (SINL) for three different SOI1 (rows) and three SOI2 (columns).

4.5 Conclusions

- Under the conditions tested (i.e., split injection with retarded spark at cold temperatures), the engine performance and emissions was primarily controlled by the second injection. Split fueling generated a superposition of effects, early injection led to mixing which created a baseline fuel air charge which did not significantly affect the behavior of the engine. The later injection controlled the fuel stratification which dominates performance and the engine-out emissions.

- The imaging data from the soot incandescence showed that the PM sources for cold start are similar to the sources found for hot engines (e.g. wetted surfaces and fuel rich regions). However, at cold-start conditions with retarded spark, the combination of cold boundaries and late ignition timing led to fuel re-condensation, forming fuel rich pockets that intensified soot formation.
- The particle size distribution is correlated with the dominating soot formation source. Specifically, conditions with soot originating from fuel impingement on surfaces presented a smaller particle distributions (8-20 nm), while conditions with PM forming primarily at fuel rich pockets due to charge stratification had larger particle distributions (20-200 nm).

4.6 Abbreviations

A/F	Air-fuel [ratio]
aTDC	After top dead center
bTDC	Before top dead center
CA50	Crank angle corresponding to 50% of total heat release
CAD	Crank angle degree
CO	Carbon monoxide
COV	Coefficient of variation
DI	Direct injection
DISI	Direct injection spark ignition
EVC	Exhaust valve closing
EVO	Exhaust valve opening
FSN	Filter smoke number
FTP	Federal test procedure
HACA	Hydrogen abstraction-C2H2 (acetylene) addition
HC	Hydrocarbon
IC	Internal combustion
IMEP	Indicated mean effective pressure
IVO	Intake valve opening

LED	Light-emitting diode
MAP	Manifold absolute pressure
NOx	Nitrogen oxides
PAH	Polycyclic aromatic hydrocarbon
PFI	Port-fuel injection
PID	Proportional integral derivative
PM	Particulate matter
RPM	Revolutions per minute
SINL	Spatially integrated natural luminosity
SMPS	Scanning mobility particle sizer
SOI	Start of injection
TDC	Top dead center
TWC	Three-way catalyst
UFP	Ultra-fine particles
UHC	Unburned hydrocarbons

References

[1] D. Kittelson and M. Kraft, "Particle Formation and Models in Internal Combustion Engines," *Cambridge Cent. Comput. Chem. Eng.*, no. 142, pp. 1–39, 2014.

[2] M. Fatouraie, M. Wooldridge, and S. Wooldridge, "In-Cylinder Particulate Matter and Spray Imaging of Ethanol/Gasoline Blends in a Direct Injection Spark Ignition Engine," *SAE Int. J. Fuels Lubr.*, vol. 6, no. 1, pp. 2013-01–0259, Apr. 2013.

[3] M. Braisher, R. Stone, and P. Price, "Particle Number Emissions from a Range of European Vehicles," no. Ci, 2010.

[4] R. D. Brook *et al.*, "Air Pollution and Cardiovascular Disease," *Circulation*, vol. 109, no. 21, pp. 2655–2671, Jun. 2004.

[5] J. Stolcpartova *et al.*, "Internal Combustion Engines as the Main Source of Ultrafine Particles in Residential Neighborhoods: Field Measurements in the Czech Republic," *Atmosphere (Basel).*, vol. 6, no. 11, pp. 1714–1735, Nov. 2015.

[6] J. Merkisz and J. Pielecha, *Nanoparticle Emissions from Combustion Engines*. Springer.

[7] S. K. Friedlander and W. H. Marlow, "Smoke, Dust and Haze: Fundamentals of Aerosol Behavior," *Phys. Today*, vol. 30, no. 9, pp. 58–59, Sep. 1977.

[8] D. B. Kittelson, "Engines and Nanoparticles: A Review," *J. Aerosol Sci.*, vol. 29, no. 5–6, pp. 575–588, Jun. 1998.

[9] O. I. Smith, "Fundamentals of Soot Formation in Flames with Application to Diesel Engine Particulate Emissions," *Prog. Energy Combust. Sci.*, vol. 7, no. 4, pp. 275–291, Jan. 1981.

[10] A. Violi, A. F. Sarofim, and T. N. Truong, "Mechanistic Pathways to Explain H/C Ratio of Soot Precursors," *Combust. Sci. Technol.*, vol. 174, no. 11–12, pp. 205–222, Nov. 2002.

[11] H. Wang, “Formation of Nascent Soot and Other Condensed-phase Materials in Flames,” *Proc. Combust. Inst.*, vol. 33, no. 1, pp. 41–67, 2011.

[12] M. Frenklach, “Reaction Mechanism of Soot Formation in Flames,” *Phys. Chem. Chem. Phys.*, vol. 4, no. 11, pp. 2028–2037, May 2002.

[13] M. Frenklach and H. Wang, “Detailed modeling of soot particle nucleation and growth,” *Symp. Combust.*, vol. 23, no. 1, pp. 1559–1566, Jan. 1991.

[14] S. S. Merola, A. Irimescu, L. Marchitto, C. Tornatore, and G. Valentino, “Effect of injection timing on combustion and soot formation in a direct injection spark ignition engine fueled with butanol,” *Int. J. Engine Res.*, vol. 18, no. 5–6, pp. 490–504, 2017.

[15] X. He, M. A. Ratcliff, and B. T. Zigler, “Effects of Gasoline Direct Injection Engine Operating Parameters on Particle Number Emissions,” *Energy & Fuels*, vol. 26, no. 4, pp. 2014–2027, Apr. 2012.

[16] T. L. Barone, J. M. E. Storey, A. D. Youngquist, and J. P. Szybist, “An Analysis of Direct-Injection Spark-Ignition (DISI) Soot Morphology,” *Atmos. Environ.*, vol. 49, pp. 268–274, Mar. 2012.

[17] W. Piock, G. Hoffmann, A. Berndorfer, P. Salemi, and B. Fusshoeller, “Strategies Towards Meeting Future Particulate Matter Emission Requirements in Homogeneous Gasoline Direct Injection Engines,” *SAE Int. J. Engines*, vol. 4, no. 1, pp. 2011-01–1212, Apr. 2011.

[18] G. K. Hargrave, P. Efthymiou, J. E. T. Rimmer, M. H. Davy, D. Richardson, and C. P. Garner, “Insights into Cold-Start DISI Combustion in an Optical Engine Operating at −7°C,” *SAE Int. J. Engines*, vol. 6, no. 2, pp. 1059–1074, 2013.

[19] Z. Xu, J. Yi, S. Wooldridge, D. Reiche, E. W. Curtis, and G. Papaioannou, “Modeling the Cold Start of the Ford 3.5L V6 EcoBoost Engine,” *SAE Int. J. Engines*, vol. 2, no. 1, pp. 2009-01–1493, 2009.

[20] P. Yin, Y. Gao, M. Xu, D. Hung, and J. Su, “Particle Number Emissions Reduction Using Multiple Injection Strategies in a Boosted Spark-Ignition Direct-Injection (SIDI) Gasoline Engine,” *SAE Int. J. Engines*, vol. 8, no. 1, pp. 20–29, 2014.

[21] T. Li, K. Nishida, Y. Zhang, M. Yamakawa, and H. Hiroyasu, “An Insight Into Effect of Split Injection on Mixture Formation and Combustion of DI Gasoline Engines,” 2004, no. 724.

[22] K. G. Duleep, “The Impact of Gasoline Direct Injection System Design on PM Emissions,” 2019, pp. 1–16.

[23] S. S. Merola, A. Irimescu, C. Tornatore, L. Marchitto, and G. Valentino, “Split Injection in a DISI Engine Fuelled with Butanol and Gasoline Analyzed through Integrated Methodologies,” *SAE Int. J. Engines*, vol. 8, no. 2, pp. 2015-01–0748, Apr. 2015.

[24] W. Fedor, J. Kazour, J. Haller, K. Dauer, and D. Kabasin, “GDi Cold Start Emission Reduction with Heated Fuel,” in *SAE 2016 World Congress and Exhibition*, 2016.

[25] D. C. Quiros *et al.*, “Measuring Particulate Emissions of Light Duty Passenger Vehicles Using Integrated Particle Size Distribution (IPSD),” *Environ. Sci. Technol.*, vol. 49, no. 9, pp. 5618–5627, May 2015.

[26] J. E. Ketterer and W. K. Cheng, “On the Nature of Particulate Emissions from DISI Engines at Cold-Fast-Idle,” *SAE Int. J. Engines*, vol. 7, no. 2, pp. 2014-01–1368, Apr. 2014.

[27] P. Efthymiou, C. P. Garner, G. K. Hargrave, and D. Richardson, “An Optical Analysis of a DISI Engine Cold Start-Up Strategy,” in *SAE Technical Paper Series*, 2015, vol. 1.

[28] E. Stevens and R. Steeper, “Piston Wetting in an Optical DISI Engine: Fuel Films, Pool Fires, and Soot Generation,” 2001, vol. 2001, no. 724.

[29] M. Fatouraie, “The Effects of Ethanol/Gasoline Blends on Advanced Combustion Strategies in Internal Combustion Engines,” pp. 1–147, 2014.

[30] M. F. J. Brunt, H. Rai, and A. L. Emtage, “The Calculation of Heat Release Energy from Engine Cylinder Pressure Data,” in *SAE Technical Paper Series*, 1998, vol. 1, no. 724.

[31] J. E. Ketterer and W. K. Cheng, “On the Nature of Particulate Emissions from DISI Engines at Cold-Fast-Idle,” *SAE Int. J. Engines*, vol. 7, no. 2, pp. 2014-01–1368, 2014.

[32] T. L. Barone, J. M. E. Storey, A. D. Youngquist, and J. P. Szybist, “An analysis of direct-injection spark-ignition (DISI) soot morphology,” *Atmos. Environ.*, vol. 49, pp. 268–274, 2012.

[33] J. Serras-Pereira, P. G. Aleiferis, and D. Richardson, “An experimental database on the effects of single- and split injection strategies on spray formation and spark discharge in an optical direct-injection spark-ignition engine fuelled with gasoline, iso -octane and alcohols,” *Int. J. Engine Res.*, vol. 16, no. 7, pp. 851–896, Oct. 2015.

Chapter 5

Design and Demonstration of a Novel In-situ Sensor for Spray Impingement and Fuel Composition

5.1 Introduction

In the context of modern combustion research, the internal combustion (IC) engine is no longer a black box. Several means for optical access and probing tools into the combustion chamber have led to advances in understanding, predicting, and designing for specific fuel spray characteristics, charge motion, spark plasma development, combustion, and emission mitigation. The field has benefited from the development of complex techniques like particle image velocimetry, phase Doppler anemometry, high-frequency momentum and pressure transducers, and high-speed imaging-based methods. It is undeniable that advanced diagnostic tools and probing instrumentation have greatly expanded our understanding of in-cylinder phenomena and helped at improving engine performance and emissions. Nonetheless, certain engine processes remain poorly understood, and engine design would benefit from the development of novel diagnostics to elucidate into the nature of these phenomena. Specifically, characterization tools are lacking for fuel impingement, spray-wall interaction, and film evaporation; these complex processes are recognized as some of the key challenges in engine research [1].

Fuel films are formed during typical operation of reciprocating internal combustion engines and have critical effects on engine performance and emissions. Films are formed on liner, piston, and valve surfaces as a direct result of fuel impingement during injection, fuel rebound, and fuel condensation. A wide range of experimental data has been reported on fuel films, with film thickness ranging from 0.1 to 100 μm, and surface areas of 10s to 100s of mm^2, depending on conditions and operating parameters [2]–[4]. These thin films have been identified as sources of fine particulate matter (PM) [5]–[7] and unburned hydrocarbon (UHC) emissions [8], and as the cause of coking and varnishing of gasoline direct fuel injectors [9], [10]. Therefore, surface wetting is a critical design concern for modern spark ignition and compression ignition engines.

Liquids droplets interact with surfaces in a plethora of natural and artificial processes, like raindrops hitting surfaces, spray painting and coating, urea injection, and plant fertilization, just to name a few. Spray-wall interactions involve complex multiphase phenomena that are governed by both the thermophysical properties of the fluids (i.e., the liquid and the ambient gas) and the surface characteristics of the wall [4], [11], [12].

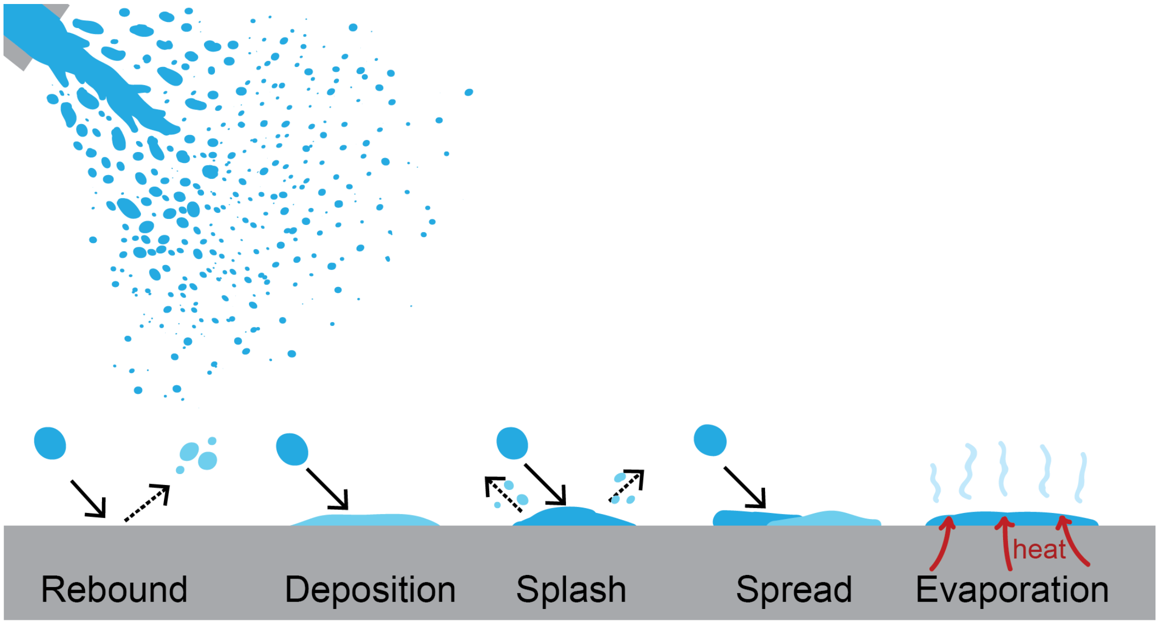

Figure 5.1. Simplified schematic for some of the regimes included in multiple conceptual models for spray-wall ineractions.

A better understanding of spray-wall interaction has been developed through single- and multiple-drop experiments [13], [14]. Multiple conceptual models have been proposed to explain and capture the conclusions of the experimental work [4], [11], [15]. These models frequently consist of different regimes for the dynamic formation and evolution of the spray-wall interactions, including hydrodynamic and heat transfer regimes. Common mechanisms in the models include droplet rebound, deposition, spread, splash, evaporation, and Leidenfrost effect. Figure 5.1 shows simplified schematics for a few of the common regimes experimentally observed. The dominating mechanisms controlling liquid film formation depends on the liquid's density, surface tension, and viscosity of the liquid used in the spray; drop size, shape and velocity; ambient gas pressure and temperature; and surface temperature, roughness, and wetness. Lee et al. [14] provide an excellent and comprehensive review of the numerous conceptual and theoretical models developed on spray-wall interactions.

Within the engine research community, pioneering and innovative methods have been developed and used to study fuel impingement in and outside optical engines for diesel, gasoline, and biofuel sprays. The methods include laser-induced fluorescence [2], [3], [16], [17], refractive index matching [8], [18], infrared thermography [19], high-speed imaging [20], and gravimetric techniques [21]. Based on these techniques, crucial factors controlling film formation and behavior have been identified, including injection pressure [19], engine surface temperatures [2], [18], [22], injection duration [16], [17], and in-cylinder flow [2], [23]. Although these are powerful techniques, they have different drawbacks when measuring films in conditions relevant to reciprocating engines. Additionally, these methods are difficult to scale to a variety of engine platforms, as they require expensive instrumentation, or the techniques cannot operate in-situ to measure in-cylinder films. What is missing is a less costly, simple, robust, and versatile method to measure the fundamental characteristics of the spray-wall interaction and fuel films that form in engines.

The objective of the study on developing a new technology to measure films was to design and fabricate a capacitive sensor to characterize fuel impingement and films generated by non-reactive sprays and to demonstrate the efficacy of the sensor in a single-cylinder optical engine.

The sensor was designed to help develop fundamental understanding of spray impingement and film characteristics, which are critical for reducing empiricism and developing comprehensive physics-based theory for spray-wall interactions.

Some challenges of developing a capacitive sensor are due to the intrinsic properties of fossil fuels. Specifically, the relative permittivity of petroleum-derived fuels is typically close to the relative permittivity of air; diesel fuel and gasoline have a relative permittivity around two, compared with air, which has a dielectric constant of one. Hence, a capacitive sensor would display low sensitivity to thin films formed by these fuels. To address this fact, the present study uses ethanol and ethanol-gasoline blends as fuel surrogates. Ethanol has a dielectric constant of 24.3 [24], which would increase the sensitivity of the proposed sensor. This approach is also relevant since ethanol is a fuel with significant use in the transportation sector. Ethanol is commonly used as an automotive fuel at blend rates from 10% to 85% by volume in the U.S. and, in countries like Brazil, ethanol is used neat (100% hydrous ethanol) as pump fuel [25], [26].

Ethanol is commercially available in the U.S. in three main nominal ethanol-gasoline blend concentration: E10, E15, and E85, where the numeric values signify the ethanol volume percentage (i.e., E15 represents a 15% ethanol, 85% gasoline blend per volume) [27]. However, the fuel found at gas pumps and branded as E85 actually has a variable ethanol content that spans from 51% to 83% depending on the local geographical and seasonal characteristics [26], [28]. Ethanol content has direct impacts on the behavior of the fuel spray [6], [29], ignition of the mixture [27], [30], engine emissions [9], [31], and overall performance of the engine [32], [33].

5.2 Capacitive Sensor Design and Function

The development of the sensor was guided by design objectives that were considered central to making a useful and versatile tool. The design goals included in-situ operation, non-contact data transmission, high-spatial sensitivity, high-temporal response, and low-cost fabrication. In-cylinder phenomena are usually hard to replicate, so in-situ measurements of fuel impingement are required to better represent the relevant phenomena occurring inside an engine. The sensor had to be small and lightweight to enable instrumenting a piston and to allow data to be retrieved without wires integrated with the moving components of the engine. From the literature review, the films were expected to be a few microns in thickness, so having high sensitivity in that range of film thickness was essential. The temporal response was also crucial since an engine cycle usually spans a few dozen milliseconds, and injection durations are considerably shorter than that, ranging from hundreds of microseconds to a few milliseconds. Finally, the sensor should be accessible from a financial standpoint, so the cost of the fabrication was kept low.

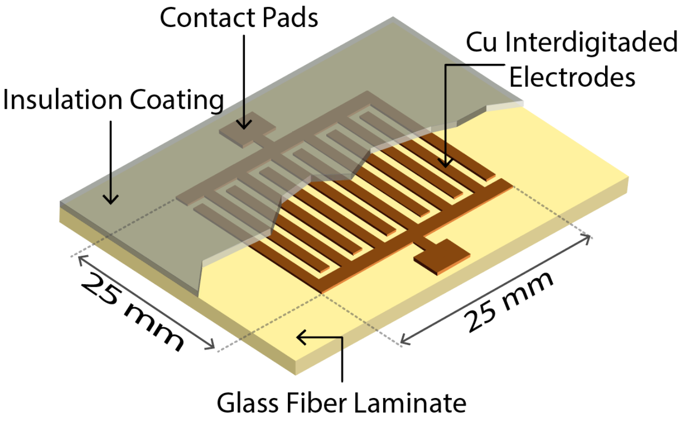

Figure 5.2. Schematic of the interdigitated electrode sensor. The electrode structure proportions are not to scale.

The sensor developed in this work is based on a capacitive sensing technique. The device consists of two comb electrodes made out of copper that are interdigitated to form the coplanar capacitor, with a sensing area of 25×25 mm. To prevent charge leakage and circuit shorts, the electrodes are covered with a passivation coating. The electrodes rest on a glass fiber laminate. The geometric parameters for the structures were varied in a computational study discussed in the following section (Section 5.3). Figure 5.2 shows a schematic (not to scale) of the sensor design.

The capacitance of the system is a function of the spatial characteristics and the permittivity of the medium that is in contact with the surface of the electrodes. If the relative permittivity of a fuel is higher than that of air, the capacitance of the system will increase as a liquid film forms on the surface due to the higher intensity of polarization. The capacitance would tend to increase as the film becomes thicker.

5.3 Computational Simulations and Results

2D finite element simulations (COMSOL Multiphysics) of a simplified coplanar capacitor were used to evaluate the effectiveness of the proposed design and understand the effect of the geometric parameters on the interdigitated electrode (IDE) capacitor. Figure 5.3a presents a sample geometry of the 2D model. The electrodes are made out of copper with a thickness of 35 μm. Parametric studies were performed varying electrode width and the spacing; the effects of the number of electrode pairs and the thickness of the insulation coating were also considered. The base geometry used a single electrode pair, electrode gaps and width of 100 μm. During the studies, a single parameter was varied while the others were kept at the base values. Designs with electrode "fingers" widths ranging from 25 to 200 μm and spacing gaps of 25 to 150 μm were considered and evaluated. For the computational component of the work, the passivation coating was a conformal layer of alumina.

Two main output variables were of interest in the simulations: the capacitance of the electrodes as a function of the film thickness and geometric parameters, and the electric polarization field medium in contact with the IDE. The polarization field describes the spatial response of a material when exposed to an electric field between two electrodes, since it indicates the strength of the induced electric dipole moment in the substance [34]. The molecules of a polar substance, like ethanol, orient themselves along the direction of the electric field and oppose the applied voltage [34]. This effectively increases the charge concentration at the electrodes, which in turn increases the capacitance of the system.

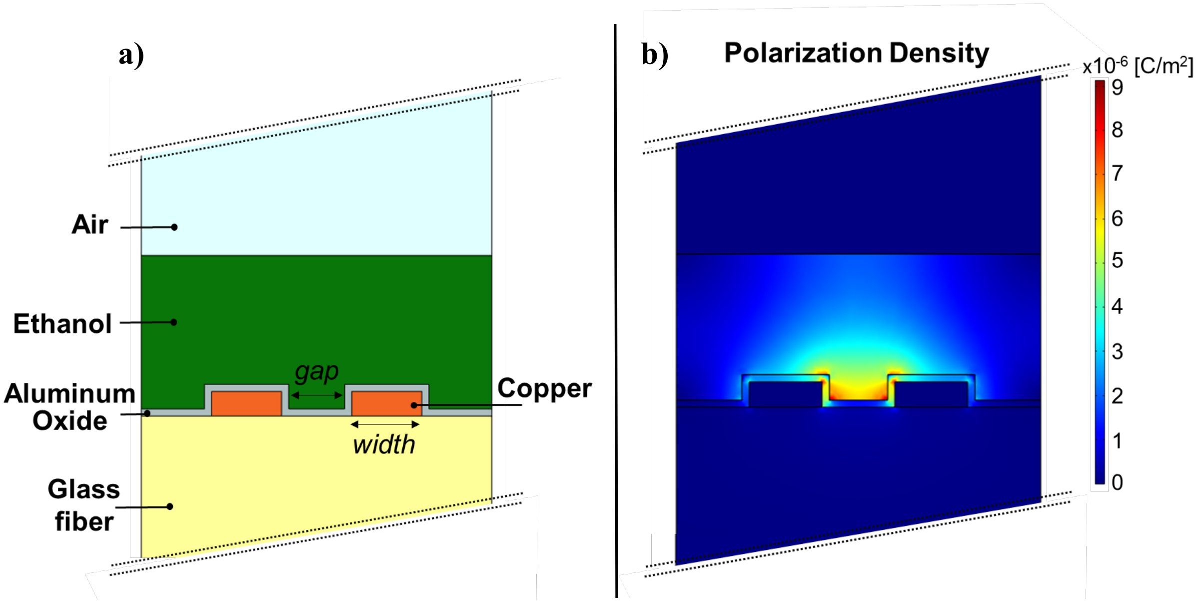

Figure 5.3. a) Simplified coplanar capacitor model programmed used in finite element model simulations (COMSOL): b) Results for the polarization density field of the sensor and liquid ethanol film. The domains for the air and glass fiber are cropped from the images for presentation purposes.

Figure 5.3b shows the predicted polarization density for the reference sensor design in the presence of a 100% ethanol film of 200 µm thickness with an applied voltage of 3V. The results show ethanol is considerably more polarized than air in the presence of the electric field. A second important observation is that the polarization field is concentrated within a semi-ellipse that goes from the midpoint of one of the electrodes to the halfway point of the second electrode, and the polarization field penetrates into the liquid to about half of the width of the electrodes. Based on these results, an expectation is that the sensor would start losing sensitivity to films that extend past the half-width of the electrode. Although, the proposed design is not a completely flat capacitor –since the thickness of the electrodes is not negligible– this finding is consistent with analytical solutions found in the literature for purely flat coplanar capacitors [35].

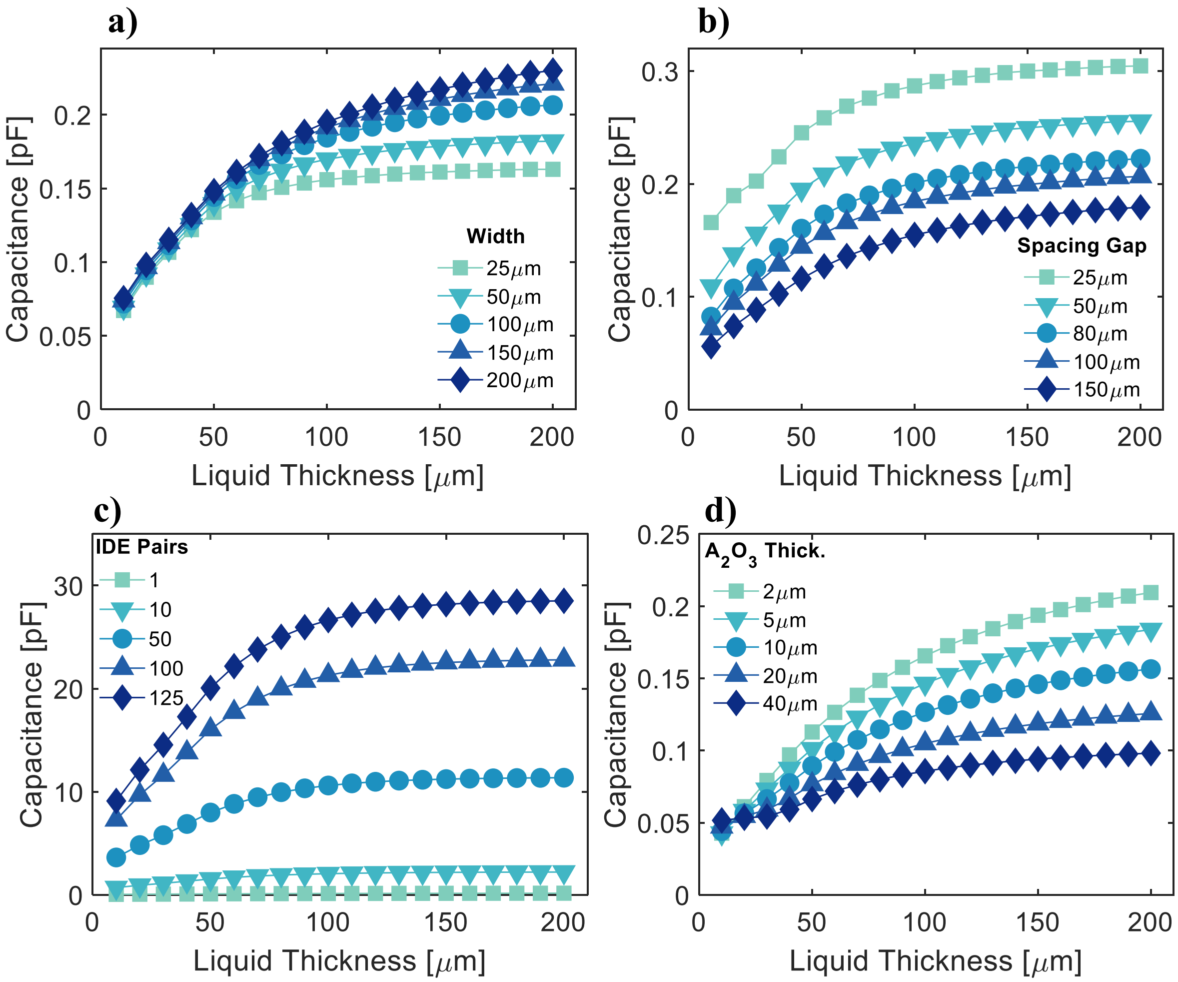

Figure 5.4. Simulation results for the capacitance response using 100% ethanol films for varying a) electrode width, b) spacing gap, number of IDE pairs, and insulating Al2O3 thickness. All simulations were conducted using a 3V potential applied to the electrode terminals.

Figure 5.4 presents the results for the capacitance of the device obtained from the parametric studies. Panel a) shows the capacitance of the device as a function of 100% ethanol film thickness for different electrode widths. All electrode widths had similar behaviors for films thinner than 50 µm. However, the capacitance of the IDE starts saturating when the film reaches a thickness comparable with the electrode width; beyond that point, the sensor sensitivity tends to decrease. The trend is explained by the results shown in Figure 5.3b. From a design perfective, one can prevent reaching this limit by selecting an electrode width at least twice as big as the maximum expected fuel film thickness. Figure 5.4b depicts the effect of the electrode spacing: as the gap decreases, the sensor becomes more sensitive. It would be desirable to maximize the response of the device to films thinner than 100 µm, so this gap should be as smaller as possible. Nonetheless, on the physical device, the spacing will be limited by the resolution and tolerance of the fabrication process. A trade-off between sensitivity, manufacturability, and fabrication cost must be considered to achieve the best overall results.

Panel c) in Figure 5.4 presents the effect of the number IDE pairs. The plot indicates that the sensor sensitivity drastically increases as electrode pairs are added. In fact, the capacitance system scales almost proportionally to the number of electrodes. Lastly, Figure 5.4d displays the effect of the coating thickness on the response of the capacitor and show that the capacitance increases for thinner coatings. Therefore, a thin coating would offer a better response of the sensor, although proper electrical insulation is desired as well.

Based on these results, and taking into account fabrication limitations, a few IDE platforms were fabricated with the following geometric parameters: 150 µm in electrode width, spacing gap of 50, 80 and 100 µm, and with as many electrode pairs as they could be fit 25 mm depending on the spacing gap (i.e., 100, 108, or 125 pairs, respectively).

5.4 Experimental Set-up

5.4.1 Electrode Fabrication

To demonstrate and test the physical performance and functionality of the device, interdigitated electrodes were fabricated using a similar procedure as the one used on printed circuit boards (PCB) for homemade analog circuits. However, as the simulation results showed, the electrode structures must be in the micron size regime to achieve the desired sensitivity. Amateur circuitry does not require that level of resolution, so little literature is available with that specific purpose. Therefore, a custom lithography recipe was developed by trial and error until the aspect ratio and resolution on the design were satisfactorily obtained. The fabrication recipe was optimized by varying the exposure time, the distance between the light source and the sample, the developing time, and the etching time. These processes are discussed in further detail below and shown in Figure 5.5. It should be noted that it was desired to fabricate an inexpensive device, so all the fabrication process was performed outside a cleanroom.

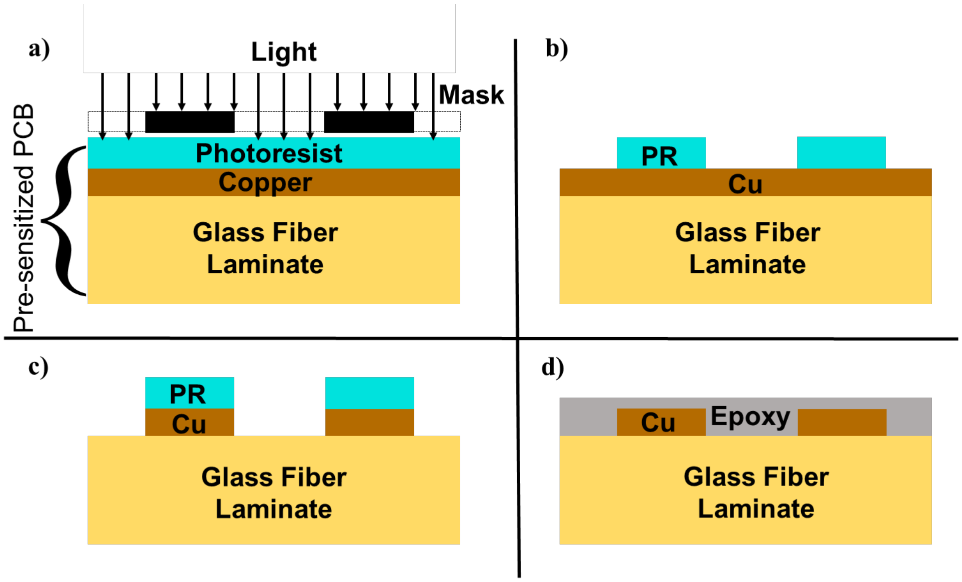

Figure 5.5. Diagrams of the steps used to fabricate the IDE capacitor sensor: a) contact photolithography, b) photoresistant developing, c) chemical etching, and d) passivation coating

A positive pre-sensitized copper-clad board (GC Electronics, 21-334-VP) was used as a starting point for the fabrication. The board consists of a single copper layer (35 μm in thickness) sandwiched between a photoresist and a fiberglass-epoxy laminate, commonly called FR-4. A side-view schematic of the board can be found in Figure 5.5a. Contact photolithography using a photomask printed at 5,000 dpi (CAD/Art Services) was performed to transfer the electrode design into the photoresist. The board was exposed for 17 minutes to a 23W fluorescent light (1600 lumens, 6,500 K) at 30 cm from the light source, while a glass pressed the mask against the photoresist. Three masks were used to obtained different gap and electrode width patterns. The photomask designs had electrode widths of 150 μm and gaps of either 50, 80, or 100 μm. One of the mask designs is presented in Figure 5.6; the electrodes are not properly displayed due to the limited resolution of this document.

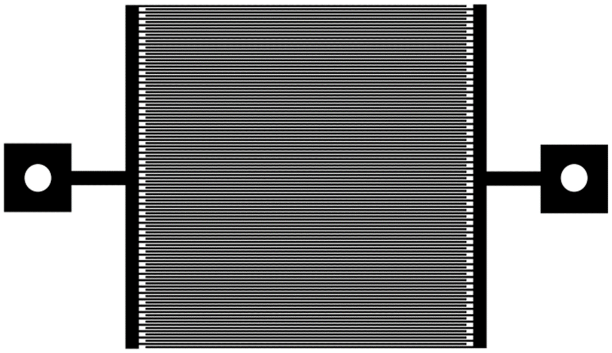

Figure 5.6. Photomask design used for the photolithography process corresponding to electrode widths of 150 µm and gaps of 80 µm.

After the sample was exposed, the board was immersed in a solution of distilled water and positive photoresist developer (MG Chemicals #418) at a 10:1 volume ratio for 4 minutes. Next, the developed sample was chemically etched using a solution of one-part hydrochloric acid (Sunnyside, 31.45% HCl, 20° Baumé) and two-parts of hydrogen peroxide for around 23 minutes. A multimeter was used to verify that the electrode terminals were electrically disconnected from each other, indicating that the copper was completely edged to the bottom of the board. The remaining photoresist layer was removed with acetone. For the passivation coating, alumina deposition was firstly tried, but better results were obtained using an epoxy layer. The epoxy was applied with a spatula so that a thin flat layer covered the sensing area. After fabrication, visual inspection indicated the IDE with electrode widths of 150 µm and gaps of 80 µm had the best fabrication quality (e.g., uniformity, resolution, etc.), so this geometry was used for the experiments discussed here.

5.4.2 Sensor Metering Circuit

To interface and monitor the response of the IDE element, a metering circuit based on an RC resonator [35] was assembled and connected to the electrodes. The resonant frequency of the entire system was then measured to detect changes in capacitance. The circuit outputs an oscillating signal with a frequency determined by Equation 5.1

$$f = \frac{1}{2\ln(3)\,RC} \tag{5.1}$$

where f represents the resonant frequency [Hz], R the resistance of the circuit [Ω], and C the total capacitance [F].

To characterize the metering circuit, the system was initially connected directly to a data acquisition (DAQ) system programmed with a LabVIEW routine. The DAQ consisted of a digital card and chassis from National Instruments (NI-9401 and NI cDAQ-9174). Instead of acquiring the direct digital signal from the sensing circuit, the DAQ system was set up to operate as a digital frequency counter. In this mode, the DAQ uses an 80 MHz internal time-base to measure the input frequency signal and achieve more accurate results.

The frequency response of the RC oscillator in Equation 5.1 dictates, in part, the temporal resolution of the sensor, since it fixes the rate at which the sensing element can be probed. Accordingly, for a given capacitance range, the resistance value in the RC resonator has to be optimal so the sensor is fast enough to capture the dynamics of the spray impingement. On the other hand, the temporal response of other circuit components has to be considered as well, especially the speed at which the telemetry system (described in the next section) can accurately transmit and receive data. The resistor was selected by connecting the IDE element and performing experiments until an appropriate frequency was obtained. A resistor with a value of 100 kΩ was selected, which enabled a sensor response in the sub-millisecond region.

The response of the resonator was characterized by monitoring the frequency as capacitors with known value were added to the circuit. The resonant frequency response to varying capacitance is displayed in Figure 5.7. The solid line represents the theoretical oscillating frequency based on Equation 5.1, while the blue symbols show the experimental calibration. The maximum error between the expected and measured data is approximately 10%; the difference is most likely an outcome of the parasitic resistance and capacitance of the circuit and its components.

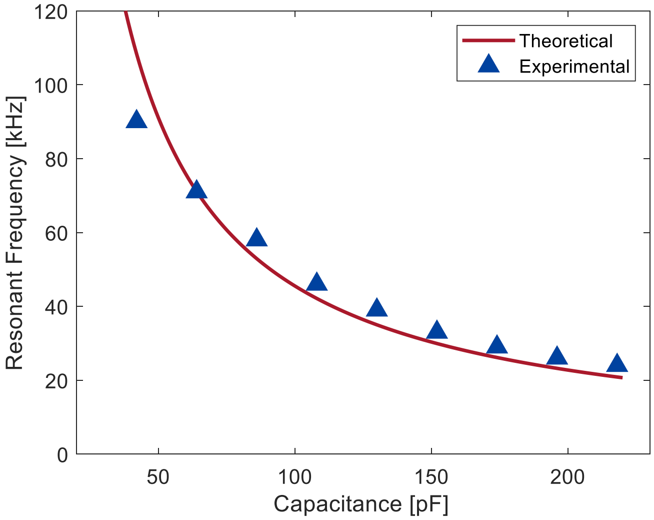

Figure 5.7. Frequency response of the sensing circuit as a function of capacitance.

A frequency of 65 kHz was detected when connecting the IDE capacitor to the circuit. Based on the results plotted in Figure 5.7, this frequency indicated that the sensor had a capacitance of approximately 70 pF when exposed to air. When the sensor is exposed to a liquid film with higher permittivity than that of air, the oscillating frequency relaxes following the curve shown in Figure 5.7 due to the increase in capacitance.

5.4.3 Instrumented Piston and Telemetry Circuitry

To achieve in-situ measurements of spray impingement in an engine, the IDE was mounted on a custom--made aluminum insert that fit inside the optical piston shell (89.0 mm in diameter) used for the imaging studies in the previous chapter. The aluminum insert consisted of two parts: the upper piece held the sensor in place, while the bottom part had a small chamber where the metering circuit, a battery pack, and a switch were located. A threaded ring held the two-piece aluminum insert in place.

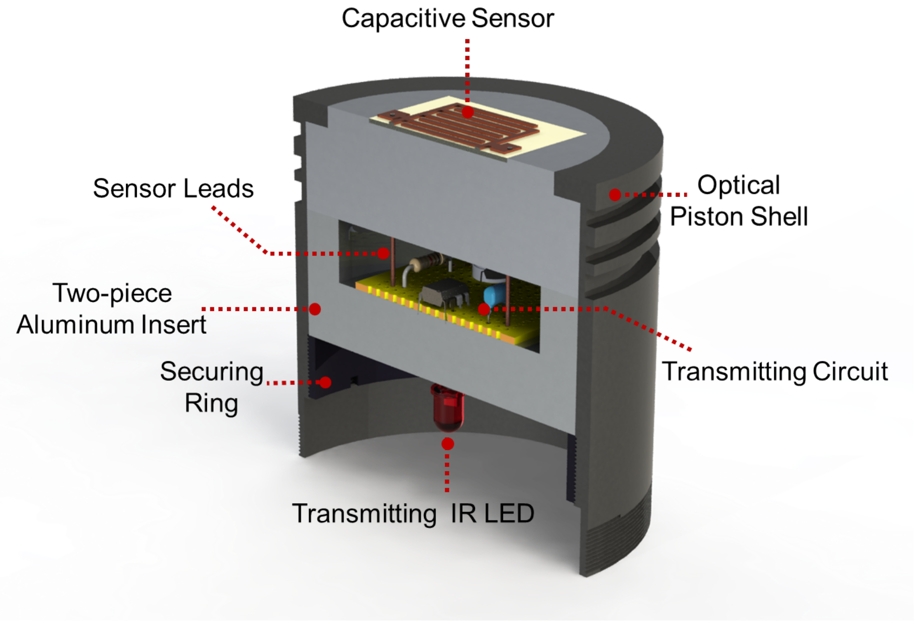

Figure 5.8. Cross-sectional view of the CAD model for the instrumented piston with the mounted capacitive sensor and non-contact data transmission circuit

Leads ran from the sensors, through the upper part of the insert, and into the chamber where it was connected to the metering circuit described in Section 5.4.2. An infrared light-emitting diode (IR LED, 940 nm, Gikfun) was connected to the metering circuit and secured to the bottom surface of the aluminum insert. The LED was connected to the circuit so that it would flash at the oscillating frequency from the RC resonator.

Figure 5.8 presents a cross-sectional view of a CAD model for the instrumented piston with the sensor mounted on the aluminum insert, the metering circuit, and the IR LED for transmitting the oscillating frequency.

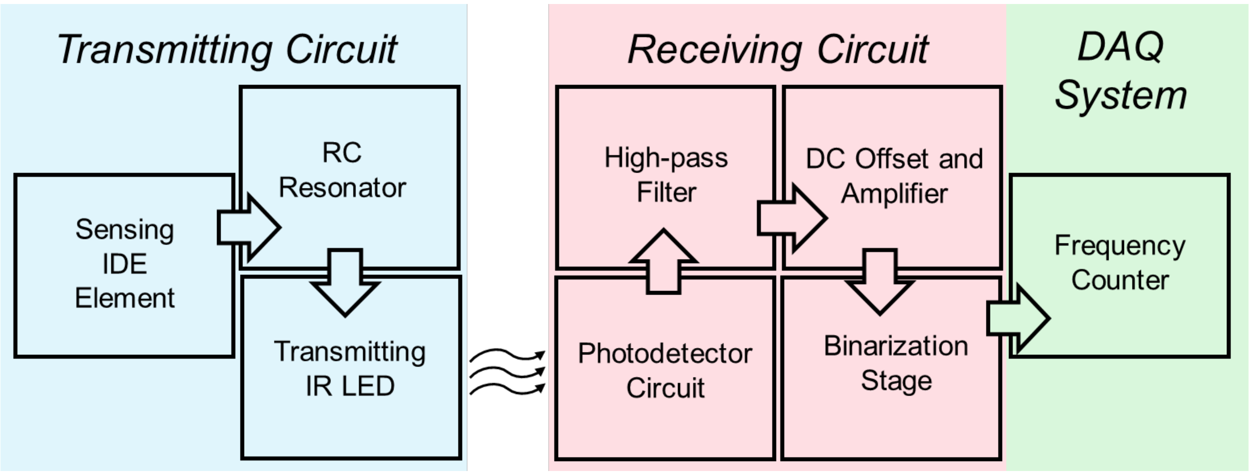

Figure 5.9. Schematic of the capacitive sensing circuit with a transmitting LED and photodetector for non-contact data transmission

A receiving circuit was built to monitor the flashing frequency of the LED. Since the input for the DAQ frequency counter described earlier requires a 5V digital signal, the receiving circuitry was designed as a multistage conditioning circuit consisting of four steps. The first stage of the receiving circuit consisted on a transimpedance photodetector made with an infrared (IR) photodiode (940 nm, Gikfun) and a JFET operational-amplifier (TL082, Texas Instruments) with a feedback gain of 1,000. The second stage was a high-pass filter [36] with a cut-off frequency of 1500 Hz. This phase eliminates the unwanted signal that the reciprocating movement of the piston would introduce –a low-frequency noise in the range of 2 to 50 Hz. The third step applies a second amplification and DC offset so the signal is within transistor-to-transistor logic (TTL) levels. The final stage translates the analog signal into a square binary signal with proper digital levels. This signal is input to a frequency counter operated using a LabVIEW routine, where the data were logged into a text file for further analysis. Figure 5.9 shows a diagram with the transmitting and receiving circuits.

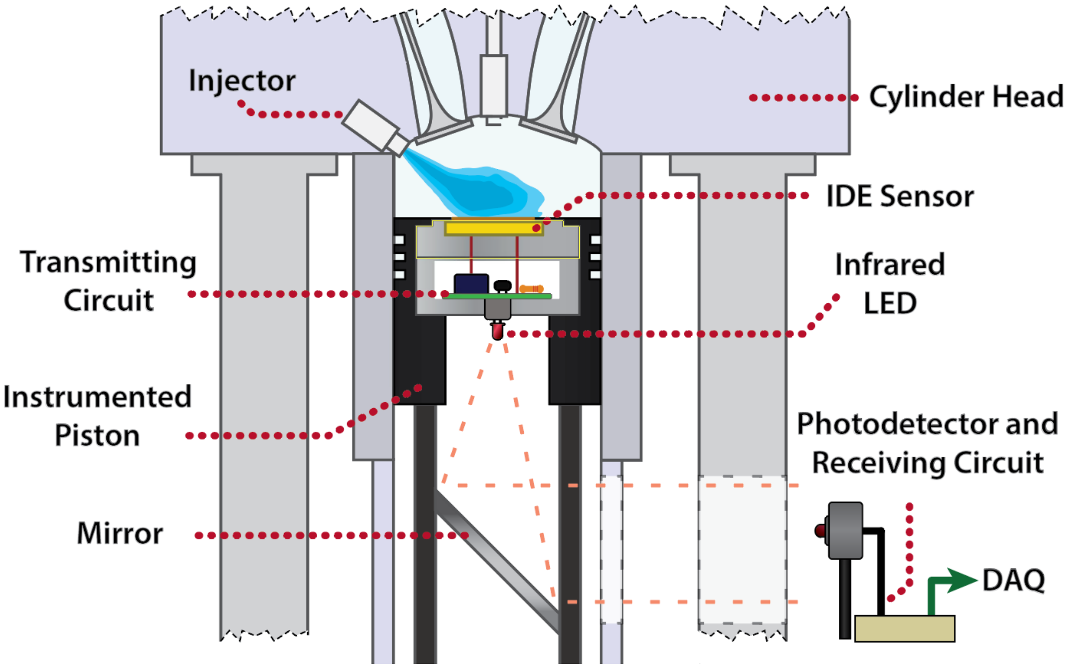

Figure 5.10. Schematic of the instrumented piston inside the single-cylinder optical engine and DAQ method.

The instrumented piston was placed inside the single-cylinder optical engine described Chapter 4. However, the engine was not motored; rather the piston was kept at a fixed location of 300° before top dead center (bTDC). A mirror with a 45° tilt angle was placed underneath the piston and was used to reflect the IR signal towards the photodetector and the receiving circuit located outside the engine. In this way, the response of the sensor was monitored without having wires connected to the engine, thus achieving a non-contact data transmission DAQ system. A microcontroller (Arduino UNO Rev3) was used to trigger the data acquisition and control the injection events. Figure 5.10 presents a schematic of the experimental setup used to test the film sensor in the single-cylinder engine. Injection pressure, injection duration, and ethanol content were varied to characterize the response of the sensor to different injection conditions and spray impingement characteristics. The surrounding air and fuel temperature were kept at ambient conditions (24°C ± 2). Table 5.1 summarizes the conditions tested.

Table 5.1. Explored experimental conditions for impingement tests

Variable	Value
Fuels	E10, E20, E50, E80
Injection Durations	0.5, 1.0, 1.5, 2.0 ms
Fuel Pressures	30, 50, 100 bar
Piston Position	300°bTDC
Fuel/Air Temperature	24°C ± 2

5.4.4 Imaging Equipment and Analysis

The injection experiments were imaged using a high-speed Mie scattering technique to capture the development of the liquid spray. A camera (Phantom V711-8G-MAG-C) captured the fuel spray at 41,000 frames per second (fps) with an exposure time of 24 μs and a resolution of 512×304 pixels, which gave a spatial resolution of 182 μm/pixel at the focus plane. A telephoto lens (Elicar V-HQ Macro MC 90mm) with an f-stop of 5.6 was used and focused at the center plane of the cylinder. The spray was illuminated using two white LED arrays (Visual Instrument #900420). An image-based trigger was used to trigger the camera and synchronize imaging with the sensor data from the DAQ system.

High-speed Mie-scattering has been previously used to study fuel impingement of direct-injection systems. Fatouraie et al. [20] imaged gasoline, ethanol, and E50 sprays in an optically-accessible engine, and used the luminosity at a pixel column close to the cylinder wall to quantify the flux of fuel that impinged on the surface. In the study [20], the authors defined the line integrated luminosity (LIL), which was the integration of the grayscale values of the pixels at a given boundary of interest as a function of time:

$$LIL = \int I_{pixel}\,(x,t)dx \tag{5.2}$$

where I_{pixel} stands for the gray scale value of the pixel at location x and time t. A similar approach was applied in this study to analyze the imaging data and compare with the sensor measurements. First, the color images were transformed into gray scale. A reference vertical line of pixels was set at 2 mm from the piston surface directly above the sensor. The reference boundary is shown as a red dashed line in Figure 5.11. It is assumed that as the spray crosses the line, the luminosity at the boundary correlates with the flux of fuel that impinges on the area where the sensing element is located. The LIL was then temporally integrated to obtain the accumulated line integrated luminosity (ALIL) to assess the total amount of fuel that reached the sensor area as a function of time:

$$ALIL = \int_{t_0}^{t_i} LIL\,(t)dt \tag{5.2}$$

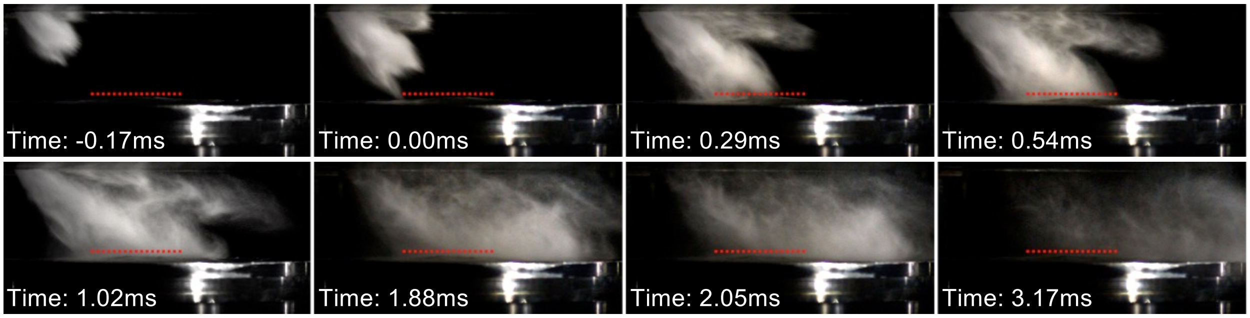

Figure 5.11. Imaging data for E50 fuel spray at an injection pressure of 100 bar and an injection duration of 2.0 ms. The dashed line indicates the boundary where the LIL and ALIL were computed. The timestamps are referenced with respect to the instant the spray crossed the line.

While this analysis can be used to understand and compare general trends, the results should be treated as semi-quantitative due to limitations of the imaging method (e.g., different extinction coefficients as a function of droplet size and fuel, variable optical thickness, etc.).

5.5 Experimental Results and Discussion

To understand and test the response of the capacitive sensor to different fuel blends, the electrodes were submerged in pools anhydrous ethanol (Decon Labs, Inc., 200 proof) and different concentrations of ethanol-gasoline blends (neat E0 gasoline from Gage Products, 40580-1BL). The liquid pool formed a layer on top of the sensor with a thickness of approximately 5 mm. As shown by the simulation results, this film thickness is beyond the saturation point of the capacitor, so the values from this test represent the maximum measurable response of the sensor.

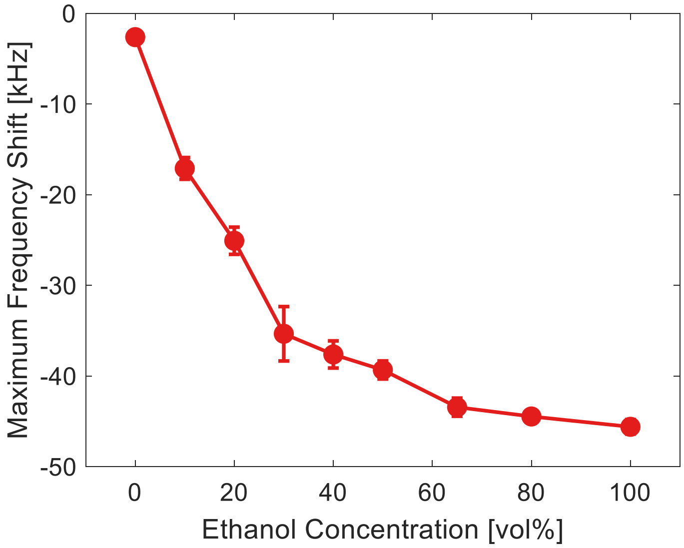

Figure 5.12. Measured maximum decrease in frequency for ethanol, gasoline, and ethanol-gasoline blends for the IDE with electrode widths of 150 µm and gaps of 80 µm

The sensor had a resonant frequency of 65 kHz when exposed to air. Figure 5.12 shows the measured shift in frequency ($\Delta f = f_{fuel} - f_{air}$) experienced by the system when the sensor was exposed to each of the ethanol/gasoline fuel blends. The symbols represent the average of five measurements, and the error bars are the standard deviations. The sensor response increases with ethanol concentration approximately linearly for E0 to E30. At higher ethanol concentrations, the sensor response is less sensitive. Higher ethanol content increases the electric permittivity of the fuel, which causes the larger frequency shift as the ethanol concentration increases. The E100 (pure ethanol) generated the maximum frequency change of 46.2 kHz. Pure gasoline (E0) generated the lowest frequency shift of only 2.6 kHz.

The results have two important implications. Firstly, the data suggest that even blends with relatively low ethanol content (e.g., E20) generate a considerable change in frequency. This indicates the sensor is sensitive to the films generated by a broad range of ethanol-gasoline blends, demonstrating the wide potential scope for the use of the proposed impingement sensor.

The second significance of the results shown in Figure 5.12 is that they indicate that the sensor is capable of measuring fuel composition; more specifically, it can detect levels of ethanol content in gasoline. As previously stated, E85 does not have a constant concentration of ethanol. Fuel composition variations introduce challenges to which the engine cannot easily react. Current flex-fuel vehicles (FFV) employ an ethanol 'virtual sensor' that retroactively calculates the alcohol content based on the exhaust gas oxygen (EGO) sensor reading and a closed feedback loop that control fueling parameters [26], [37]. Although this method is effective, its accuracy still generates concerns on component protection, fuel efficiency, and emissions for current and future engine technologies [37], [38].

Capacitive sensing for fuel composition has been explored before with some success [25], [39], [40]. Although capacitive sensing for determining alcohol concentration in fossil fuels has some remaining challenges to address [38], such a sensor could be placed in a vehicle fueling system and detect, in real-time, the ethanol percentage in the fuel tank. Having this real-time data would enable the engine operating parameters to be proactively adapted to optimize the vehicle performance for varying fuel composition "on the fly". For example, engines using E85 have problems starting [30], especially during cold conditions due to the higher enthalpy of vaporization of ethanol. Having a priori knowledge of the fuel composition would enable the use of proper fuel-composition specific ignition strategies during cold-cranking and engine start. An additional area of improvement is the fact that higher ethanol content enables a more aggressive ignition timing, which improves fuel efficiency [32]; this strategy could be applied on-demand if the appropriate ethanol concentration is detected in the tank.

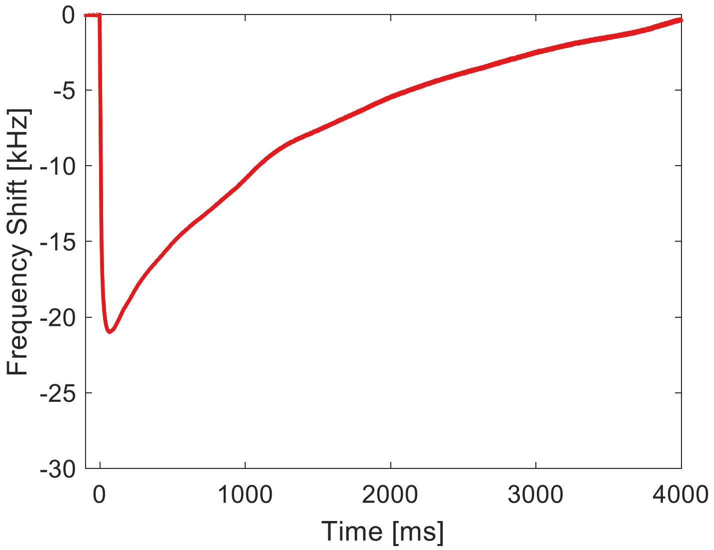

Figure 5.13. A typical result for the frequency shift of the impingement sensor. The results correspond to one of the tests of E50 at an injection pressure of 100 bar and injection duration of 0.5 ms.

After the initial results, the instrumented piston was placed inside the engine to test the fuel impingement from a realistic injection system. The resonant frequency was monitored using the telemetry system and the data were recorded for four seconds. Figure 5.13 presents typical results for the frequency shift as a function of time obtained for an injection event of E50 at 100 bar and 0.5 ms. The results show the sensor response is fast enough to capture the spray impingement as indicated by the sudden decay in frequency. The sensor also captures how the film evaporates in about four seconds, as the frequency returns to the original value. In a warm engine, the evaporation rate will be significantly higher due to the hot surfaces and the in-cylinder charge motion. As reported by Drake et al. [41], fuel films evaporate in a few dozen milliseconds.

The response of the sensor to fuel impingement from four ethanol-gasoline blends was tested by keeping the injection pressure and duration constant while varying the ethanol content.

The fuel blends tested were E80, E50, E20, and E10, each at an injection pressure of 100 bar and injection duration of 2.0 ms. While it has been reported that the amount of fuel that impinges on a surface is dependent on the ethanol concentration of a blend [6], the objective of this study was not to explore those effects, but rather to understand the sensitivity of the sensor to different fuel blends and determine the detectability limits of the sensor. The results have not been analyzed to determine intrinsic differences in the films formed. The goal of this part of the study was to demonstrate the sensor concept, and quantitative calibration remains future work as discussed in Chapter 6.

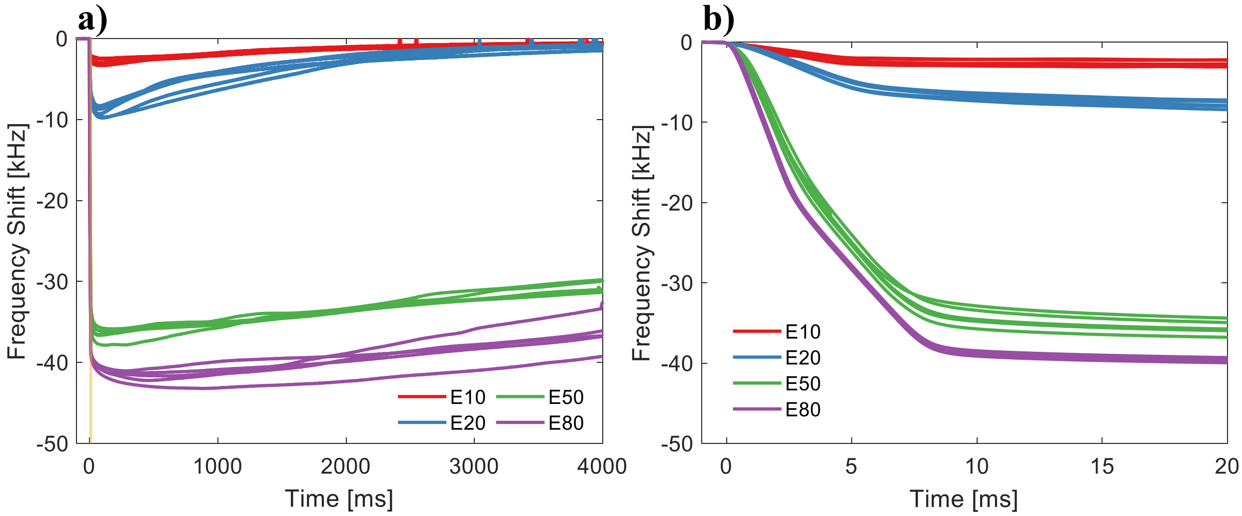

Figure 5.14. Sensor response to different ethanol-gasoline blends. Panel a) shows the 4 seconds of acquired data, while panel b) show the first 20 ms of the test. The initial 20 ms of the test are highlighted in panel a) with a thin yellow region.

The results of the instrumented piston experiments are summarized in Figure 5.14, which shows the sensor time histories of the five injection events for each fuel. Panel 5.13a presents the frequency shift for the four seconds (4000 ms) during which the data was recorded, while Panel 5.13b presents the first 20 ms after the spray impinges on the sensor. The thin yellow region in Panel 5.13a corresponds to the 20 ms shown in Panel 5.13b. As expected, the sensor exhibited higher sensitivity to increasing ethanol concentration, but overall the four fuels had similar behavior, with large frequency change within the first 10 ms, followed by a slower decay due to evaporation that lasted a few seconds. E50 and E80 experienced longer evaporation times than the four seconds shown in the figure. Additional testing indicated the evaporation times for E50 and E80 were on the order of 10 s.

In Figure 5.14b, the E50 and E80 tests displayed three regions with distinct characteristic slopes; the first one from t = 0s to 2 ms, the second from 2 ms to about 8 ms, and the last from 8 ms to the end of the test. The behavior indicates the film formed during impingement experiences three distinct phases during each fuel injection event. The first phase, which coincides well with the 2 ms injection duration, is characterized by a rapid frequency shift, indicating the rate of fuel deposition is the highest during this phase. After the end of injection, the frequency shift continues to decrease, but at a lower rate, indicating the film continued to grow even after the end of injection. Data reported by Drake et al. [41] also showed the fuel film increased in thickness after the end of injection in a DISI engine using isooctane and indolene. Two explanations are possible for film growth. First, Figure 5.11 shows that even after the injector closes, a fuel cloud lingers after the 2 ms injection duration and the images indicate the cloud deposits on top of the piston and sensor. The deposition rate of the fuel droplets is lower than the fuel deposited by the momentum of the injection event, which would explain the decrease in slope at 2 ms in Figure 5.13b. A second explanation could be that the film reconfigures due to surface tension after the momentum of the spray is no longer present. It is possible that the pull from the surface tension that may increase the thickness of the film while potentially decreasing the area. After some period of time, the film behavior is dominated by evaporation, as shown in Figure 5.13a. More in-depth analysis of the liquid film physics and experimentation are needed to more precisely understand the observed behaviors. Importantly, the results demonstrate the sensor capability to detect fuel impingement and capture the dynamics of the films formed.

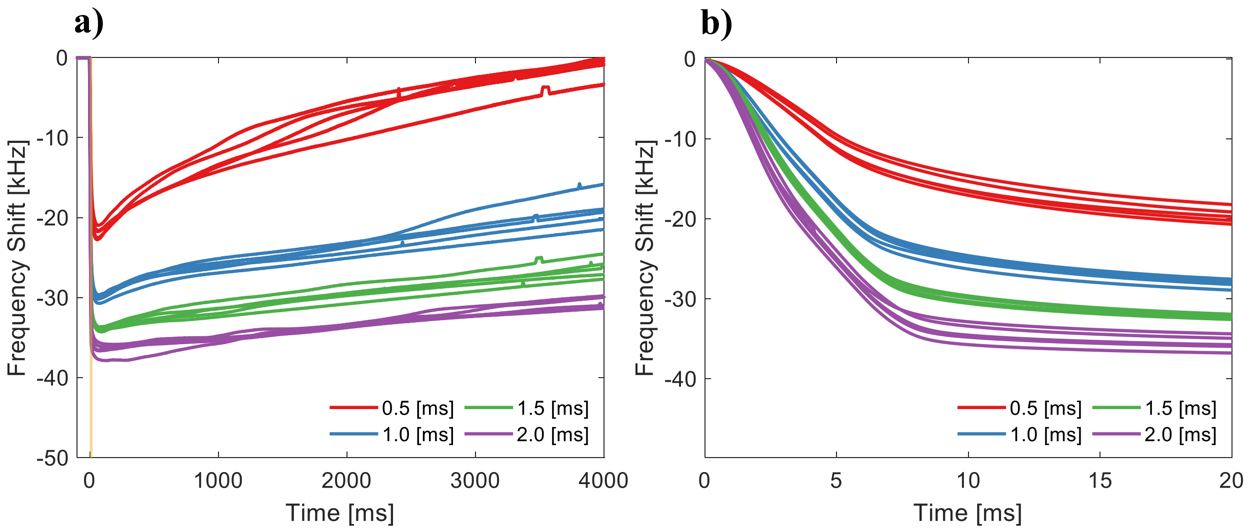

Figure 5.15. Sensor response for E50 with 100 bar injection pressure and multiple injection durations. Panel a) shows the 4000 seconds of acquired data, while Panel b) zooms in to the first 20 ms of the test. The initial 20 ms of the test are highlighted in Panel a) with a thin yellow region.

The effect of injection duration was also explored. The injection pressure was maintained at 100 bar while the injection pulse width was varied from 2.0 to 0.5 ms, effectively changing the injected fuel mass. Figure 5.15 shows the frequency shift as a function of time for the tests with E50; similar behaviors were obtained for the other fuel blends. The long-time and early-time behaviors are shown in the figure. The results show the frequency change is larger for longer injection durations. Since the injection pressure was constant for the experiments, the injected fuel mass scales with injection duration. It is expected that, to a certain degree, the film characteristics –e.g., film thickness and area– would in turn scale with injected fuel mass. Evaporation time also increased with injection duration (and injected mass). The results show the trends expected for changes in fuel mass are well-captured by the sensor.

The results in Figure 5.15b show the same three-region behavior observed in Figure 5.14b. However, the slope of the frequency change after 5 ms appears to be influenced by the injection duration. Specifically, the slope for the shortest injection (0.5 ms) has a steeper slope after 5 ms, which implies the rate of fuel deposition was larger for the shortest injection duration after injection had ended.

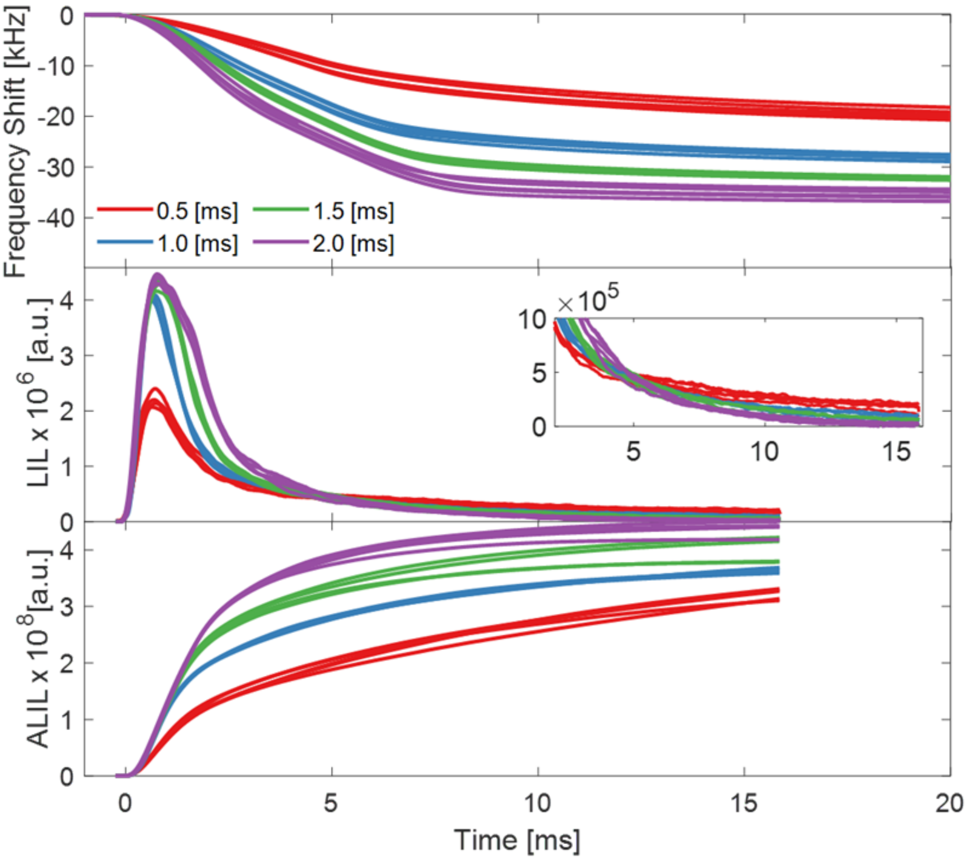

Figure 5.16. Results for frequency shift (top), LIL (middle), and ALIL (bottom) for E50 during different injection durations at 100 bar.

To better understand the observations, the LIL and ALIL of the imaging data for the tests were computed. Figure 5.16 shows the response of the sensor (top) with the LIL (middle) and ALIL (bottom) time-histories of the tests. The results show both the LIL and ALIL scaled with injection duration in the same manner as the sensor response. Secondly, the ALIL results displayed a similar change in slope as observed in the frequency shift at the end of injection for each of the injection durations. Finally, focusing on the results after the 5 ms, the LIL was higher for the shortest injection timing and the ALIL had a higher slope. The results from the imaging data indicate that fuel deposits at a higher rate for the shorter injection duration after the end of injection, confirming the trend observed in the sensor data. Visual inspection of the imaging data confirmed that fuel lingers for a longer time when the injection duration is short, probably caused by the lower momentum transfer when shortening the injection.

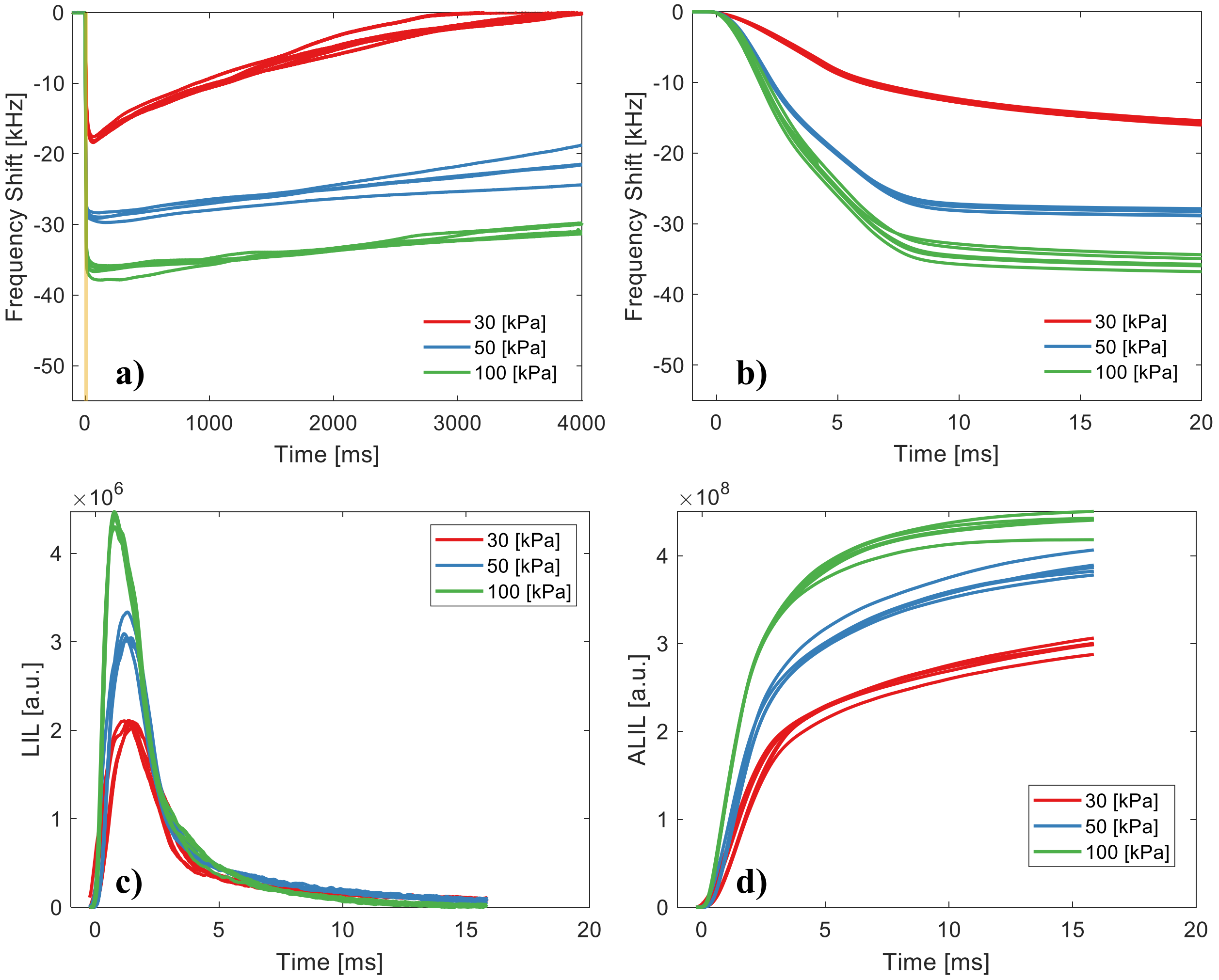

Figure 5.17. Sensor response, LIL, and ALIL results for E50 with injection duration of 2.0 ms and injection pressures. Panel a) shows the 4000 seconds of acquired data, while Panel b) zooms in to the first 20 ms of the test. The initial 20 ms of the test are highlighted in Panel a) with a thin yellow region. Panel c) shows the LIL, while Panel d) presents the ALIL as a function of time derived from the imaging data.

Figure 5.17 presents the effects of injection pressure on the response of the sensor, the LIL and the ALIL for the E50 experiments. Similar trends were observed for the other fuel blends. The three metrics show similar behaviors, indicating higher impingement with increasing pressure. Since the injection duration was constant for these experiments (2.0 ms), varying the injection pressure also changed the injected mass, which explains the observed trends. Lower pressure (and therefore lower injected mass) correlates with less impingement as indicated by the three metrics. The behavior differs from the trends observed by Schulz et al. [3] and Fatouraie et al. [20], where less impingement was associated with increasing injection pressures, due to better atomization and momentum transfer. However, unlike in the present study, Schulz et al. [3] and Fatouraie et al. [20] kept the injected mass constant, which would account for the difference in trends. Overall, the agreement between the three metrics used in the present work demonstrates the effectiveness of the sensor to detect and characterize impingement at different spray conditions.

5.6 Conclusions

Fuel impingement in direct injection engines is one of the main sources of soot emissions and unburned hydrocarbons. Although much has been learned about spray-wall interaction through single droplet experiments and other experimental and computational methods, diagnostic tools to characterize spray impingement in-situ are still lacking. This study presented the design, fabrication, and demonstration of a novel sensor based on an interdigitated electrode (IDE) capacitor for detecting and characterizing thin films generated by spray impingement from ethanol-gasoline blends. The sensor was instrumented in a piston and tests were performed using a realistic injection system in a static engine at ambient conditions, while the impingement was imaged using high-speed imaging. A few outcomes and conclusions from the study include:

- A new method for non-contact data transmission based on IR light pulses was developed and implemented which avoids physical connections to the moving parts of the engine. The telemetry circuit was effective at transmitting the measurements from the instrumented piston. The transmission approach has the potential to be used in other engine research applications where non-contact data transmission is needed.

- The sensor sensitivity to fuel films increased as the concentration of ethanol increased, and blends with all ranges of ethanol concentration, including relatively low ethanol content (e.g., E20), generated excellent sensor response (e.g., time response less than 0.5 ms).
- The sensor showed the film growth and decay follows a three-regime evolution with different deposition rates observed during and after the injection event. The first regime is characterized by fast growth rate and coincides with the injection duration. The second regime has a slower deposition rate and is driven by fuel that lingers after the end of injection and slowly deposits on the surface of the piston and sensor. During the last phase, the sensor response is dominated by slower film evaporation. The first two regimes were corroborated by the imaging data.
- The behavior of the films detected by sensor scaled with injection duration and injection pressure as expected based on the effects on injected fuel mass. The trends measured by the sensor agreed with optical metrics derived from fuel spray imaging data.
- Overall, the proposed sensor achieved the original design objectives: to enable in-situ measurements, to use non-contact data transmission, to have high-spatial sensitivity to thin films, to display fast temporal response capable of capturing the dynamics of the film formation, and to use an inexpensive fabrication.

5.7 Abbreviations

ALIL	Accumulated line integrated luminosity
bTDC	Before top death center
DAQ	Data acquisition
EGO	Exhaust gas oxygen
E*XX*	Ethanol-gasoline blend were the *XX* indicate volume concentration
FFV	Flex-fuel vehicle
fps	Frames per second
IC	Internal combustion
IR	Infrared
IDE	Interdigitated electrodes

LED	Light-emitting diode
LIL	Line integrated luminosity
TTL	Transistor-to-transistor logic
PCB	Printed circuit board
PM	Particulate matter
UHC	Unburned hydrocarbon

References

[1] T. D. Fansler and S. E. Parrish, "Spray measurement technology: a review," *Meas. Sci. Technol.*, vol. 26, no. 1, p. 012002, Jan. 2015.

[2] M.-T. Lin and V. Sick, "Is Toluene a Suitable LIF Tracer for Fuel Film Measurements?," in *SAE Technical Paper Series*, 2004, vol. 1, no. 724.

[3] F. Schulz and J. Schmidt, "Investigation of fuel wall films using laser-induced-fluorescence," in *DIPSI Workshop 2011 on Droplet Impact Phenomena & Spray Investigation*, 2012, no. 1, pp. 39–44.

[4] Y. Zhang, M. Jia, H. Liu, and M. Xie, "Development of an improved liquid film model for spray/wall interaction under engine-relevant conditions," *Int. J. Multiph. Flow*, vol. 79, pp. 74–87, Mar. 2016.

[5] X. He, M. A. Ratcliff, and B. T. Zigler, "Effects of Gasoline Direct Injection Engine Operating Parameters on Particle Number Emissions," *Energy & Fuels*, vol. 26, no. 4, pp. 2014–2027, Apr. 2012.

[6] M. Fatouraie, M. Wooldridge, and S. Wooldridge, "In-Cylinder Particulate Matter and Spray Imaging of Ethanol/Gasoline Blends in a Direct Injection Spark Ignition Engine," *SAE Int. J. Fuels Lubr.*, vol. 6, no. 1, pp. 2013-01–0259, Apr. 2013.

[7] E. Stevens and R. Steeper, "Piston Wetting in an Optical DISI Engine: Fuel Films, Pool Fires, and Soot Generation," 2001, vol. 2001, no. 724.

[8] M. C. Drake, T. D. Fansler, A. S. Solomon, and G. A. Szekely, "Piston Fuel Films as a Source of Smoke and Hydrocarbon Emissions from a Wall-Controlled Spark-Ignited Direct-Injection Engine," *SAE Tech. Pap. Ser.*, vol. 1, no. 724, 2010.

[9] M. J. M. G. Ramos and J. S. Wallace, "Sources of Particulate Matter Emissions Variability From a Gasoline Direct Injection Engine," *J. Eng. Gas Turbines Power*, vol. 140, no. 12, p. 122805, Aug. 2018.

[10] T. Badawy, M. A. Attar, P. Hutchins, H. Xu, J. Krueger Venus, and R. Cracknell, "Investigation of injector coking effects on spray characteristic and engine performance in gasoline direct injection engines," *Appl. Energy*, vol. 220, no. November 2017, pp. 375–394, 2018.

[11] R. Lindgren and I. Denbratt, "Modeling Gasoline Spray-Wall Interactions and Comparison

to Experimental Data," in *SAE Technical Paper Series*, 2004, vol. 1, no. 724.

[12] C. Bai and A. D. Gosman, "Mathematical Modelling of Wall Films Formed by Impinging Sprays," in *SAE Technical Paper Series*, 1996, vol. 1, no. 412.

[13] R. Rioboo, C. Tropea, and M. Marengo, "OUTCOMES FROM A DROP IMPACT ON SOLID SURFACES," *At. Sprays*, vol. 11, no. 2, p. 12, 2001.

[14] S. Y. Lee and S. U. Ryu, "Recent progress of spray-wall interaction research," *J. Mech. Sci. Technol.*, vol. 20, no. 8, pp. 1101–1117, Aug. 2006.

[15] F. Birkhold, U. Meingast, P. Wassermann, and O. Deutschmann, "Analysis of the Injection of Urea-Water-Solution for Automotive SCR DeNOx-Systems: Modeling of Two-Phase Flow and Spray/Wall-Interaction," in *SAE Technical Paper Series*, 2006, vol. 1, no. 724.

[16] Y. Cheng, K. Deng, and T. Li, "Measurement and simulation of wall-wetted fuel film thickness," *Int. J. Therm. Sci.*, vol. 49, no. 4, pp. 733–739, Apr. 2010.

[17] H. Cho and K. Min, "Measurement of liquid fuel film distribution on the cylinder liner of a spark ignition engine using the laser-induced fluorescence technique," *Meas. Sci. Technol.*, vol. 14, no. 7, pp. 975–982, Jul. 2003.

[18] D. Maligne and G. Bruneaux, "Time-Resolved Fuel Film Thickness Measurement for Direct Injection SI Engines Using Refractive Index Matching," in *SAE Technical Paper Series*, 2011, vol. 1.

[19] F. Schulz, J. Schmidt, A. Kufferath, and W. Samenfink, "Gasoline Wall Films and Spray/Wall Interaction Analyzed by Infrared Thermography," *SAE Int. J. Engines*, vol. 7, no. 3, pp. 2014-01–1446, 2014.

[20] M. Fatouraie, M. S. Wooldridge, B. R. Petersen, and S. T. Wooldridge, "Spray Development and Wall Impingement of Ethanol and Gasoline in an Optical Direct Injection Spark Ignition Engine," in *Volume 1: Large Bore Engines; Fuels; Advanced Combustion*, 2015, p. V001T02A004.

[21] K. Ko and M. Arai, "Diesel Spray and Adhering Fuel on an Impingement Wall," *SAE Pap. 2002-01-1628*, 2002.

[22] F. Schulz, J. Schmidt, A. Kufferath, and W. Samenfink, "Gasoline Wall Films and Spray/Wall Interaction Analyzed by Infrared Thermography," *SAE Int. J. Engines*, vol. 7, no. 3, pp. 2014-01–1446, Apr. 2014.

[23] M. C. Drake, T. D. Fansler, A. S. Solomon, and G. A. Szekely, "Piston Fuel Films as a Source of Smoke and Hydrocarbon Emissions from a Wall-Controlled Spark-Ignited Direct-Injection Engine," in *SAE Technical Paper Series*, 2003, vol. 1, no. 724.

[24] M. Mohsen-Nia, H. Amiri, and B. Jazi, "Dielectric Constants of Water, Methanol, Ethanol, Butanol and Acetone: Measurement and Computational Study," *J. Solution Chem.*, vol. 39, no. 5, pp. 701–708, May 2010.

[25] L. Bueno and T. R. L. C. Paixão, "A copper interdigitated electrode and chemometrical tools used for the discrimination of the adulteration of ethanol fuel with water," *Talanta*, vol. 87, no. 1, pp. 210–215, Dec. 2011.

[26] K. H. Ahn, A. G. Stefanopoulou, and M. Jankovic, "AFR-Based Fuel Ethanol Content Estimation in Flex-Fuel Engines Tolerant to MAF Sensor Drifts," *IEEE Trans. Control Syst. Technol.*, vol. 21, no. 3, pp. 590–603, May 2013.

[27] C. Barraza Botet, "Combustion Chemistry and Physics of Ethanol Blends to Inform Biofuel Policy," p. 147, 2018.

[28] U. S. D. of Energy, "Ethanol." [Online]. Available: https://www.fueleconomy.gov/feg/ethanol.shtml. [Accessed: 01-Jun-2019].

[29] L. Allocca, F. Catapano, A. Montanaro, P. Sementa, and B. M. Vaglieco, "Study of E10 and E85 Effect on Air Fuel Mixing and Combustion Process in Optical Multicylinder GDI Engine and in a Spray Imaging Chamber," in *SAE Technical Paper Series*, 2013, vol. 1.

[30] K. Huang, E. Du, H. Tang, and R. Tao, "Electrorheology improves E85 engine efficiency and performance," *J. Intell. Mater. Syst. Struct.*, vol. 22, no. 15, pp. 1707–1711, 2011.

[31] M. Fatouraie, "The Effects of Ethanol/Gasoline Blends on Advanced Combustion Strategies in Internal Combustion Engines," pp. 1–147, 2014.

[32] R. Singh, T. Han, M. Fatouraie, A. Mansfield, M. Wooldridge, and A. Boehman, "Influence of fuel injection strategies on efficiency and particulate emissions of gasoline and ethanol blends in a turbocharged multi-cylinder direct injection engine," *Int. J. Engine Res.*, pp. 1–13, 2019.

[33] M. Storch, F. Hinrichsen, M. Wensing, S. Will, and L. Zigan, "The effect of ethanol blending on mixture formation, combustion and soot emission studied in an optical DISI engine," *Appl. Energy*, vol. 156, pp. 783–792, 2015.

[34] D. C. Tayal, *Electricity and Magnetism*. New Delhi: Global Media, 2008.

[35] J. Z. Chen, A. A. Darhuber, S. M. Troian, and S. Wagner, "Capacitive Sensing of Droplets for Microfluidic Devices Based on Thermocapillary Actuation," *Lab Chip*, vol. 4, no. 5, p. 473, 2004.

[36] P. Horowitz and W. Hill, *The Art of Electronics*. Cambridge: Press Syndicate of the University of Cambridge, 1987.

[37] R. A. D. E. Souza, C. A. D. E. Carvalho, R. Souza, C. Carvalho, and R. Bertolucci, "SAE TECHNICAL Turbocharged flex fuel vehicles with virtual ethanol content identification Turbocharged F lex F uel V ehicles with V irtual E thanol C ontent I dentification," 2019.

[38] A. Lunati and O. Galtier, "Determination Of Mixture Of Methanol And Ethanol Blends In Gasoline Fuels Using A Miniaturized NIR Flex Fuel Sensor," in *SAE Technical Paper Series*, 2011, vol. 1.

[39] J. J. C. Kopera, M. E. McMackin, and R. K. Rader, “Methanol Concentration Smart Sensor,” in *SAE Technical Paper Series*, 1993, vol. 1, no. 412.

[40] T. Hofmann, F. Beckmann, S. Michaelis, J. Zacheja, J. Binder, and S. Tagliante, “Comparison of a conventional with an advanced micromachined flexible-fuel sensor,” *Sensors Actuators A Phys.*, vol. 61, no. 1–3, pp. 319–322, Jun. 1997.

[41] M. C. Drake, T. D. Fansler, A. S. Solomon, and G. A. Szekely, “Piston Fuel Films as a Source of Smoke and Hydrocarbon Emissions from a Wall-Controlled Spark-Ignited Direct-Injection Engine,” no. 724, 2003.

Chapter 6

Conclusions and Recommendations for Future Work

6.1 Conclusion

Direct injection spark ignition (DISI) engines offer significant thermodynamic and benefits to improve efficiency and reduce emissions of light-duty vehicles. The work presented here focused on developing and applying novel methodologies and diagnostics to elucidate multiple in-cylinder phenomena that limit the performance of DISI technology. Specifically, questions regarding spray behavior, cycle-to-cycle variability (CCV), the formation of emissions at cold-start conditions, and fuel impingement were addressed. The experimental approach was primarily based on high-speed imaging experiments in optically-accessible engines. A new diagnostic tool was also developed to probe the fuel impingement process and study spray-wall interactions in direct-injection engines. Key conclusions, outcomes, and contributions of this work include the following:

- The non-reactive spray study showed the features of fuel sprays in a quiescent condition (i.e., constant volume chamber) differed greatly compared with the behaviors observed in the high-turbulence environment of a reciprocating engine. Charge motion had a strong influence on spray structure, fuel distribution, and vaporization rate. Higher engine speeds were associated with loss of distinctive plume structure, stronger plume-to-plume interaction, and faster mixing. A strong bias on the location of the liquid fuel was introduced as the intake air disturbed the plumes closer to the intake side, with the higher engine speed having over 65% of the spray asymmetrically distributed in the combustion chamber. The results show caution should be applied when extrapolating results from constant-volume chambers (CVC) (and models derived from those data) to sprays in operational engines during the design of injection systems, and the differences in spray development become more significant at higher engine speeds.

- Fuel flash-boiling had major effects on the structure and behavior of the spray in addition to the effects of charge motion. Major plume-to-plume interaction was identified from the onset of fuel injection, and plume collapse was observed early in the development of the spray. Differences between the lower and medium speeds were dissipated by the effects of flash-boiling.
- Regarding the variability on the spatial distribution of the spray, analysis using proper orthogonal decomposition indicated that both engine speed and flash-boiling increase inter-cycle variability. Regarding the effects of speeds, intensified charge motion disturbed the orientation of the fuel plumes which translated in clear differences in the spray structure. Flash-boiling increases variability due to differences in the plume collapse time and rate.
- When using split injection at cold-start conditions, the performance of the engine was primarily controlled by the second injection, which indicates a rich fuel zone close to the spark plug is crucial for good combustion characteristics at cold-start conditions. A medium level of charge stratification (having a second injection around 45°bTDC) successfully stabilized the engine and optimized the power output of the engine. Particle size distribution of engine-out emissions also correlated with the level of stratification generated by the last injection, where the

size distribution shifted from smaller sizes (8- 20 nm) for homogeneous charge, to larger particle distributions (20 – 200 nm) for the stratified strategies.

- The sources of particulate emission from a cold DISI engine are similar to those reported for fully-warmed engines; namely, fuel films and fuel-rich pockets in the charge are the primary sources of particulates. However, a third source, fuel re-condensation was also identified in this work. Fuel recondensation increased the sooting tendency/particulate emissions of the engine at cold-start conditions.
- A new tool for characterizing the impingement of fuel sprays was developed based on capacitive sensing. A prototype sensor was designed, fabricated and tested, and the sensor was demonstrated using a production fuel injection system and optical measurements were used for validation. The sensor results demonstrated excellent sensitivity to the formation and presence of thin films, exceptional temporal response (less than 0.5 ms), and robust dynamic range in terms of response to different grades of ethanol and gasoline fuel blends from 10% ethanol/90% gasoline (by volume) to 100% ethanol.
- The films generated during fuel impingement exhibited a time-evolution marked by three clear stages, as indicated by the sensor data and confirmed by the imaging data. The first phase was characterized by a large deposition rate with a duration close to the injection pulse. The second regime was dominated by a slower growth rate driven by late droplets that linger and slowly deposited on the surface. The final stage was characterized by the end of fuel deposition and the start of film evaporation.

The work presented in this thesis offers new insights on important in-cylinder phenomena that impact in-cylinder particulate formation and other engine-out emissions. Although the tools and methods derived and applied in this work focused on gasoline, ethanol, and iso-octane in DISI engines, the analysis and techniques can be easily expanded to other fuels and compression ignition engines.

6.2 Recommendations for Future Work

The sensor developed in this thesis demonstrated great potential to detect and characterize fuel impingement in direct injection engines. Different systems have been proposed and used to assess the level of development of a specific technology with respect to full deployment or commercial use. Both the Department of Defense (DOD) and the National Aeronautics and Space Administration (NASA) developed quantitative procedures to evaluate the maturity of a system based on ascending technology readiness levels (TRL) [1], [2]. The NASA TRL consists of nine levels that span from basic fundamental research to the development and test of components for a particular application in a laboratory environment, to final the demonstration of the integrated systems in the real environment. Although the NASA ranking was conceived to assess the research and development (R&D) of technology for aerospace and space applications, the TRL can be adapted for the engine and vehicle context and presented here:

- TRL 1: Basic principles observed and reported
- TRL 2: Technology concept and/or application formulated
- TRL 3: Analytical and experimental critical function and/or characteristic proof-of-concept
- TRL 4: Component validation in a laboratory environment
- TRL 5: Component validation in a relevant environment
- TRL 6: System/subsystem model or prototype demonstration in a relevant environment

- TRL 7: System prototype demonstration in an engine or vehicle environment
- TRL 8: Actual system completed, and full implementation qualified through test and demonstration
- TRL 9: Actual system used successfully in a vehicle during a standard driving cycle (e.g., FTP-75, NEDC, WLTP, etc.).

Based on the adapted NASA TRL system, the impingement sensor is between TRL3 and TRL4. Some additional work is required to develop the prototype into a more robust tool for commercialization and application in other laboratory environments, including addressing material compatibility and calibrating the sensor for quantitative measurements of film thickness and wetted area.

For example, a limitation of the current proof-of-concept is the glass-fiber laminate used as a substrate for the sensor, which has limited resistance to the extreme thermal and stress loads that characterize engine environments. In addition, the heat-transfer properties of the laminate do not match those of the aluminum that is commonly in pistons and other engine components. The difference in heat transfer would impact the behavior of the film formation and evaporation. To match the material properties of a real engine, it is proposed to modify the sensor fabrication process and materials. The sensor could be fabricated using an aluminum wafer as a substrate, with aluminum oxide for a passivation coating, and copper for the electrodes. The fabrication process could consist of: 1) aluminum oxide chemical vapor deposition (CVD), 2) patterning of copper through photolithography lift-off, 3) passivation coating of aluminum oxide by CVD. Figure 6.1 shows a simplified side view of the proposed sensor with improved material characteristics. Using aluminum as a substrate and alumina as coating would improve the heat transfer characteristics of the device and improve the overall robustness of the tool.

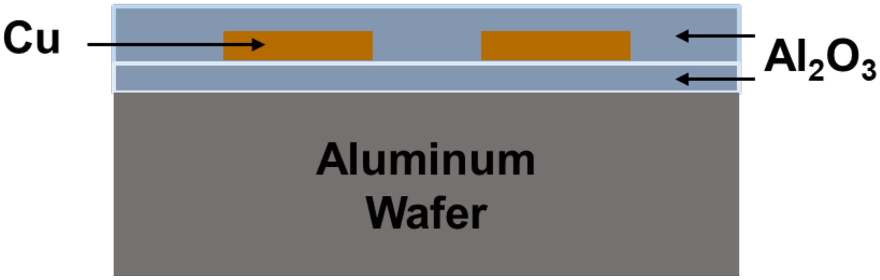

Figure 6.1. Schematic for a sensor with improved material characteristics.

Regarding the calibration for the sensor, different calibration approaches have been used for thin-film measurement techniques. Drake et al. [3] and Maligne et al. [4] used an optical technique to calibrate a refraction index matching (RIM) method for measuring thin fuel films. The methodology consisted in depositing a known volume of liquid on a surface, measuring the wetted area, and then calculating an average thickness from the ratio of the liquid volume and the area. The measurements were then correlated with the response of the RIM signal. A second method found in literature to calibrate film measurements consists of forming thin films in the gap between the sampling surface and a second surface. To calibrate a laser-induced-fluorescence technique, Schulz et al. [5] clamped two pieces of quartz with a foil of known thickness between them. The liquid was injected between the gap formed between the quartz pieces. Similarly, Chen et al. [6] calibrated a capacitive sensor using a micrometer stage to vary the film thickness formed between the sampling surface and a polycarbonate surface attached to the micrometer. A similar approach could be applied to the sensor developed in this work.

In the present work, three methodologies were used to study different characteristics of fuel sprays, fuel impingement, and the combustion process in direct injection spark ignition engines. The three studies were performed independently to isolate specific aspects of the fuel sprays and combustion processes, so direct connections between spray characteristics (including cycle-to-cycle variability), spray-wall interactions and the resulting combustion features were not directly considered. It is expected that these processes are intrinsically connected, e.g. variability in spray impingement will lead to variability in particulate emissions, etc. Future work should focus on integrating the methods developed in this thesis to provide clearer insight into how the in-cylinder phenomena interact. Future work should also strive towards more quantitative measurements of these related phenomena. Quantitative and integrated understanding of in-cylinder phenomena would represent a significant contribution to engine research and development.

6.3 Abbreviations

CCV	Cycle-to-cycle variability
CVC	Constant-volume chamber
CVD	Chemical vapor deposition
DISI	Direct injection spark ignition
DOD	Department of Defense
LIF	Laser-induced fluorescence
NASA	National Aeronautics and Space Administration
R&D	Research and development
TRL	Technology readiness level

References

[1] J. C. Mankins, "Technology readiness and risk assessments: A new approach," *Acta Astronaut.*, vol. 65, no. 9–10, pp. 1208–1215, Nov. 2009.

[2] J. Carmack, "Technology Readiness Levels For Advanced Nuclear Fuels and Materials Development Fuels and Materials Development," *U.S. Dep. Energy Natl. Lab.*, no. January, pp. 1–6, 2014.

[3] M. C. Drake, T. D. Fansler, A. S. Solomon, and G. A. Szekely, "Piston Fuel Films as a Source of Smoke and Hydrocarbon Emissions from a Wall-Controlled Spark-Ignited Direct-Injection Engine," *SAE Tech. Pap. Ser.*, vol. 1, no. 724, 2010.

[4] D. Maligne and G. Bruneaux, "Time-Resolved Fuel Film Thickness Measurement for Direct Injection SI Engines Using Refractive Index Matching," in *SAE Technical Paper Series*, 2011, vol. 1.

[5] F. Schulz and J. Schmidt, "Investigation of fuel wall films using laser-induced-fluorescence," in *DIPSI Workshop 2011 on Droplet Impact Phenomena & Spray Investigation*, 2012, no. 1, pp. 39–44.

[6] J. Z. Chen, A. A. Darhuber, S. M. Troian, and S. Wagner, "Capacitive Sensing of Droplets for Microfluidic Devices Based on Thermocapillary Actuation," *Lab Chip*, vol. 4, no. 5, p. 473, 2004.

APPENDICES

Appendix 1: Supplemental Material for the Non-reactive Study on the ECN Injector G Sprays

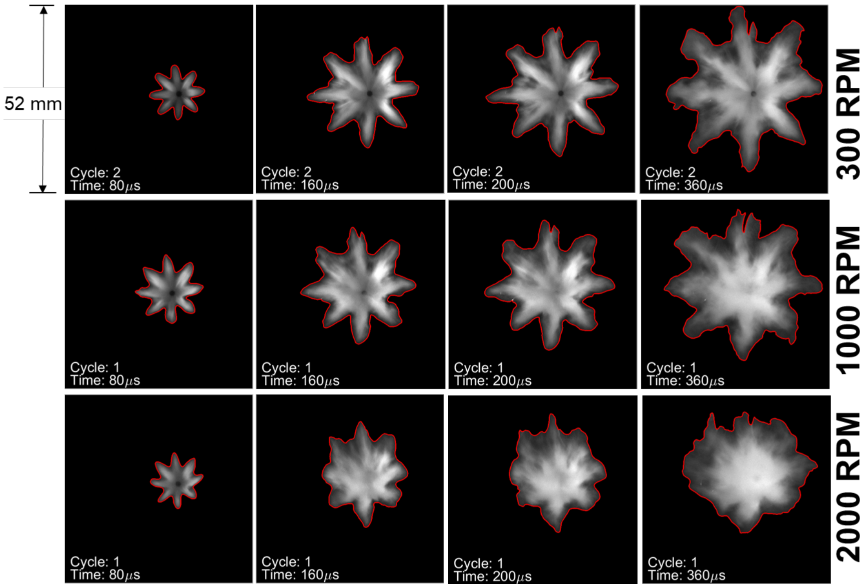

Figure A1. 1. Spray imaging for the G3-Non-flash boiling condition as a function of engine speed and time after SOI

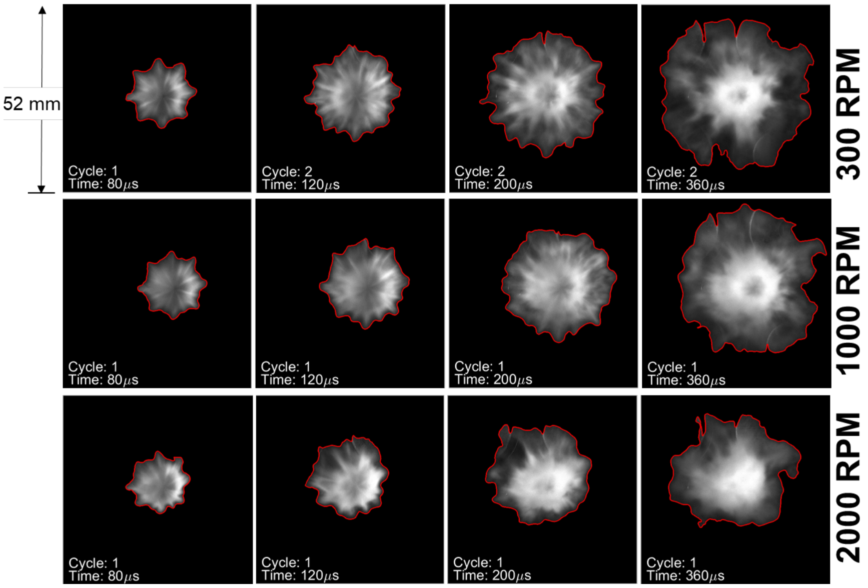

Figure A1. 2. Spray imaging for the G2-Flash boiling condition as a function of engine speed and time after SOI

Appendix 2: Supplemental Material for POD Study on the Injector G Sprays

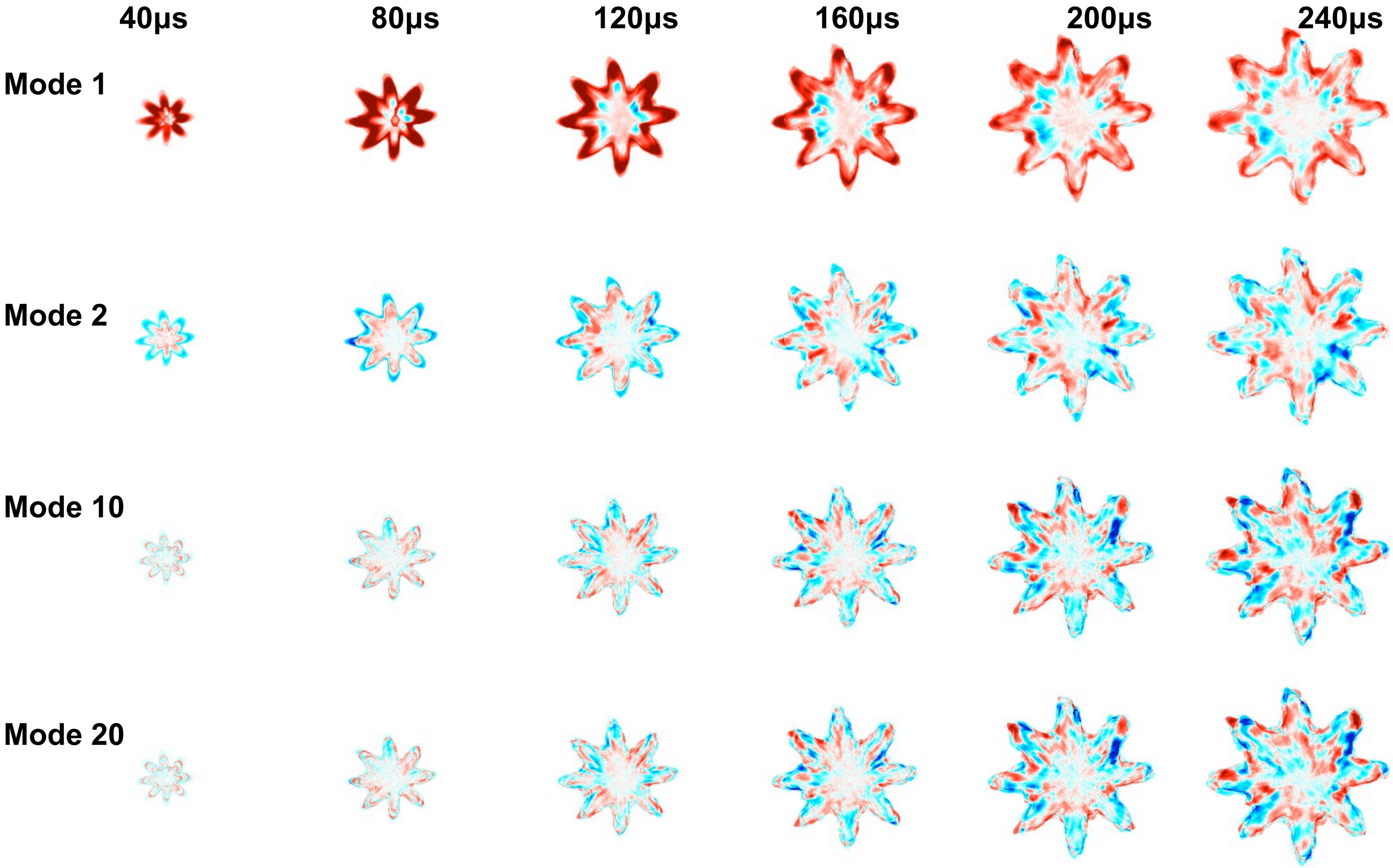

Figure A2. 2. POD modes for injection events at 300 RPM and 98 kPa

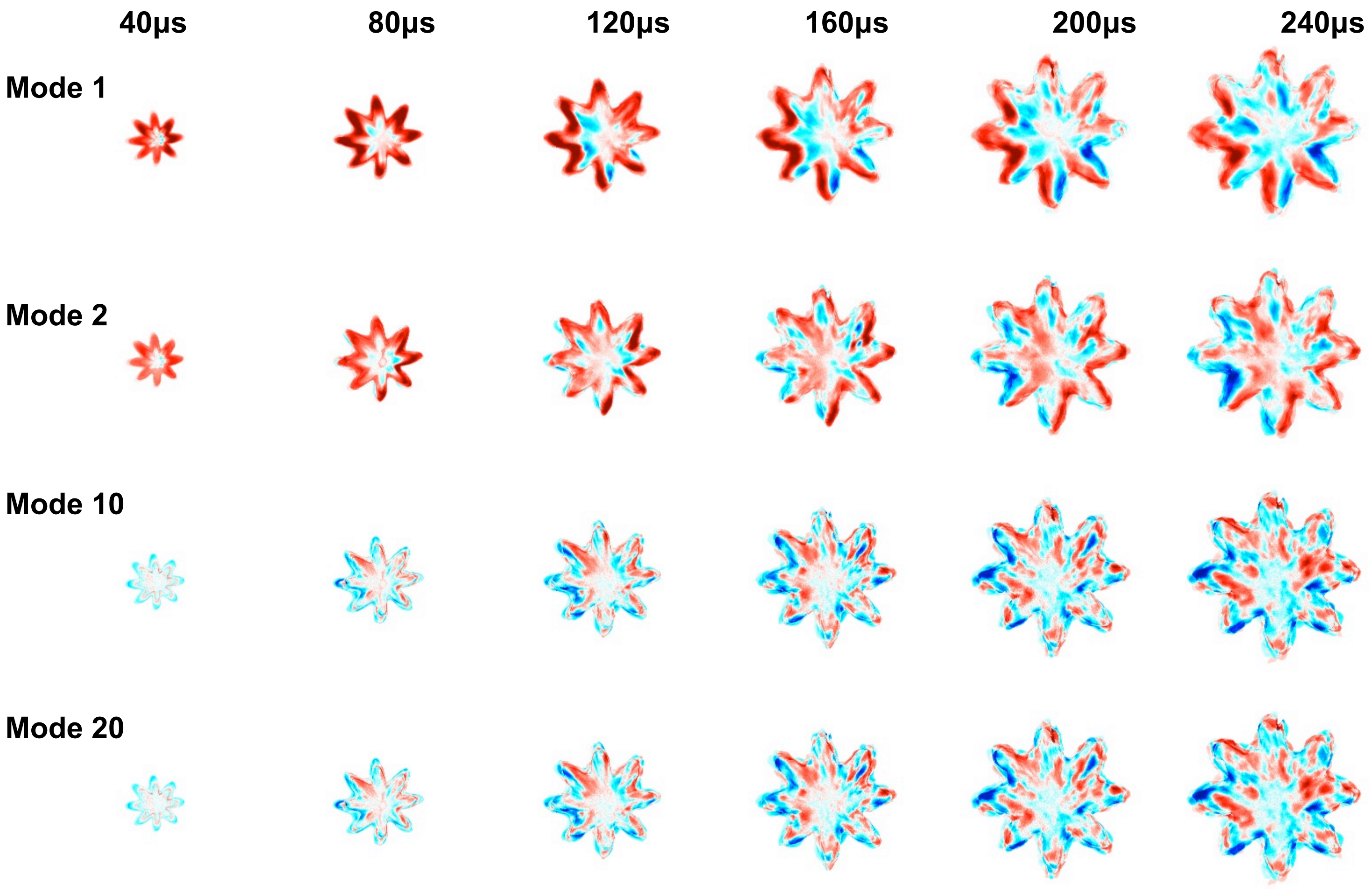

Figure A2. 3. POD modes for injection events at 1000 RPM and 98 kPa

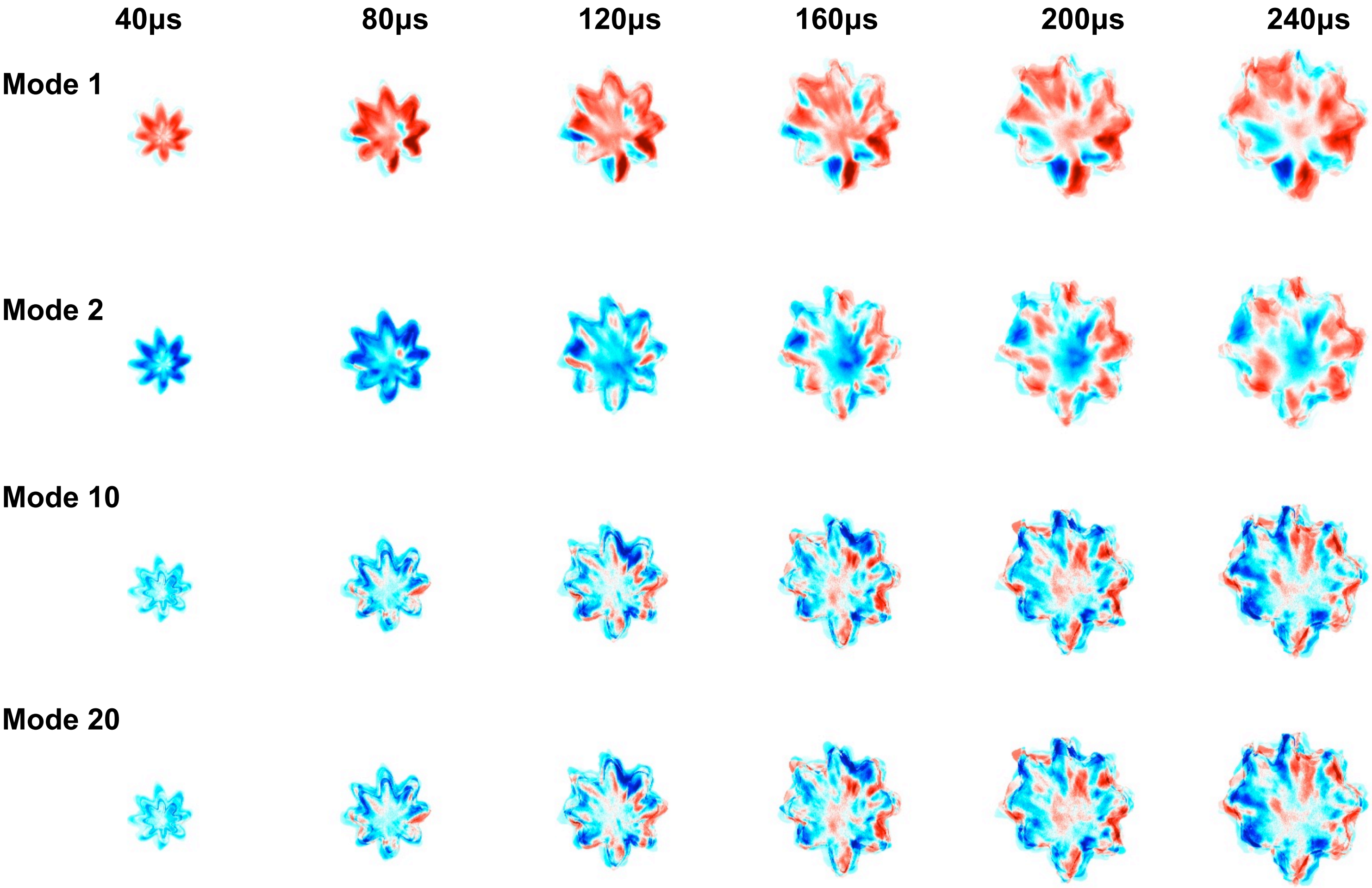

Figure A2. 4. POD modes for injection events at 2000 RPM and 98 kPa

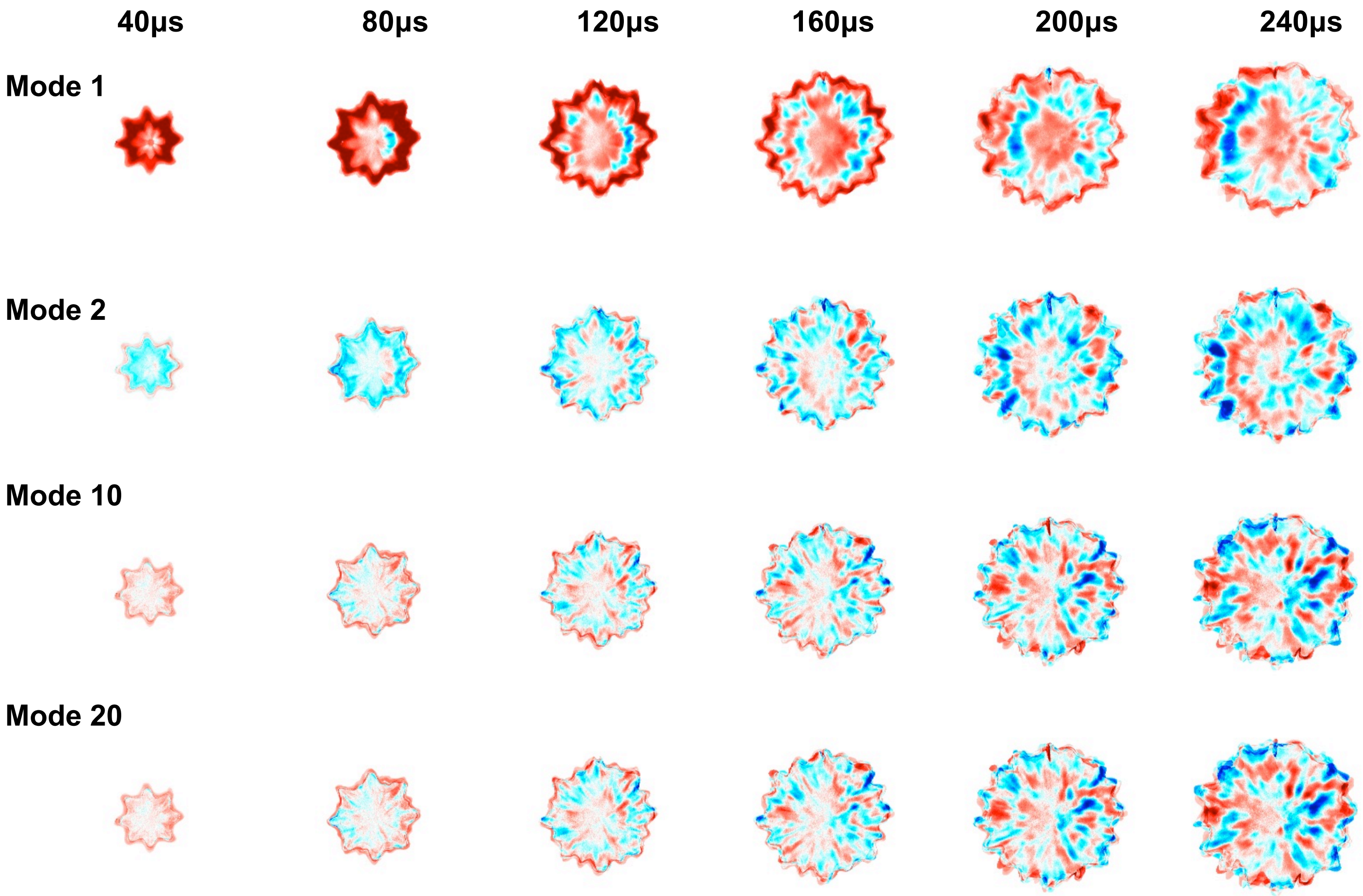

Figure A2. 5. POD modes for injection events at 300 RPM and 50 kPa

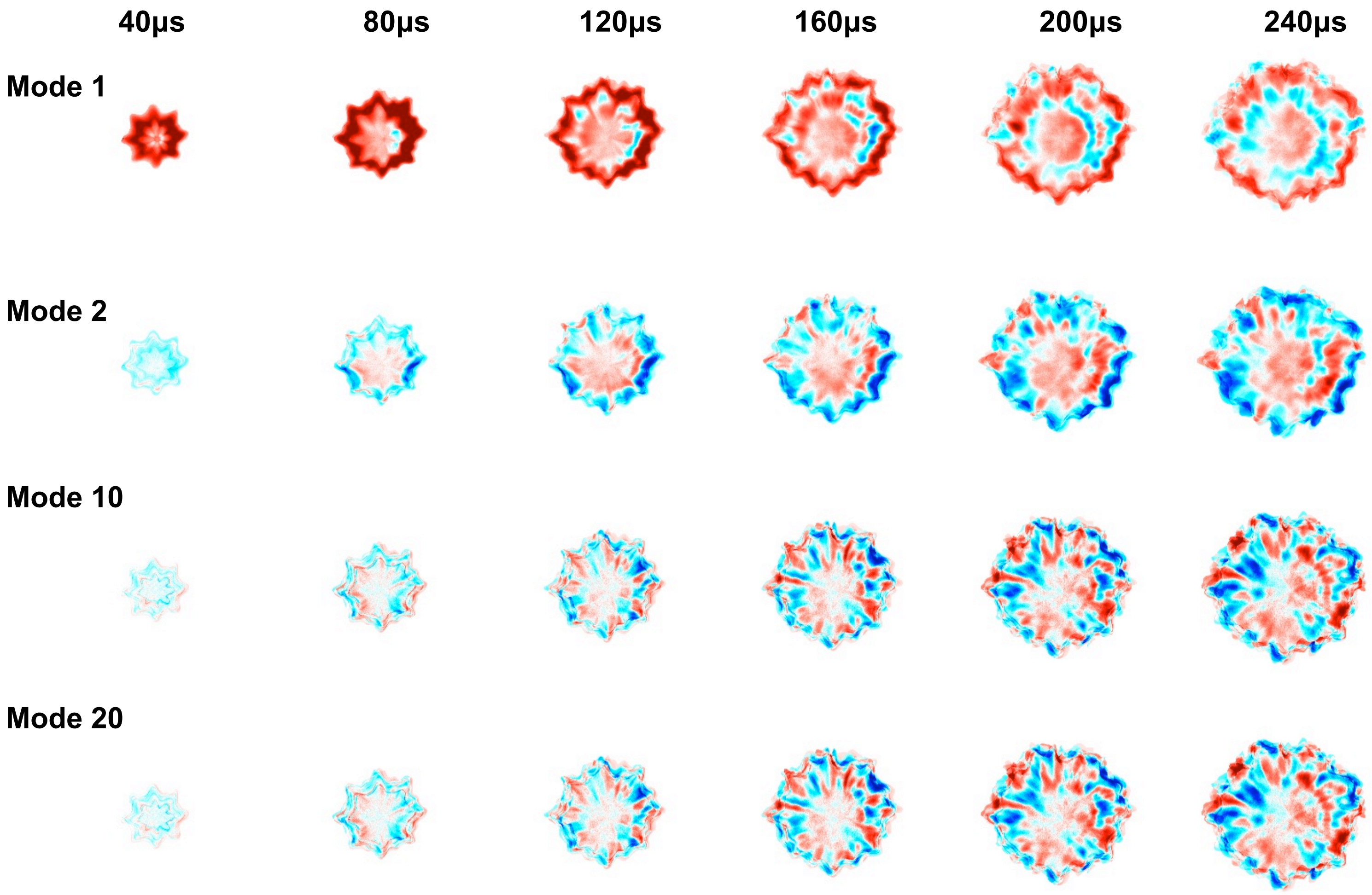

Figure A2. 6. POD modes for injection events at 1000 RPM and 50 kPa

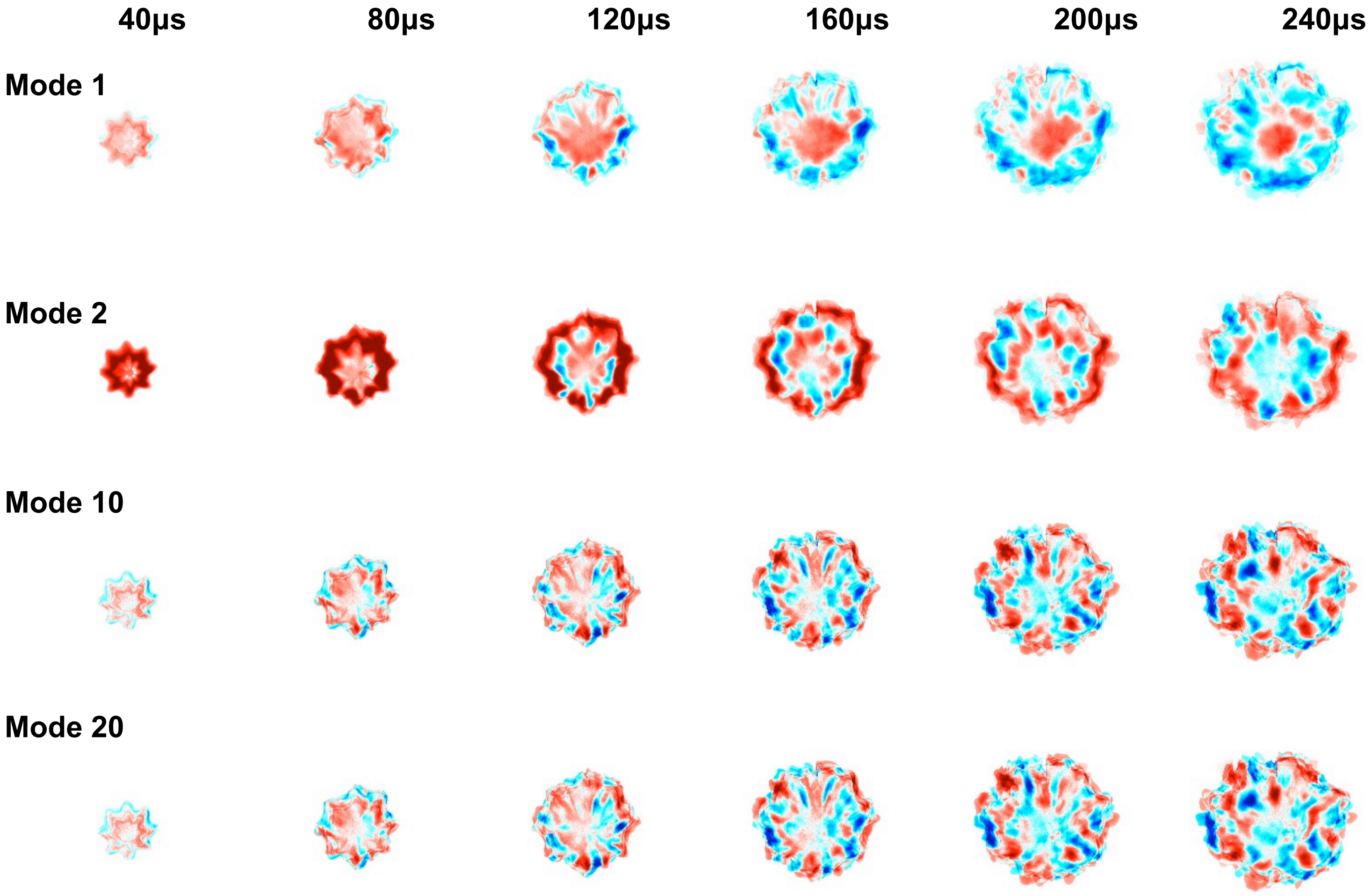

Figure A2. 7. POD modes for injection events at 2000 RPM and 50 kPa

Appendix 3: Supplemental Material for the Cold-start Emission Study

Table A3.1 Fuel properties for the fuels used in the cold-start and sensor studies.

Property	**Reference grade gasoline (E0)**	**Anhydrous ethanol (E100)**
Reid Vapor Pressure [kPa]	62.5*	15.85[a]
Lower Heating Value [MJ/kg-fuel]	43.6*	26.9[b]
Lower Heating Value [MJ/kg-mixture]	2.8	3.0
Stoichiometric Air/Fuel Ratio [Mass basis]	14.6	9.0
Hydrogen/Carbon Ratio [mole basis]	1.9*	3.0
Oxygen [mass %]	None	0.5
Research Octane Number	91.5*	~108[c]
Motoring Octane Number	83.4*	~91[c]
Octane Sensitivity (S)	8.1*	17
Heat of Vaporization [kJ/kg-fuel]	373[b]	840[b]
Heat of Vaporization [MJ/kg-mixture]	25.5	93.3
Initial Boiling Point [°C]	32.1*	78[d]

*Gage Products (http://www.gageproducts.com)

[a] http://cta.ornl.gov/cta/

[b] SAE paper 2012-01-0403

[c] SAE paper 2012-01-1274

[d] https://pubchem.ncbi.nlm.nih.gov/

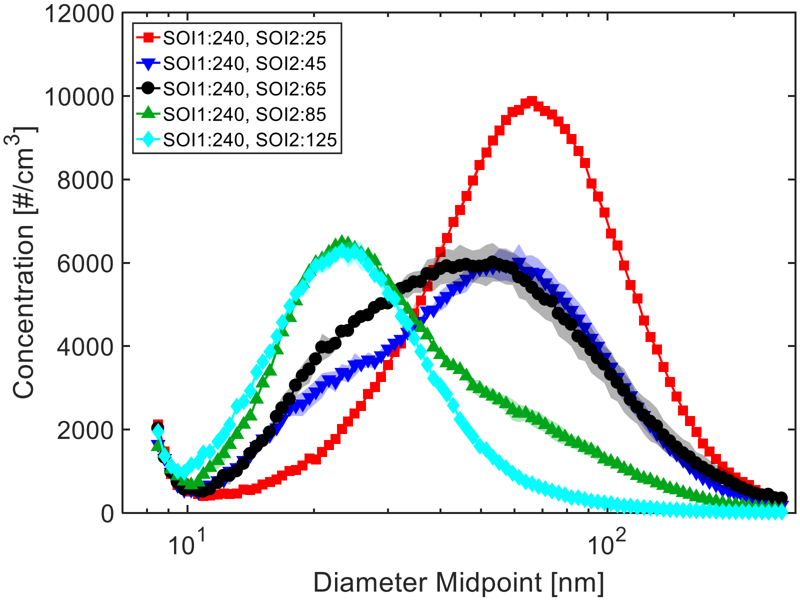

Figure A3. 1. Particle distribution for SOI1 of 240° bTDC for various SOI2. The observed trend is analogous to the one for SOI1 of 180° bTDC discussed in Chapter 4.

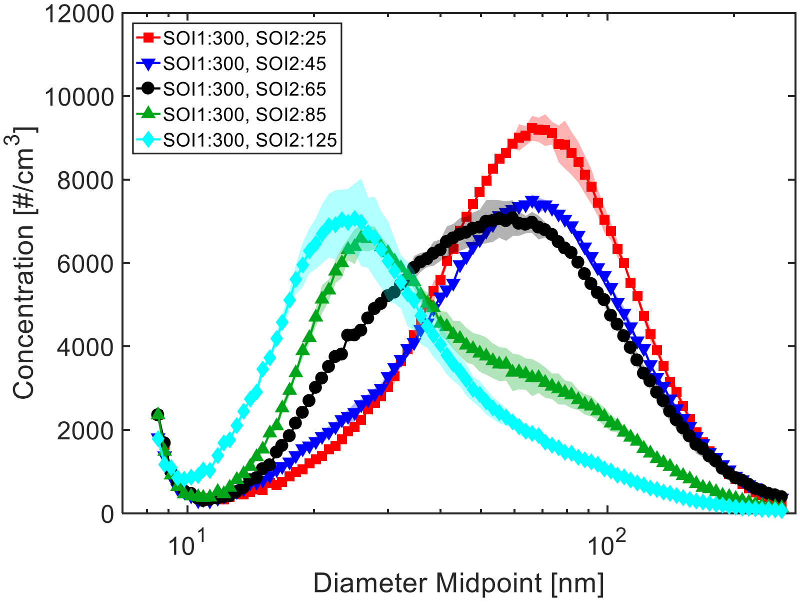

Figure A3. 2. Particle distribution for SOI1 of 300° bTDC for various SOI2. The observed trend is analogous to the one for SOI1 of 180° bTDC discussed in Chapter 4.